Electrical Characterization of Carbon Nanotubes grown by the Chemical Vapor Deposition Method

INAUGURALDISSERTATION

zur
Erlangung der Würde eines Doktors der Philosophie
vorgelegt der
Philosophisch-Naturwissenschaftlichen Fakultät
der Universität Basel
von

Bakir Babić

aus Sarajevo (BH)

Basel, 2004

Genehmigt von der Philosophisch-Naturwissenschaftlichen Fakultät auf Antrag der Herren Professoren:

Prof. Dr. C. Schönenberger (University of Basel)
Prof. Dr. L. Forró (EPF Lausanne)
Prof. Dr. M. Kappes (University of Karlsruhe)
Dr. A. Bachtold (École Normale Supérieure)

Basel, 2004

Prof. Dr. M. Tanner, Dekan

To my loving family

Contents

Chapter 1

Introduction

1.1   Molecular electronics

The possibility to use molecules as building blocks for artificial devices was first foreseen by R. Feynman in 1959 [1]. However, these suggestions have been elusive to realize experimentally for several decades. Instead, the electronic miniaturization followed a more approachable route through applications of bulk semiconductor materials. The constant scaling of the dimensions is the driving force behind the continuously improving silicon technology which will unavoidably lead to molecular or even atomic dimensions, where the processing used on micrometer range will cease to be an optimum choice. The ultimate miniaturization of logic circuits would be the use of single molecule, which would act as electronic switch and storage element [2]. In contrast to well established silicon based technology, molecular electronics aim to contact an individual molecule or small arrays of identical and perfectly ordered molecules. Due to extreme difficulties to contact and manipulate these objects, research was limited to theoretical work, initiated by Aviram *et al.* [3] in 1974. In the last decade, the invention and development of scanning probe microscopes [4] and many advances in micro and nanotechnology have allowed the observation and manipulation of a single molecule [5]. Tremendous progress in this field has been crowned by the discovery of C_{60} [6] and six years later of carbon nanotube (CNT) [7].

Exploring nanometer* size systems conceptually could be divided in two main approaches, namely top-down and bottom-up. In the top-down approach a desired system is designed from bulk material by structuring (optical lithography, electron beam lithography, evaporation techniques, etc.) the building blocks of nanosystems into a mesoscopic device (probe, interconnections, gates, etc). The main disadvantage of this approach is the

---

*nano$\equiv 10^{-9}$

limitation of the processing techniques in spatial resolution. For example, electron-beam lithography (EBL) enables structuring with a resolution of $\approx 10 - 50\,\text{nm}$, which is one order of magnitude bigger than the typical size of molecules $1 - 2\,\text{nm}$. Nevertheless, commercial availabilities, high reliability and simple integration with standard measurement set-up makes this approach widely used in the research of nanosystems. Although, the basic concept of this approach is well established, still new techniques emerge, e.g. the break junction technique [8].

The bottom-up approach is well known in chemistry. This method omniscient to nature, could be in a simple way understood as the self-organization of a desired structure given by the initial conditions. However, these objects still must be connected to the outside world by the macroscopic structures patterned with a top-down approach. The advantage of this approach is its extensive parallelism.

Although, the first steps in research of nanosystems have been done by the top-down approach, the bottom-up approach is getting more then ever involved in nanoscience. Today's research on nano-size objects compiles both approaches. This is best seen in the carbon nanotube (CNT) research, where CNTs to some extent can be grown and oriented at a specific location and then prepared for electronic transport measurements with a top-down approach. Ultimately, it is expected that the commercial implementation of molecular electronics will be done solely with the bottom-up approach.

Difficulties which we are facing during the fabrication and investigation of these systems are well compensated with interesting physics found at nanoscale dimensions and their great potential for numerous applications in many different fields. Because of their small size it is expected that these systems show pronounced quantum phenomena. Developments, primarily due to the theoretical Landauer-Büttiker [9] formalism and the observation of the Hall effect with a quantization of conductance in a two dimensional electron gas (2DEG) attracted immense interest in mesoscopic transport [9, 10]. Although, experimentally ballistic transport and quantum dot physics with Coulomb blockade and the Kondo effect have been already well established in 3- and 2D systems new exciting physical phenomena like Luttinger liquid behavior stayed modestly explored. CNTs are considered as an ideal low dimensional system where this and many other theoretically predicted phenomena can be tested. For example, the control of the spin degree of freedom in a quantum dot (CNT) [11] or the injection of entangled electrons from a superconductor to a low dimensional system (CNT) has been proposed as a building block for a quantum computer [12].

Despite of the many challenges which are in front of us, molecular electronics shows an outstanding potential for long-term future applications especially in information technology because of the ultimate density of logic

and memory functions, their low fabrication costs and power consumption. On the other hand, interesting physics found during the last decade in nanoscale systems foresee bright future to this field. In this thesis, we will give insight into this exciting field through our work undertaken on carbon nanotubes.

1.2 Carbon nanotubes

Carbon nanotubes (CNTs) have been discovered by S. Iijima in 1991 [7]. This work was motivated by a previously discovered family of macro-molecules called fullerenes. The best known member of the fullerenes family is C_{60} [6]. They are composed only of carbon atoms arranged in a three-dimensional cage structure. Carbon nanotubes are fullerenes which are extended in one dimension acquiring a cylindrical shape. Fig. 1.1a shows TEM images of multi-wall carbon nanotubes (MWNTs). In 1995, Smalley and coworkers have made an important progress by synthesizing single-wall carbon nanotubes (SWNTs) in large amounts [13]. The geometry of SWNT can be imagined as one layer of graphite (so-called graphene) rolled in a seamless cylinder with a typical diameter of $1 - 2\,\mathrm{nm}$ as illustrated in Fig. 1.1b. MWNT is a multiple, concentrically arranged set of SWNTs with an interlayer spacing of $3.4\,\text{Å}$ and a typical diameter of $10 - 20\,\mathrm{nm}$. The lengths of the two types of tubes can be up to hundreds of microns or even centimeters. Theoretical calculations and pioneering experimental investigations showed that in many respects CNTs are an exceptional material. Strong covalent bonds between carbon atoms and their high symmetry, make CNTs a very flexible and strong material. For instance, their Young's modulus is estimated to be around $1\,\mathrm{TPa}$ [14], which is the highest yet reported. Their high flexibility, together with high aspect ratio qualifies them as an ideal candidate for the tips in scanning force microscopes [15] and nanoelectromechanical resonators in the GHz regime. Some of the challenges considering this subject will be discussed in Chapter 5.

Carbon nanotubes have attracted most of the attention by the possibility to use them in nanoelectronics [16]. Band structure calculations showed (see below) that SWNTs can be either metallic or semiconducting. Unlike in other molecules, CNT's exceptional mechanical characteristics suppress Peierls instability, enabling metallic like behavior. With a diameter between $1 - 3\,\mathrm{nm}$, a SWNT is considered the smallest conducting wire to date. On the other hand, semiconducting SWNTs can act as a room temperature field effect transistor (FET) [17]. For performing electronic transport measurements, it was early anticipated that CNTs should be assembled and integrated in nanocircuitry, rather than randomly and massively produced.
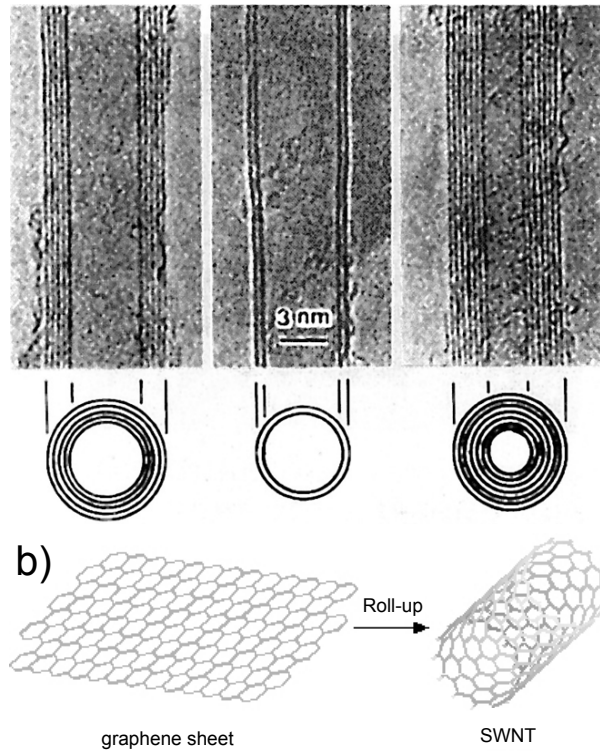
Figure 1.1: (a) A TEM image of MWNTs (adopted from Ref. [7]. (b) A hexagonal graphene sheet can be wrapped onto itself to form a nanotube.

Crucial progress in this direction has been made by Dai and coworkers [18]. They have used the chemical vapor deposition (CVD) method to grow for the first time individual SWNT *in situ* on silicon wafer from lithographically patterned catalyst islands. This method opened the possibility to grow SWNTs at specific locations and to integrate them in mesoscopic devices with well established structuring of the contacts and gate(s). Even more important, this simple and inexpensive method enabled many laboratories around the world to pursue the production and transport measurements of CNTs. Although, several different methods for the production of CNTs exists today, yet none of them fully controls their quality, diameter or chirality. Despite of the enormous work undertaken in the last decade, mass production and processing are still serious obstacles towards the realization of many proposed applications. In addition, it will not be possible to

integrate CNTs in nanocircuitry without a reliable selection between semi-conducting and metallic SWNTs. An important step in this direction has been done by Krupke *et al.* [19], where SWNTs have been separated due to their different polarization upon an applied electrical field.

Because of breathe-taking pace in this field, at this stage we will just summarize some of the main subjects of current research. From a fundamental point of view CNT has been established as a prime model nanosystem for studying low dimensional (1D,0D) solids. Theoretical and experimental work has been focused on the relationship between their atomic structure and electronic (mechanical) properties. Because of their small size, at low temperature CNT exhibit a number of interesting quantum phenomena like: single electron charging [20], quantum interference [21], Luttinger liquid behavior [22] and Kondo physics [23]. From an applied point of you, thus far individual CNTs or an assemble has been utilized to build functional device prototypes. Ensembles of CNTs have been used for field emission based flat panel displays [24]. Individual CNTs have been used as chemical and biological sensors [25, 26], nanotweezers [27] and in lithium based batteries [28]. Promising application of CNT as a FET, qualify it as a central element for the future miniaturized electronic devices. Recent investigations have shown that FETs made with semiconducting SWNTs can exceed the mobilities of the best semiconductors [29]. Also several other geometries beyond simple FET have already been explored like p-n [30], p-n-p [31] devices and nanotube/nanotube junctions [32].

Taking the above mentioned into account, it is not surprising that at this moment CNTs are of central importance for nano-science and form strong, interdisciplinary link between physics, material science and chemistry.

1.3   Carbon nanotube band structure

We will perform a calculation of the SWNT band structure starting from a simple tight-binding model for a two dimensional (2D) sheet of graphene. In Fig. 1.2a and b are illustrated a hexagonal lattice of a graphene sheet in real space and within the first Brillouin zone in reciprocal space, with corresponding lattice vectors in real $(\vec{a}_1, \vec{a}_2)$ and reciprocal space $(\vec{b}_1, \vec{b}_2)$. The unit cell of the graphene sheet contains two carbon atoms and is emphasized with grey color in Fig. 1.2a. Each of the carbon atom has four valence electrons, where three of them make sp^2 bonds forming σ orbitals. However, the transport properties are determined by the fourth electron which makes p_z bond and occupies a π orbital.

Using the tight binding approximation [33], one can obtain the dispersion
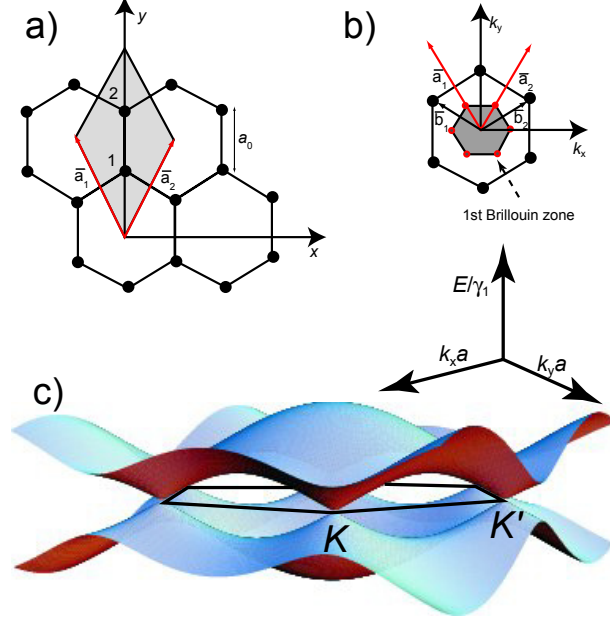
Figure 1.2: (a) Lattice of graphene. The primitive lattice vectors $\vec{a}_1$ and $\vec{a}_2$ and the unit-cell (shaded) are shown. There are two carbon atoms (black dots) per unit-cell, denoted by 1 and 2. (b) The reciprocal lattice of graphene with the 1st Brillouin zone (shaded). $\vec{b}_1$ and $\vec{b}_2$ are the primitive lattice vectors. (c) The graphene bands computed from Eq. 1.1. The Fermi level is located at the six corner points (two are marked K and K') where the valence and conduction bands touch.

relation for a 2D graphene sheet:

$$E_{graphene} = \pm\gamma_0\left\{1 + 4\cos\left(\frac{\sqrt{3}k_y a}{2}\right)\cos\left(\frac{k_x a}{2}\right) + 4\cos^2\left(\frac{k_x a}{2}\right)\right\}^{1/2},$$
(1.1)

where γ_0 is the nearest-neighbor C-C overlap integral and $a = \sqrt{3}a_0$, where a_0 denotes the nearest neighbor distance $a_0 = 1.42\text{Å}$. Fig. 1.2c depicts the dispersion relationship calculated from Eq. 1.1.

The two resulting bands, namely a bonding and an anti-bonding one, are the consequence of two carbon atoms per unit cell. There are six points where the two bands cross and they coincide with the corners of the first Brillouin zone. Because of the same number of states in the first Brioullin zone as in real space and two carbon atoms per unit cell, at $T = 0\,\text{K}$ only

the anti-bonding states are occupied, with a Fermi energy lying exactly at the position where the two bands cross. The two-dimensional graphene is therefore expected to be a semi-metal.

Single-wall carbon nanotubes can be formed if we roll-up a graphene sheet into a seamless cylinder (Fig. 1.3a). How the graphene sheet is rolled up in a SWNT, can be described with a chiral vector $\vec{C} = n\vec{a}_1 + m\vec{a}_2$, where n and m are integers. Finally, a SWNT is formed by joining the parallel lines which are defined by the starting (O) and ending (A) point of the chiral vector $\vec{C}$. Such a tube is referred as (n, m) SWNT. There are three distinct geometries of SWNTs: armchair, zig-zag and chiral (Fig. 1.3b).
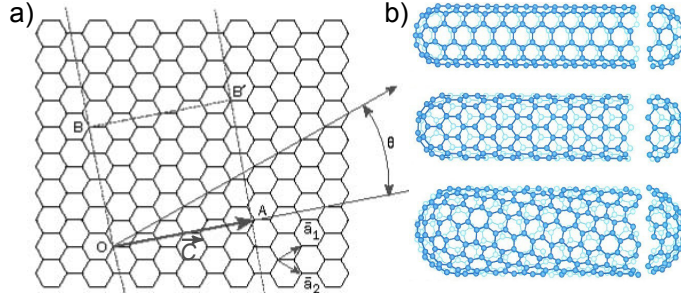
Figure 1.3: (a) The hexagonal graphene sheet can be wrapped onto itself to form a nanotube. (b) The classification of nanotubes (from top to bottom): armchair, zig-zag, chiral.

The electronic properties of a SWNT can be calculated if we impose periodic boundary conditions on the wave function along its circumference, where $\vec{k}$ becomes quantized in the following way:

$$\vec{C} \cdot \vec{k} = 2\pi q, \tag{1.2}$$

where $q \in \mathbf{Z}$ is an integer. In the case of an armchair SWNT (n, n), the periodic boundary conditions yields allowed values for the wave vector in circumferential direction according to: $nk_y a_0 \sqrt{3} = 2\pi q$. Discreteness of the k_y values, leads to a one dimensional (1D) dispersion relation in the following form:

$$E_{1D} = \pm\gamma_0 \left\{ 1 + 4\cos\left(\frac{q\pi}{n}\right)\cos\left(\frac{k_x a}{2}\right) + 4\cos^2\left(\frac{k_x a}{2}\right) \right\}^{1/2}. \tag{1.3}$$

The one dimensional dispersion relation is plotted in Fig. 1.4a and b for armchair $(10, 10)$ and zig-zag $(10, 0)$ SWNTs. Let us first discuss the case

when the k_y values are aligned with the special corner points K of the Brillouin zone. In this case the SWNT behaves as a metal. For armchair SWNT $(10, 10)$ there are in total twenty dispersion relations in the valence and twenty in the conduction band. Only, the $k_y = 0$ $(q = n)$ band and the two outermost bands are non degenerate. At low energies, we expect two modes with a linear dispersion relation to determine the electronic transport properties for a metallic SWNT. However, for different chiral vectors the boundary conditions on $\vec{k}$ around the circumference of a SWNT are not as simple as in the case of armchair or zig-zag SWNT. This situation can be visualized by the rotated orientation of quantized k_y values in reciprocal space (upper inset of Fig 1.4b). In specific cases it is possible that none of the allowed k_y values cross the K points, which results in an energy gap, i.e. semiconducting properties. Now we see that the chirality of a SWNT determines its electronic proprieties (e.g. it is metallic or semiconducting character).
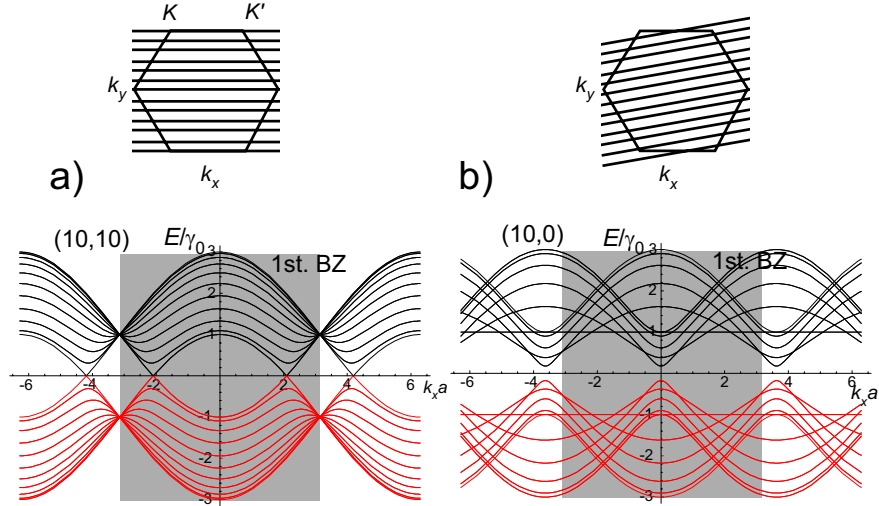
Figure 1.4: One dimensional dispersion relations for two different CNTs. Shaded region correspond to 1st. Brillouin zone. The states indicated with red color are occupied $E_F = 0$. (a) An armchair (10,10) nanotube is a metal. (b) A zig-zag (10,0) is a semiconductor. Insets: the projections of the allowed k states onto the first Brioullin zone of graphene corresponding to (a) and (b).

In the vicinity of the Fermi energy, the one-dimensional band structure

for a SWNT with arbitrary chiral vector can be approximated by:

$$E_{1D}^{lin.res.} = \pm \frac{2\hbar v_F}{d} \sqrt{\left(\frac{m-n}{3} + q\right)^2 + \left(\frac{k_\parallel d}{2}\right)^2}, \qquad (1.4)$$

where d denotes the SWNT diameter and $k_\parallel$ is the component of the k-vector along the tube axis. From this simple relation one can see that SWNTs have metallic properties when $m - n = mod(3)$ and the dispersion relation is then linear. On the other hand, when $m - n \neq mod(3)$ the SWNTs are semiconducting with an energy gap inversely proportional to their diameter. As a consequence, $1/3$ of SWNTs with all possible chiralities should be metallic and $2/3$ semiconducting. At low energies ($| E - E_F | \ll 1\,\mathrm{eV}$), the conduction bands for a metallic SWNT are linear with dispersion relation $E = \pm \hbar v_F k_\parallel$, where $v_F = 8.51 \times 10^5\,\mathrm{m/s}$ denotes the Fermi velocity and $h = 2\pi\hbar$, is the Planck's constant. The dispersion relation at low energies, for a metallic $(9,0)$ and a semiconducting $(10,0)$ SWNT are shown in Fig. 1.5a and b, respectively. Note, that for a metallic SWNT the subband spacing between the Fermi energy ($E_F = 0$) and the neighboring higher subband is inversely proportional to $d^\dagger$ and it does not contribute to transport at small energies. However, higher subbands can play an important role in large diameter CNTs, for example MWNTs.
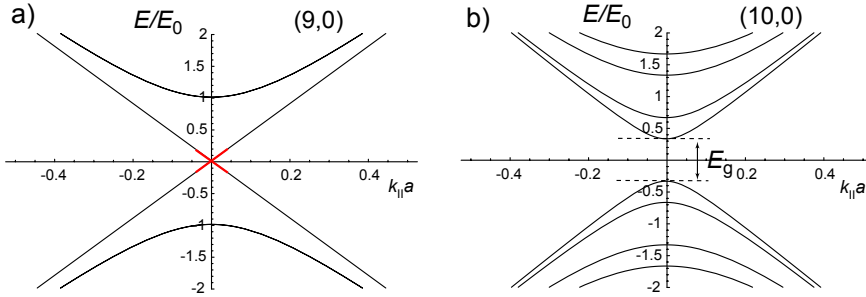
Figure 1.5: Dispersion relation for CNTs (9,0) and (10,0) at small energies, calculated from Eq. 1.4. (a) Metallic carbon nanotube. Since the subband spacing is of the order $1\,\mathrm{eV}$, only subbands with linear dispersion relation participate in transport at low energies (in red). (b) A carbon nanotube is a semiconductor, due to semiconducting gap E_g, which is inversely proportional to the diameter of CNT and equal to $E_g = 2E_0/3$, where $E_0 = 2\hbar v_F/d$.

The main theoretical predictions for the SWNT band structure derived

---

†For a SWNT (10,10) the subband gap is about $0.6\gamma_0 = 1.7\,\mathrm{eV}$.

above, have been indeed experimentally confirmed by scanning tunneling microscopy (STM) on SWNTs with various chiralities [34]. This method is especially useful for this kind of experiment because it allows the simultaneous probing and comparison between, the electronic density of states and the real-space atomic structure.

Finally, the discussion so far has been restricted to an isolated SWNT. Theoretical and experimental studies have shown that the intertube coupling in a bundle of SWNTs [35] has a relatively small effect on their band structure. However, most of the bundles of SWNTs show metallic behavior, because one single metallic nanotube is sufficient to short-cut all the semiconducting ones.

1.4 Transport properties in carbon nanotubes

Let us now discuss the peculiar transport properties of a metallic SWNT near the Fermi energy (low energy excitation). In the first approximation, the dispersion relation near the Fermi energy is linear as seen in Fig. 1.5a. Two modes are present at k_F and $-k_F$ with positive and negative slope (right and left movers). In the absence of scattering, the Landauer-Büttiker formalism predicts a conductance of

$$G = 2 \cdot 2 \cdot e^2/h, \tag{1.5}$$

for a metallic SWNT (orbital and spin degeneracies included). However, scattering in real systems is always present due to defects or phonons which reduces this ideal conductance. Let us first consider scattering by impurities.

Scattering from impurities is elastic and it can change the electron momentum. If we look again at the dispersion relation in the vicinity of $\pm k_F$, it is evident that scattering is potentially possible for example from state 1 to states 2, 3 and 4 as shown in Fig 1.6a. Since the right and left moving states are build from the orthogonal molecular orbitals in a metallic SWNT, interband scattering is suppressed e.g. between states 1 and 2. Additionally, potential scattering to the states 3 and 4 requires a large change in momentum and for long-range disorder it is suppressed. Therefore at low temperature where scattering from impurities should dominate, metallic SWNTs are expected to have long mean free paths ($l_e > 1\,\mu$m). However, for semiconducting SWNTs the interband scattering is allowed, due to the fact that the states are build from mixed orbitals (bonding and anti-bonding) [36]. In this case, it is expected that the transport through the semiconducting SWNT is more sensitive to disorder (long range) where back-scattering processes are now allowed (Chapter 3.)

For the discussion of phonon scattering we have to distinguish between scattering by acoustical and optical phonons. To scatter from an acoustical
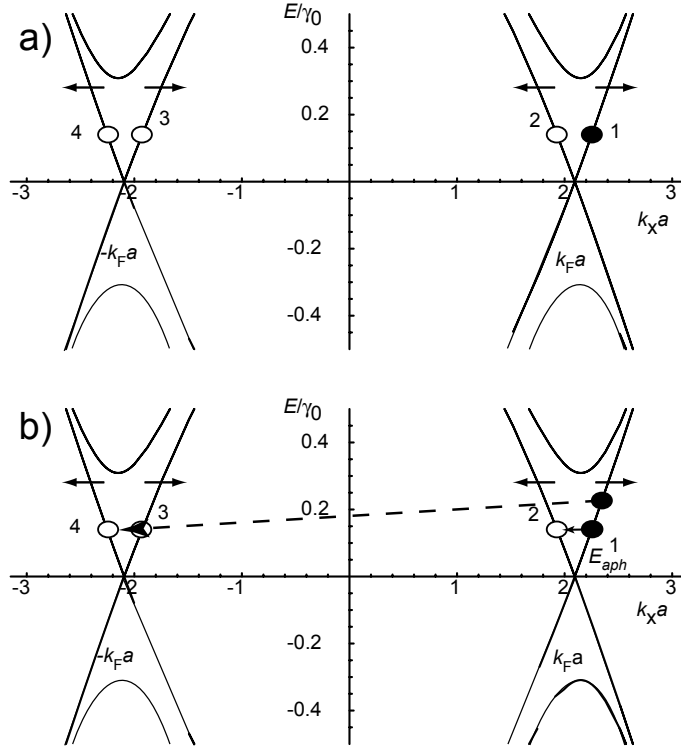
Figure 1.6: (a) Impurity scattering processes in a metallic SWNT. Position 1 (full circle) indicates an initial state of an electron. Potential final scattering to states 2,3 and 4 (open circles) is suppressed due to the unique band structure of SWNT. (b) An acoustic phonon scattering process in a metallic SWNT. This scattering at room and low temperatures can scatter electron from initial state 1 only to final state 2 (solid arrow) and it is forbidden between states 1 and 3,4 (dashed arrow).

phonon one has to provide energy $E_{aph} = \hbar v_{ph} k_{ph}$. Scattering by an acoustical phonon to state 3 and 4 is not possible, because such process requires a large change in the electron moment of $\Delta k = k_{ph} = 2k_F$ (Fig. 1.6b). This would correspond to a phonon energy of $E_{aph} \approx 100\,\text{meV}$ which is much higher than $k_B T$ even at room temperature, where k_B is the Boltzmann constant. However, scattering to state 2 is suppressed due to 1D nature of a SWNT. A quantitative analysis shows that the resistance due to scattering by acoustical phonons in 1-D systems should be proportional to tempera-

ture $R_{1D}^{ph} \sim T$ [37]. Note the striking difference compared with a 3D metal (copper) where the phonon scattering length is order of 10's of nm, with $R_{3D}^{ph} \sim T^5$.

At room temperature, for a small excess electron energy ($eV_{sd} < 100\,\text{meV}$) scattering from the optical phonons in CNT can be neglected, since there are no unoccupied states at energies

$$E_{final} = E_{initial} - E_{oph}, \tag{1.6}$$

where E_{oph} is the energy of the optical phonon. For large biases, i.e. at high electrical field electrons in a CNT can acquire sufficient energy to emit optical phonons. In that case electrons immediately backscatter as schematically illustrated in Fig. 1.7a. A steady state is approached when the electrons moving in forward direction have an energy E_{oph} higher than the backward moving ones. This leads to a saturation current of approximately $25\,\mu\text{A}$, for $E_{oph} \approx 160\,\text{meV}$ [38]. Experimental details on scattering from optical phonons in a CNT will be discussed in the following chapter.
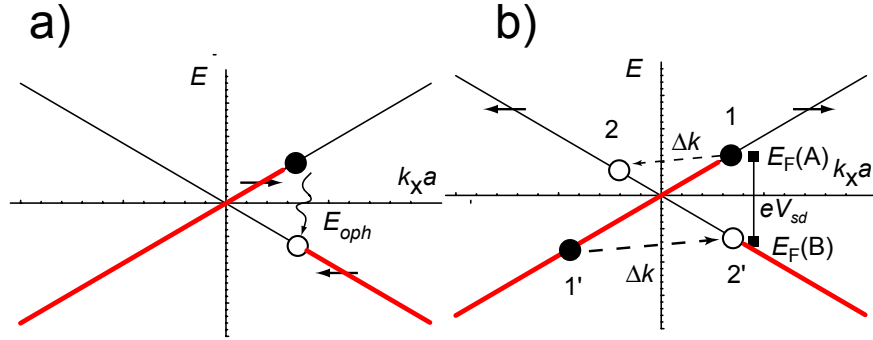
Figure 1.7: (a) Optical phonon emission occurs in non-linear regime, after which electron is backscattered. (b) An electron-electron scattering process in a metallic SWNT. In this case, electrons in the initial states labelled by 1 and 1' can be scattered to the states 2 and 2'.

Finally, we will discuss electron-electron scattering. Electron-electron scattering must fulfill energy and momentum conservation. Because of the large density of states in 3D metals the same number of electrons will be scattered in forward and backward direction. That is why this mechanism can be neglected considering the resistance in normal metals. However this situation is drastically changed in low dimensional systems as in SWNTs. It is easy to see in Fig. 1.7b that forward moving electrons in states 1 and 1' can be scattered in states 2 and 2', conserving energy and momentum.

Chapter 2

Suitability of carbon nanotubes grown by chemical vapor deposition for electrical devices

Using carbon nanotubes (CNTs) produced by chemical vapor deposition, we have explored different strategies for the preparation of carbon nanotube devices suited for electrical and mechanical measurements. Though the target device is a single small diameter CNT, there is compelling evidence for bundling, both for CNTs grown over structured slits and on rigid supports. Whereas the bundling is substantial in the former case, individual single-wall CNTs (SWNTs) can be found in the latter. Our evidence stems from mechanical and electrical measurements on contacted tubes. Furthermore, we report on the fabrication of low-ohmic contacts to SWNTs. We compare Au, Ti and Pd contacts and find that Pd yields the best results.

The present work is structured in two main sections. The first is devoted to our results on carbon nanotubes (CNTs) grown by chemical vapor deposition (CVD) emphasizing on the problem of CNT bundling, which occurs during growth. The second section discusses our results on the contacting of CVD-grown tubes using the metals Au, Ti and Pd.

2.1 Supported and suspended carbon nanotubes prepared by CVD

The full control and understanding of structural and electronic properties of carbon nanotubes remain a major challenge towards their applications in nanoelectronics. Today, there exists several different production methods of carbon nanotubes (CNTs). Among them, chemical vapor deposition (CVD) emerged [39, 40, 18] as the most prominent one for the investigation of the

electronic and electromechanical properties of CNTs. The most important advantages of the CVD method are that CNTs can be grown at specific locations on the substrate and at lower temperatures with simpler equipments as compared to the arc discharge and laser ablation methods. However, CNTs grown with this method vary in a quality and display a rather large dispersion in diameter which might be a sever problem for potential applications. Following the published recipes, we found that CVD grown CNTs differ dramatically if they are grown supported on a substrate or suspended over structured slits. This suggests that the nanotube-substrate interaction plays an important role in the final product in addition to growth parameters and catalysts.

2.1.1 Growth method

Two types of catalysts are used for the growth of CNTs. The first catalyst, which we will name catalyst 1, is similar to that described in Ref. [40]. The catalyst suspension consists of $1\,mg$ iron nitrate seeds ($Fe(NO_3)_3 \cdot 9H_2O$) dissolved in $10\,ml$ of isopropanol. The other catalyst, which we will call in the rest of the paper catalyst 2, has been prepared similar to that described in Ref. [18]. To $15\,ml$ of methanol, $15\,mg$ alumina oxide, $20\,mg$ $Fe(NO_3)_3 \cdot 9H_2O$ and $5\,mg$ $MoO_2(acac)_2$ are added. Both suspensions are sonicated for $1\,hour$, stirred overnight and sonicated every time for at least $20\,min$ before deposition on the substrate [41]. A drop of the suspension is placed on a bare substrate surface or on a substrate with predefined structured areas by electron-beam lithography (EBL) or optical lithography in the corresponding resist. After spinning at $2000\,r.p.m$ for $40\,sec$, the substrate is baked at $150\,°C$ for $5\,min$, followed by lift-off. The CVD growth of CNTs is performed in a quartz-tube furnace between $750 - 1000\,°C$ at atmospheric pressure using different gases. For catalyst 1 we used a mixture of either ethylene or methane with hydrogen and argon with respective flow rates of 2, 400, and $600\,cm^3/min$ [42]. For the catalyst 2, we have used a mixture of methane and argon with respective flow rates of 5000 and $1000\,cm^3/min$ [42]. During heating and cooling of the furnace, the quartz tube is continuously flashed with argon to reduce the contamination of the CNTs and to avoid burning them once they are produced.

2.1.2 Results and Discussion

Carbon nanotubes which are grown at the same temperature but with the two mentioned catalysts on thermally oxidized silicon substrates show similar characteristics. In both cases there is a profound temperature dependence. At relatively low temperatures (750-850 °C) predominantly individ-
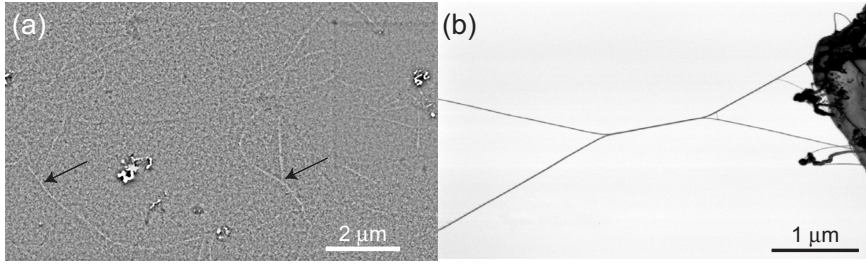
Figure 2.1: SEM images of CNTs grown from catalyst 1. In (a) the CNTs were grown on a Si/SiO$_2$ substrate at T=800 °C. The arrows point to visible branches. (b) Typical CNT network, grown over structured slits at T=750 °C. Note, that CNTs can bridge very large distances.

ual MWNTs or ropes of SWNTs are obtained with high yield. At intermediate temperatures (850-975 °C) individual SWNTs are grown with a typical diameter of 2 nm or thin bundles of SWNTs, but with less yield than at lower temperatures. At high temperatures (>1000 °C), the substrate and the CNTs are often found to be covered with an additional material, which is most likely amorphous carbon. Carbon nanotubes used in transport measurements have been solely produced at the intermediate temperature range. Fig. 2.1a shows a scanning electron microscope (SEM) image of CNTs grown from catalyst 1 on a Si/SiO$_2$ substrate.

For the purpose of mechanical and electromechanical studies, CNTs have been grown over structured slits patterned in Si$_3$N$_4$, an example of the outcome is shown in Fig. 2.1b. It is expected that for sufficiently long CNTs thermal vibrations should be readily observed with transmission and scanning-electron microscopy (TEM and SEM) [43, 44]. This holds only, however, for 'small' diameter tubes, because the vibration amplitude is strongly reduced with increasing diameter d according to ($\sim 1/d^2$). Only individual SWNTs are expected to show a substantial vibration amplitude which could be observed in SEM. We suggest this as a simple check to distinguish individual from bundled SWNTs. Fig. 2.1b shows a representing SEM image of suspended CNTs spanning over long distances (L >1 μm). None of the visible 'strings' display observable vibrations. This is not surprising considering the observed CNT branches. Clearly, in this case the CNTs must be bundled. This bundling increases the wider the slit is resulting into complex (but marvellous looking) spider webs. Further details on the search for vibrating suspended tubes can be found in chapter 5. We argue that in the absence of a support and at the relatively high temperature

CNTs may meet each other during growth. The likelihood is increased if growth proceeds in 'free' space over a large distance. Once they touch each other they stick together due to the van der Waals interaction leading to a bundle. This is also supported with TEM investigation of CNTs grown over Si_3N_4 membranes. In Fig. 2.2a and b TEM images of CNT bundles are shown.
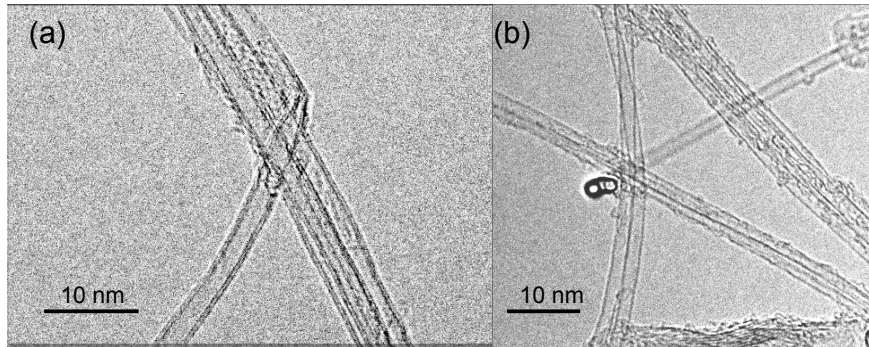
Figure 2.2: (a) and (b) TEM images of CNT bundles grown over Si_3N_4 membranes (courtesy of J. Furer).

In contrast, the growth on a substrate is different, as the tubes interact with the substrate rather than with each other. Hence, bundling is expected to be reduced. This is confirmed in SEM images, provided the catalyst density is low. However, there are bundles as well, which is evident from the observed branches visible in the SEM image of Fig. 2.1a (arrows). Even at locations where bundling is not apparent, one can still not be sure that such a nanotube section corresponds to a single-wall tube. Usually this is checked by measuring the height in AFM, but this can be misleading too, because the diameters of CVD-tubes can vary a lot, over $1 - 5\,nm$ as reported by Ref. [45]. We confirm this with our own measurements. Further insight into the question of bundling of CVD-grown CNTs can be obtained from electrical characterizations, which we report next.

2.1.3   Carbon nanotube devices

We have produced CNT devices on chip following two strategies. In the first method the substrate is covered with a layer of polymethylmethacrylate (PMMA) in which windows are patterned by electron-beam lithography (EBL). Next, the catalyst is spread from solution over these patterned structures, after which the PMMA is removed with acetone, leaving iso-
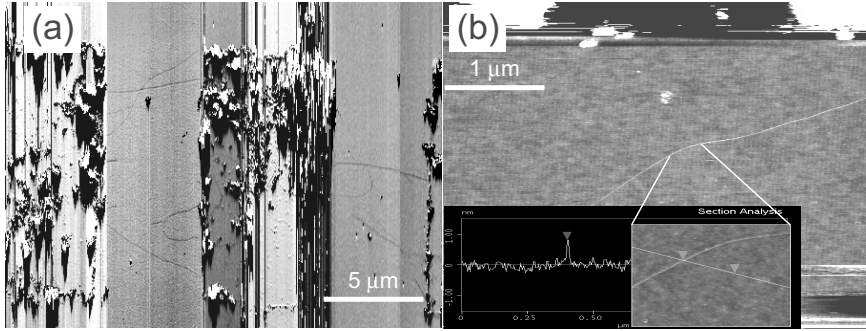
Figure 2.3: (a) Phase image recorded by tapping mode AFM, showing CNTs grown from the patterned catalyst islands and bridging between islands. (b) Topography image of an individual SWNT grown between the catalyst islands recorded by tapping mode AFM. Inset: Height measurement on the line cut (white line) for the SWNT shown in (b). The height measurements yield for the diameter $d = (1.2 \pm 0.2)$ nm for this particular tube.

lated catalyst islands ($5 \times 10\,\mu m^2$) on the surface. The substrate with the catalyst is then transferred to the oven where CVD growth of CNTs is performed. From the catalyst islands, CNTs grow randomly in all directions, but because of the relatively large distance between the islands ($5\,\mu m$) just one or a few CNTs bridge them usually. An atomic force microscope (AFM) image in phase mode with several CNTs growing from the catalyst islands is shown in Fig. 2.3a. An individual SWNT bridging the catalyst islands is shown in Fig. 2.3b. Metal electrodes (Au, Ti, Pd) are patterned over the catalyst islands with EBL, followed by evaporation and lift-off. The alignments during the EBL structuring have been done corresponding to chromium markers [46]. SEM and AFM images of contacted individual CNTs are shown in Fig. 2.4a and b.

In the second method we spread the (diluted) catalyst over the entire substrate at low concentration. The density is chosen such that at least one CNT grows inside a window of size $10 \times 10\,\mu m^2$. After the CVD process a set of recognizable metallic markers (Ti/Au bilayer) are patterned, again by EBL, see Fig. 2.4c. Using AFM in tapping mode, a suitable CNT with an apparent height of less than 3 nm is located with respect to the markers. In the final lithography step, electrodes to the selected CNT are patterned by lift-off.
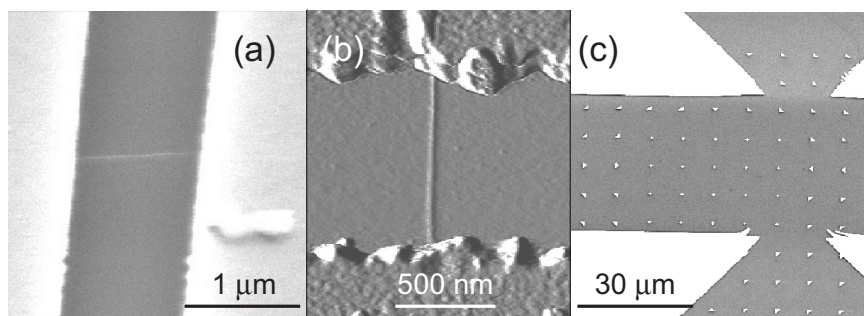
Figure 2.4: (a) SEM image of a SWNT contacted with a Ti/Au bilayer. (b) AFM image recorded in tapping mode of a contacted individual SWNT. (c) SEM image of a set of Ti/Au markers which are used to register the contact structure to the SWNTs selected before by AFM.

2.1.4   Room temperature characterization

Once the samples are made, it is common practice to distinguish semiconducting and metallic CNTs by the dependence of their electrical conductance (G) on the gate voltage (V_g), measured at room temperature $(T \approx 300\,\mathrm{K})$. This, however, cannot be considered as a proof that an individual SWNT has been contacted, because it is not well understood how the linear response conductance is altered if more than one tube is contributing to electrical transport. Even if measurements were performed on ropes of SWNTs, the measured signatures agreed quite well with the behavior expected for a SWNT [47, 48, 23]. This has been attributed to a dominant electrode-CNT coupling to one nanotube only. This scenario may be true in exceptional cases, but one would expect that the majority of measurements should display signatures that arise from the presence of more than one tube. We have recently observed Fano resonances which we attribute to the interference of a SWNT which is strongly coupled to the electrodes with other more weakly coupled ones (see chapter 4.).

Assuming that all chiralities have equal probability to be formed in growth, 2/3 of the SWNTs are expected to be semiconducting and 1/3 metallic. From the measured response of the electrical conductance to the gate voltage (back-gate), $\approx 60\,\%$ of the devices display metallic (the conductance does not depend on the gate voltage) and $\approx 40\,\%$ semiconducting behavior. Based on our assumption the larger fraction of metallic gate responses points to the presence of bundles or multishell tubes. If there are on average 2 or 3 tubes per bundle, which are coupled to the electrodes

approximately equally, the probability to observe a semiconducting charac-
teristic would amount to $(2/3)^2 = 44\%$ or $(2/3)^3 = 30\%$. Hence, we can
conclude that the bundle size is very likely small and close to 2 on average.
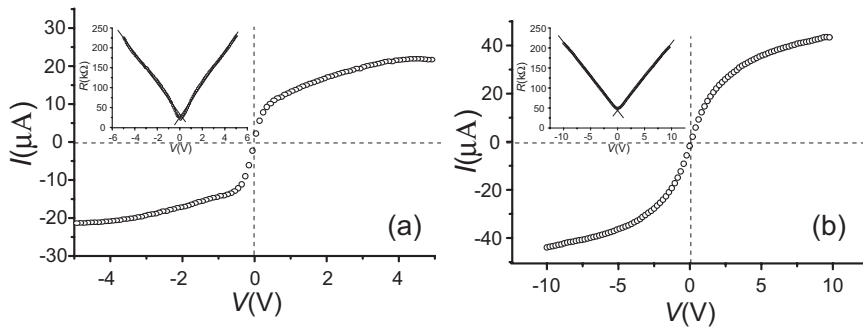
Figure 2.5: Typical $I - V$ characteristics at high bias voltage for CNT sam-
ples with a contact spacing of $1\,\mu$m. The insets show $R \equiv V/I$ versus V and
fits to Eq. 2.1 for positive and negative V (lines). (a) The extracted mean
value for the saturation current for this device is $I_0 = 24.3 \pm 1.2\,\mu$A which sug-
gests transport through an individual SWNT. (b) A higher saturation current of
$I_0 = 59.3 \pm 2.1\,\mu$A is found in this device suggesting transport through $2-3$ CNT
shells.

A powerful method to characterize contacted CNTs is to perform trans-
port measurements in the nonlinear transport regime (high bias). As pre-
viously reported by Yao *et al.* [38] the emission of zone-boundary or optical
phonons is very effective in CNTs at high fields. This effect leads to a sat-
uration of the current for an individual SWNT at $\approx 25\,\mu$A. High bias I/V
characteristics are shown in Fig. 2.5. Fig. 2.5a corresponds to an individual
SWNT. The saturation current can be extracted from the relation for the
electrical resistance $R \equiv V/I$ [38]

$$R = R_0 + V/I_0, \qquad (2.1)$$

where R_0 is a constant and I_0 is the saturation current. The dependence
of $R(V)$ versus the bias voltage V is shown in the insets of Fig. 2.5 with
corresponding fits to Eq. 2.1. Because the saturation current is relatively
well defined, its measurement allows to deduce the number of participating
CNTs. Whereas Fig. 2.5a corresponds to a single SWNT, two nanotubes
seem to participate in transport in the example shown in Fig. 2.5b. This
result is consistent with the one above and points to the presence of more
than one tube. This saturation-current method works for SWNTs but also
for multi-wall CNTs [49]. One can therefore not distinguish whether one
deals with two tubes in a rope or with one double-wall CNT.

2.2   Low-ohmic contacts

It is well known that physical phenomena explored by electrical transport measurements (especially at low temperatures) dramatically depend on the transparency between the contacts and the CNT. At low energies, the electronic transport through an ideal metallic single-wall carbon nanotube (SWNT) is governed by four modes (spin included). In the Landauer-Büttiker formalism [50] the conductance can be written as

$$G = \boldsymbol{T} \cdot 4e^2/h, \tag{2.2}$$

where $\boldsymbol{T}$ is the total transmission probability between source and drain contacts. For low transparent contacts ($\boldsymbol{T} << 1$) the CNT forms a quantum dot (QD) which is weakly coupled to the leads. Charge transport is then determined by the sequential tunnelling of single electrons (Coulomb blockade regime). If the transmission probability is increased (for which better contacts are required), higher-order tunnelling processes (so called co-tunnelling) become important which can lead to the appearance of the Kondo effect. This phenomenon was first reported by Nygård *et al.* [23]. At transparencies approaching $\boldsymbol{T} \approx 1$ we enter the regime of ballistic transport where residual backscattering at the contacts leads to Fabry-Perot like resonances [21]. Good contacts with transparencies close to one are indispensable for the exploration of superconductivity [51], multiple Andreev reflection [52] or spin injection [53] in CNTs. Nevertheless, modest progress has been made so far on the control of the contact resistances between CNTs and metal leads. Annealing is one possible route, as proposed by the IBM group [54] and we confirm their results here. We compare in the following Ti, Au and Pd contacts.

2.2.1   Comparison between Ti, Au and Pd contacts

In the ideal case of fully transmissive contacts, a metallic SWNT is expected to have a conductance of $G = 4e^2/h$ (two modes), which corresponds to a two-terminal resistance of $6.5\,\mathrm{k\Omega}$. In case of contacts made by Ti, Ti/Au or Cr on as grown SWNTs, most of the devices show resistances in the range between $100\,\mathrm{k\Omega}$ to $1\,\mathrm{M\Omega}$. In contrast, Au contacts are better, because the measured resistances range typically between $40\,\mathrm{k\Omega}$ and $100\,\mathrm{k\Omega}$. Even for the highest conductive sample the transmission probability is rather small and amounts to only $\mathbf{T} \approx 0.16$ (per channel).

To lower the contact resistances we added an annealing step to the process, which was motivated by the work of R. Martel *et al.* [54]. We have performed annealing on more than 50 samples in a vacuum chamber fitted
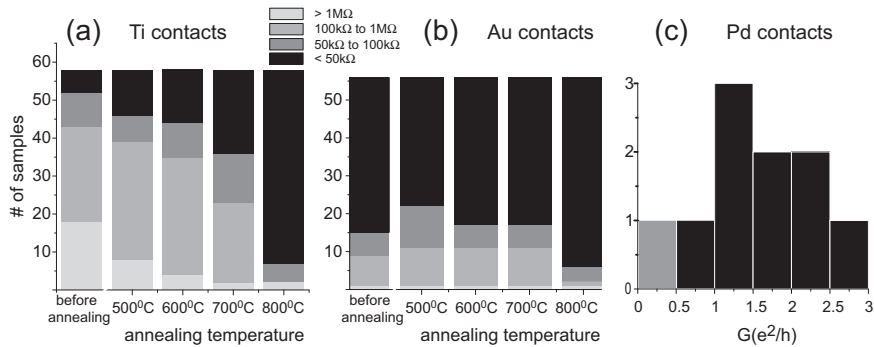
Figure 2.6: Comparison of the two-terminal resistance R at room temperature of CNT devices which were contacted with different metals: (a) Ti, (b) Au and (c) Pd. Post-annealing has been done in vacuum ($< 10^{-5}mbar$) in case of Ti and Au. In (a) and (b) the evolution of R for a large number (≈ 55) of samples as a function of annealing temperature is displayed in the form of a histogram. The representation for Pd (c) is different: the conductance $G = 1/R$ of 10 samples are compared, out of which only one has a resistance $R > 50\,\mathrm{k}\Omega$, corresponding to $G < 0.5\,e^2/h$.

with a heating stage at a back-ground pressure of $< 10^{-5}mbar$. The resistance is first recorded on as prepared devices. Then, they are annealed with temperature steps of $100\,^\circ$C for 5 min starting at $500\,^\circ$C. The results for titanium and gold contacts are shown in Fig. 2.6a and b, respectively.

In agreement with previous work [54] we find a pronounced resistance decrease for Ti contacts, if annealed at $800\,^\circ$C. It was suggested by R. Martel *et al.* [54] that the origin of the resistance decrease is the formation of titanium carbide ($\mathrm{Ti}_x\mathrm{C}$) at temperatures over $700\,^\circ$C. In contrast to Ti contacts, we do not observe a dramatic change in the sample resistance versus annealing temperature in case of Au contacts. This suggests that unlike Ti on carbon no chemical reactions take place between Au and carbon even at temperatures as large as $800\,^\circ$C. We have also compared annealing in vacuum with annealing in hydrogen within the same temperature window (not shown). The outcome in terms of resistance change is comparable to the vacuum results provided that $T < 700\,^\circ$C. At temperatures above $\approx 700\,^\circ$C the majority of the devices display a short to the back-gate. We think that the reducing atmosphere is very effective in partially etching the SiO_2 at these high temperatures.

Finally, we have also studied as-grown Pd contacts, which were recently reported to lead to contacts that are lower ohmic than Au [45]. In our own work (Fig. 2.6c) we have indeed found independently of Javey *et al.* [45] that palladium makes excellent contacts to CNTs. There is no need for an additional post-growth treatment. Metallization of CNT devices with Pd is the preferred method, because it yields low-ohmic contacts without an additional annealing step. Careful transport studies of Pd contacted SWNTs show Coulomb blockade, Kondo physics and Fano resonances (chapter 4.).

The observed resonances suggest that even in nanotubes, which look at first sight ideal, interference with additional transport channels may appear. The only plausible explanation for this observation is the existence of other tubes, hence a bundle or multishell nanotube.

2.3 Conclusion

Many applications of carbon nanotubes (CNTs) require to reproducibly place and contact single *small* diameter tubes. This is important, for example, for the realization of mechanical resonators, for field-effect transistors with reproducible characteristics and for fundamental studies of electron transport. One approach is to start from a powder of CNTs which is obtained, for example, in arc-discharge or laser-evaporation. Because these methods yield bundles of dozens of tubes, individual CNTs can only be obtained by rigorous ultrasonics and separation in an ultracentrifuge in the presence of a surfactant. If the ultrasonic step is too rigorous, the CNTs are cut into short pieces. Spreading and contacting of single tubes is possible. However, one has to bear in mind that these CNTs are covered by a surfactant which is likely to affect the fabrication of low-ohmic contacts. Moreover, the surfactant may carry charge which dopes the CNTs. In contrast to this approach, chemical vapor deposition (CVD) yields tubes in a very direct way immediately on the chip and without a surfactant, which makes this approach very attractive. Whereas a profound comparison of the quality in terms of the number of defects between these two major classes of CNTs is not yet established, the degree of bundling can be compared today. If grown by CVD on a surface at relatively high temperature and with a low catalyst density, apparently single-wall CNTs can be grown, though with a much larger spread in diameter as compared to e.g. the laser method. Although, the tubes appear to be single, as judged from SEM and simple tapping-mode AFM in air, we find in a number of different experiments clear signs for the presence of more than one tube. Measured saturation currents are often larger than the value expected for a single tube. Suspended tubes, even if no bundling is apparent in SEM in the form of branches, do not thermally vibrate as expected for a typical SWNT (chapter 5). And finally, the presence of interference effects in transport (Fano resonances) point to additional transport channels that are likely due to additional shells or tube (chapter 4). The results presented in this work show however, that the number of tubes can be small, e.g. 2-3. This gives hope that with refined catalysts, the controlled production of single tubes should be possible. In addition, we have demonstrated that relatively low-ohmic contacts can be achieved either with Ti, if an additional annealing step is used, or by Au and Pd without any additional treatment. Out of these three materials, Pd yields the best contacts (lowest contact resistance).

Chapter 3

Ambipolar field effect transistor on as-grown single-wall carbon nanotubes

3.1 Electrical properties of semiconducting carbon nanotubes

Semiconducting behavior in carbon nanotubes was first reported by Tans *et al.* [17] in 1998. Figure 3.1 shows a typical measurements of the current (a) and conductance (b) of a semiconducting single-wall carbon nanotubes (SCSWNT) as the gate voltage V_g applied to the conducting substrate is varied. For positive V_g, current is suppressed and it raises gradually for negative V_g, finally saturating at large negative V_g due to the contact resistance between SCSWNT and metallic electrodes. Such transport characteristic imply several important conclusions. First of all, semiconducting and metallic SWNTs can be distinguished due to their different V_g dependance at room temperature. Second, SCSWNTs are p-type at $V_g = 0$ (hole mediate transport in ON state) and third, they can act as a room temperature unipolar field effect transistor (FET). The fact that SWNT can be used as a FET with performances comparable or better than those known from silicon technology [29], opened unprecedent theoretical and experimental work in this field of the carbon nanotube research. Beside numerous technologically opened questions i.e. how to assemble SWNT FETs into a large-scale integrated circuits, finding that SCSWNT behaves as a p-type FET have become a central issue of the research on SCSWNT in the last couple of years. The importance to reveal the origin of this phenomenon lays in the fact that it would give a better understanding on how to improve SWNT FETs performances and build more complicated nano-scale logic circuits.

Although, enormous research have been done to date, this is still an open issue. Several scenarios have been proposed to explain the hole doping in a SCSWNT. Here, we will just mentioned two of them, to which most of the recent research has been devoted.

Experiments have shown [55, 25, 56] that changing a CNT's chemical environment can change the doping of CNTs. Strong evidence to this is large hysteresis observed in air, with shifts of several volts in threshold voltages during V_g cycling. Further investigation showed that the handling of the CNT devices may in addition change the device performance dramatically. For example, exposure to ultra-violet radiation can drive off, most likely oxygen, lowering p doping in a SCSWNT. Adsorbate doping could be sever problem for the application of SCSWNTs in commercial devices where high reproducibility is mandatary [29]. On the other hand, sensitivity of a CNT to chemical environment gives possibility to use them as a chemical sensors [25].
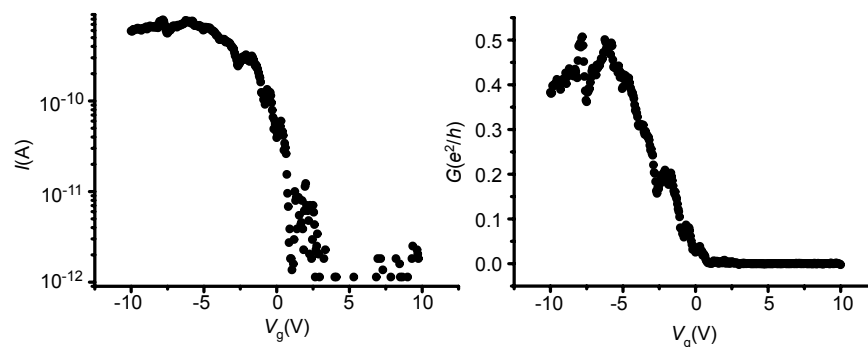
Figure 3.1: (a) Typical I versus V_g characteristic for the unipolar SCSWNT FET. (b) Conductance as a function of the gate voltage for the same device.

The formation of Schottky barriers (SBs) has been suggested as a possible origin for the hole doping in SCSWNTs [57, 58, 59, 54]. It is well known that Schottky barriers (SB) form when a metal and a semiconductor is brought into contact due to differences in their work functions [37]. Similarly, a SB is expected to be formed between a SCSWNT and metallic electrodes. Because of the typically higher work function of CNTs ($\approx 4.5\,\mathrm{eV}$) as compared to metallic electrodes such as Ti *($\approx 4.3\,\mathrm{eV}$), p-type conduction is expected for a SCSWNT. Although, SB have been extensively measured by several groups from low to room temperature, the obtained values for SBs

---

*Note, that for Au work function is $\approx 5.3\,\mathrm{eV}$ and n-type behavior would be expected.

are not conclusive, actually they have been found to vary over several orders of magnitude (1-300 meV) [58]. However, it has been appreciated that different production and processing of the samples can have an important influence on the final characteristic. For example, different growth methods of CNTs can lead to different contact resistances which might hindered the true role of the SBs. A step forward in revealing the origin and control of this phenomena has been done recently by the realization of the ballistic carbon nanotube field effect transistor with palladium contacts [45].

The exclusiveness of p-type SWNT FETs did not persist for long time. In the year 2000, first n-type unipolar FET has been achieved with a controlled chemical doping using alkali metals [60, 61, 62]. Additionally, this work has inspired the creation of p-n junction [30] and p-n-p devices [31]. Recently, an ambipolar field effect action on a SWNT have been accomplished with several different methods. We will address this subject in the following section.

3.2   Ambipolar field effect transistor

Though as-grown SWNTs are p-type, n-type unipolar conductance has been demonstrated by either chemical doping [63] or an annealing treatment in an inert environment [64]. It remains, however, challenging to realize *as-grown* ambipolar SWNT FETs with conventional back-gates. Ambipolar SWNT FETs have been demonstrated on large-diameter SWNTs ($3 - 5$ nm) [65], and recently also on small-diameter SWNTs ($1 - 2$ nm) by using strong-coupling gates [66]. Here we report on electric transport measurements of as-grown SWNTs which display ambipolar FET action. The transport characteristics of a CVD grown SCSWNT at room temperature are shown in Fig. 3.2a and b. A dramatic dependance of the current (a change by several orders of magnitude) through the device is observed upon varying the gate voltage. For large V_g (both positive and negative) the conductance is approximately constant and much larger than for the interval $V_g = 1...10$ V. We assign this reduction of conductivity to the semiconducting gap. Due to a finite conductance observed on both sides of the gap (p- and n-type conduction), this device demonstrates an ambipolar action, i.e. it behaves as an *ambipolar* SWNT FET.

Although, with some repetition from previous chapters, in the rest of the section we will present mainly the low temperature measurements on an ambipolar SWNT FET, which has been published in Nanotechnology, (2003) [67].
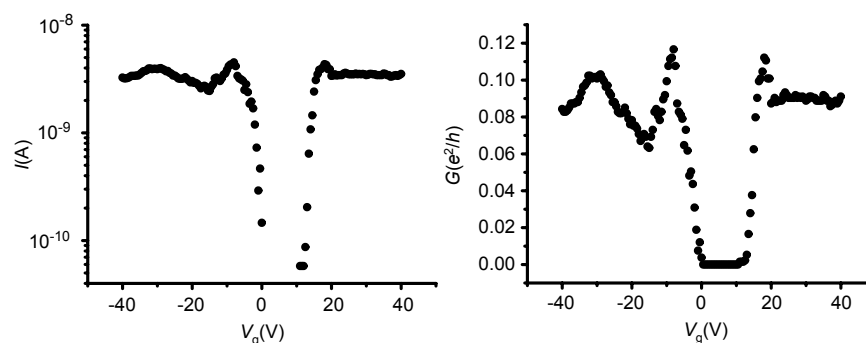
Figure 3.2: The current (a) and the conductance (b) dependance on the gate voltage. Ambipolar FET action is achieved on as grown SWNT.

3.2.1 Experiment

SWNTs are synthesized by chemical vapor deposition (CVD) following the method of Hafner et al. [40]. In all our studies we used SWNTs having diameters of 2 nm or less, as inferred from AFM height measurements. Our devices are prepared on highly doped ($\rho < 0.02\,\Omega$cm) and thermally oxidized (400 nm) Si wafers. The substrate is used as back-gate in electrical measurements of the final devices which are obtained as follows: The substrate is covered with a layer of polymethylmethacrylate (PMMA) in which windows ($5 \times 10\,\mu m^2$) are patterned by electron beam lithography. Then, a catalyst suspension consisting of 1 mg iron nitrate seeds ($Fe(NO_3)_3$) dissolved in 10 ml of isopropanol is poured into the predefined trenches. The PMMA is then removed in acetone, leaving isolated catalyst islands on the surface. The CVD growth is performed in a quartz-tube furnace at 800 °C and atmospheric pressure using a gas mixture of ethylene, hydrogen and argon with respective flow rates of 2, 400, and 600 cm^3/min. During heating and cooling of the furnace, the quartz tube is continually flashed with argon to avoid contamination of the tubes. The as-grown SWNTs are then contacted in a conventional lift-off process with two metal electrodes per SWNT, spaced 1 μm apart. As electrode material a bilayer of Ti (2 nm) and Au (60 nm) is used, leading to contact resistances of $\approx 40\,\mathrm{k\Omega}$ at room temperature. Fig. 3.3a illustrates schematically a SWNT device. An atomic force microscopy (AFM) picture is displayed in Fig. 3.3b. The diameter of the nanotubes is determined from the measured height using AFM in tapping mode.
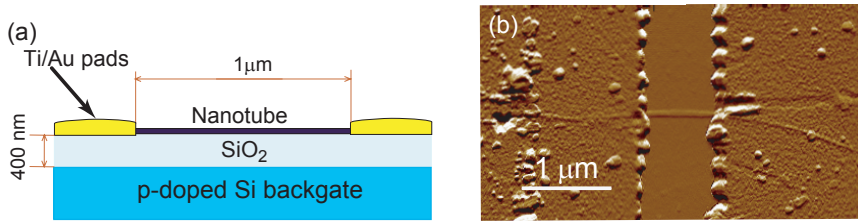
Figure 3.3: (a) Scheme of a SWNT device contacted by two Ti/Au electrodes. The Si substrate is used as back-gate. (b) Atomic force microscopy (AFM) image of a SWNT bridging between the two electrodes.

3.2.2 Results and Discussion

Once the samples are made, semiconducting and metallic tubes are distinguished by the dependence of their electrical conductance G on the gate voltage V_g, measured in a wide temperature range of $0.3\ldots300\,\mathrm{K}$. Fig. 3.4 shows a measurement of the linear conductance $G(V_g)$ for a semiconducting SWNT at moderate temperatures of $T = 40$ and $60\,\mathrm{K}$, respectively. Starting from $V_g = -10\,\mathrm{V}$, G decreases with increasing V_g indicating p-type behavior, while above $V_g \approx 4\,\mathrm{V}$, G increases indicating n-type behavior. In between these two regions the conductance is low, which suggests carrier depletion. This low conductance region corresponds therefore to the gap [65, 68]. The charge-neutrality point for this sample lies at $V_g = 2.5\,\mathrm{V}$. It varies in general between $V_g = -2.5\,\mathrm{eV}$ and $2.5\,\mathrm{eV}$. Our finding demonstrates that as-grown SWNT can be ambipolar transistors.

$G(V_g)$ is slightly lower at $40\,\mathrm{K}$ than at $60\,\mathrm{K}$. If the temperature is lowered further, the linear-response conductance is suppressed further to eventually become very small. This is caused by Coulomb interaction, which first results into a power-law suppression of G with T [69, 70] and at low-temperatures to the emergence of Coulomb blockade. The latter is observed and will be discussed afterwards.

The two-terminal resistance R of a carbon-nanotube device has two parts: the resistance arising from the contacts and a finite mobility (resistivity) of the NT. The relative magnitude is currently discussed. One prominent school of scientist assigns the major part of R to Schottky barriers at the contacts impeding transport and provide some evidence in favor of it [57, 58, 71, 59, 72]. However, the discussed devices have resistances in the range of $1..100\,\mathrm{M\Omega}$, i.e. are rather high-ohmic. The device, which we show in Fig. 3.4, has a lower resistance of order $0.1\,\mathrm{M\Omega}$. Assuming that
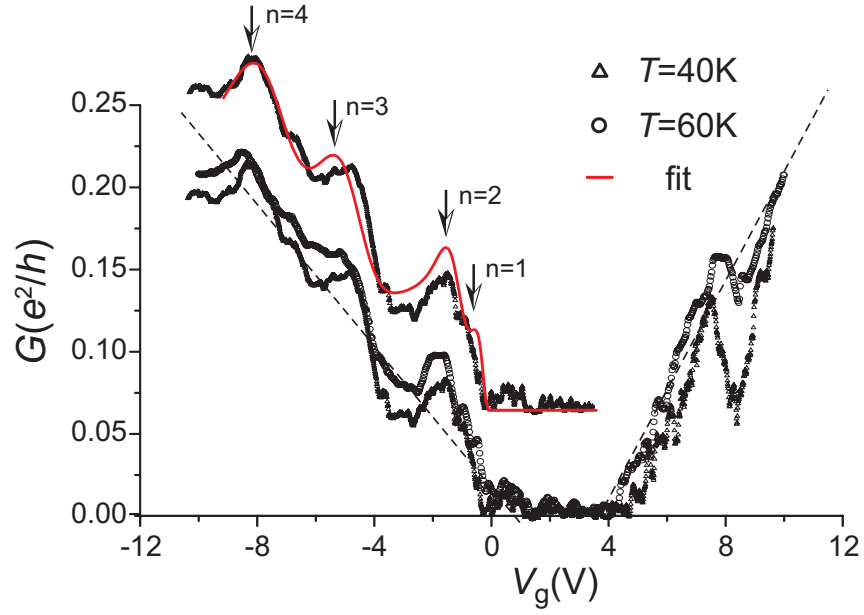
Figure 3.4: Two-terminal (linear) conductance G as a function of gate-voltage V_g for a semiconducting SWNT at moderate temperatures of $T = 40$ and $60\,\mathrm{K}$, respectively. The peaks in G are attributed to van Hove singularities in the one-dimensional DOS. A respective fit to the $T = 40\,\mathrm{K}$ data is shown as a solid curve (shifted vertically for clarity).

the conductance of this devices is limited by scattering within the NT, the mobility μ can be estimated taking a linear approximation of $G(V_g)$ (dashed lines in Fig. 3.4). This yields a relatively high average carrier mobility of $\mu \approx 800$ cm^2/Vs. The mobility can be related to the 1d diffusion coefficient $D = v_F l$ via $D = \mu E_F / e$, where E_F is the Fermi energy, $v_F \approx 10^6$ m/s the Fermi velocity, and l the scattering mean-free path. Taking the approximation $E_F \approx 0.5\,\mathrm{eV}$ yields $D \approx 0.4\,\mathrm{m}^2/\mathrm{s}$ and $l \approx 40\,\mathrm{nm}$. Note, that this estimate results in lower bounds for μ, D, and l, because of (the unknown) contribution to the total resistance from the contacts.

$G(V_g)$ is not strictly linear, but shows several pronounced humps, suggestive of van Hove singularities (VHS) in the density-of-states (DOS) of the 1-dimensional (1D) bandstructure of NTs. The conductance G is proportional to the 1d DOS N_{1D}, both in case of tunneling and low-ohmic contacts, provided the band structure moves rigidly with the gate voltage

(no Fermi-level pinning). The proportionality coefficient is then determined by the tunneling coupling parameter or the diffusion coefficient, respectively. To test this scenario, we have modelled $G(V_g)$ by $G(V_g) \propto N_{1D}(E(V_g))$ and display a fit to the curve at $T = 40\,\mathrm{K}$ at the p-side in Fig. 3.4 (shifted vertically for clarity). There are three fitting parameters: the energy broadening δ, the gate capacitance C_g and the prefactor between N_{1D} and G. δ is determined to be $\delta = 0.13\,\mathrm{eV}$. This is reasonable if we compare with the inverse scattering time, given by $v_F h/l \approx 0.1\,\mathrm{eV}$. C_g determines the horizontal scale of the plot and the prefactor the diffusion coefficient (or the tunneling coupling, if tunneling contacts are assumed to dominate the resistance). We will discuss these scaling parameters (in particular the gate coupling) later, after having introduced the low-temperature measurements.

In fitting the measurement we have used a regular sequence of 1d subbands with threshold energies of $E/E_0 = 1, 2, 4, 5....$ The respective van Hove peaks are marked by arrows in Fig. 3.4. Note, that the first VHS is hardly visible and that the peak spacing on the gate-voltage axis is modified. The latter apparent change is caused by the non-linear E_F vs V_g dependence. We have obtained this dependence assuming that a gate-voltage change leads to charging of the gate capacitance C_g connected in series with the electrochemical capacitance of the NT [55]. The latter is given by the density-of-states. To first order (averaging over van Hove singularities) we obtain $E_F \propto \sqrt{V_g}$.

We now turn to low-temperature measurements $T \leq 4$ K. Figure 3.5 shows $G(V_g)$ and a greyscale representation (inset) of the differential conductance dI/dV as a function of V_g and applied transport voltage V_{sd} of a SWNT device at $T = 2\,\mathrm{K}$. The large white zone in the middle of the greyscale plot corresponds to a non conducting region related to the semiconducting gap. The drawn thick lines at the edges are guides to the eye. Their vertical extensions intersect around $V_{sd} \cong 0.6$ eV, which is a direct estimate of the gap energy. On both sides of the gap Coulomb blockade diamonds (CBD) of varying size are observed (we refer to the term 'diamond', although the blockade region is not composed of a series of neat diamonds). Though the addition energy E_{add} (sum of single-electron charging energy and level spacing) is seen to fluctuate in between $2.5\,\mathrm{mV}$ and $\lesssim 20\,\mathrm{meV}$, there is a general trend, indicated by the thin curved lines. Close to the gap E_{add} is large and decays to smaller value for lower (higher) V_g on the p (n) side. This is not expected for an ideal (*defect-free*) semiconducting NT for the following reason: At the onset of the conduction or valence band, the 1D DOS is expected to be large (VHS), since the band dispersion is parabolic to first approximation. If the NT can be considered as a single quantum dot extending from one contact to the other, the 0D level spacing δE should be very small, i.e. $\delta E = 0$ to first approximation. Provided the
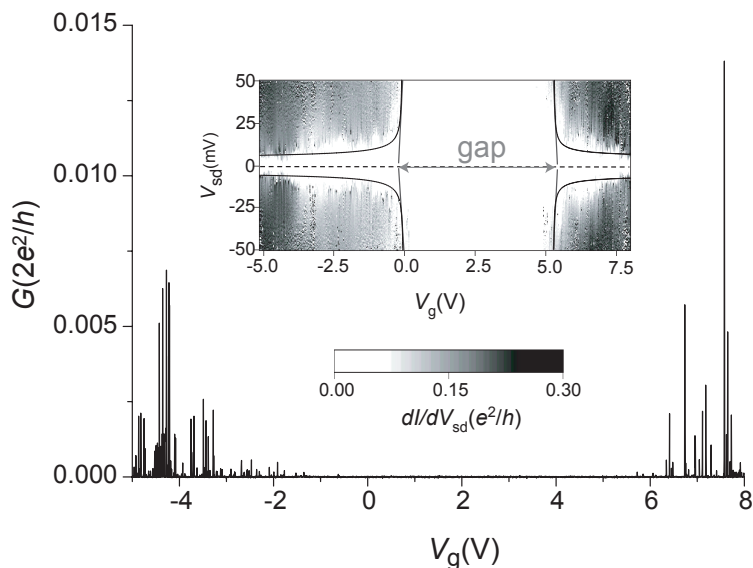
Figure 3.5: Linear conductance G as a function of gate voltage V_g (main plot) and greyscale representation of the differential conductance dI/dV as a function of V_g and applied source-drain voltage V_{sd} (inset) at $2\,\text{K}$ for a SWNT device. White regions correspond to zero and dark regions to high conductances (maximum $0.3\ e^2/h$). The semiconducting gap is clearly visible as a large non-conducting region in the inset. Coulomb oscillations peaks are observed on the p (left) and n (right) side of the semiconducting gap.

added charge can spread homogeneously along the whole tube, a constant charging energy U_c is expected. Hence, we would expect a constant addition energy in case of an ideal defect-free tube, right at the edge of the gap. The observed discrepancy can be resolved (to some degree) if disorder is taken into account. Disorder will distribute the states over some energy interval leading to the observed broadening of the VHS, see Fig. 3.5 Moreover, this results in a smooth onset of the DOS and consequently in a relatively large 0D level-spacing δE. Disorder also (partially) localizes the wavefunctions, leading to both increased δE and U_c.

Next, we focus on the region far away from the gap where ideally the 0D wavefunctions are extended, i.e. one quantum dot, and where the constant interaction model should yield a good approximation to single-electron charging effects. The charging energy is then given by the capacitances determined by the geometry of the device. Fig. 3.6 presents three greyscale

plots of the differential conductance dI/dV, 3.6a and b for one semiconducting NT and 3.6c for another metallic NT with identical contact spacing. The latter is shown as reference. Fig. 3.6a and b correspond to conduction in the p and n region, respectively. Both have been measured around $|V_g| \approx 10\,\text{V}$. If we compare with the metallic reference, the Coulomb blockade (CB) 'diamonds' are less regular in the semiconducting case, in particular they most of the time do not close. Importantly, however, they are similar in all respects on the n and p side. The irregularity of the CB and the fact that the gap most often does not close implies that the NT does not act as a *single* quantum dot. The low maximum conductance of $\leq 0.025\,e^2/h$ observed in the linear conductance in Fig. 3.5 supports this finding. Following the line pattern of conductance onset at finite V_{sd}, the addition energy E_{add} is given by the difference between adjacent maxima and minima of V_{sd}. Hence, E_{add} varies in between $\approx 2...5\,\text{meV}$, as does the additional gap. This suggests that the NTs are split up into two, at most three dots in series. The CB-pattern on the n-side seems to show a beating pattern repeating after $\approx 6 - 7$ added charges. A strong beating pattern on the n-side has been observed before [68] and has been attributed to the formation of a small quantum dot in the vicinity of one of the contacts.

The analysis of CB diamonds permits to extract the factor α [73] which measures the effectiveness of the coupling capacitance between the tube and the gate, i.e., $\alpha = C_g/C = U_c/\Delta V_g$. Here, C_g is the gate capacitance, C the total capacitance (gate plus contacts), $U_c = e^2/C$ the charging energy, and ΔV_g the single-electron period in gate voltage. We estimate the charging energy from the averaged value of the addition energy of a set of Coulomb diamonds. This results in $U_c \approx 2.5\,\text{meV}$ within a gate-voltage period of $\Delta V_g = 12\,\text{mV}$, from which we deduce $\alpha \approx 0.2$. Note, that this is a very high coupling efficiency for a nanotube whose gate-electrode is as much as $400\,\text{nm}$ away.

Provided the constant-interaction model is valid in the semiconducting gap, we can predict the gap size, apparent in V_g. The gap in energy space is given by $E_{gap} = 4\hbar v_F/3d$, yielding $0.7\,\text{eV}$ (the diameter d is taken to be $d = 1.2\,\text{nm}$) [74]. Since the charging energy is negligibly small, $E_{add} = E_{gap}$. Multiplying with the ratio $\Delta V_g/U_c$ yields for the gap-size $\Delta V_{g-gap} = 3.4\,\text{V}$, in reasonable agreement with the observed $\Delta V_{g-gap} \approx 4\,\text{V}$ in Fig. 3.4, or $\Delta V_{g-gap} \approx 5\,\text{V}$ in Fig. 3.5. From α and U_c we obtain for the capacitances $C_g \approx 12.8\,\text{aF}$ and $C \approx 60\,\text{aF}$. C_g is in reasonable agreement with the estimated geometrical capacitance $C_{geometry} = 2\pi L \epsilon_r \epsilon_0 / ln[2L/d]$ (L and d are the length and the radius of the nanotube, respectively), yielding $29\,\text{aF}$. The factor of 2 difference most likely originates from the partial screening by the contacts.

The value of α found here is one of the largest values reported so far [64].

As a reference to our study on semiconducting SWNTs, we have investigated metallic tubes of similar length too. Contrary to semiconducting NTs regular Coulomb blockade diamonds are observed in metallic SWNTs (see Fig. 3.6c). At the edges of each diamond, parallel and sharp lines are visible reflecting excited states of the nanotube quantum dot. The charging energy and the single electron level spacing are found to be $3\,\mathrm{meV}$ and $1\,\mathrm{meV}$, respectively. The latter is in good agreement with the contact separation of $L \approx 1\,\mu\mathrm{m}$. This strongly suggests, that metallic SWNTs behave like single quantum dots, unlike semiconducting SWNTs. In addition, the coupling to the gate $\alpha \sim 0.2 - 0.3$ is equally large and corroborate the universal aspect of the high gate efficiency independent of the nature of the tubes.

Let us finally compare the horizontal axis (the gate voltage) of Fig. 3.4 ($T = 40, 60\,\mathrm{K}$) with Fig. 3.6 ($T = 2\,\mathrm{K}$). The low-temperature data allows to count the added charge accurately. There are 30 electrons added in the gate-voltage interval shown in Fig. 3.6a and b, leading to ≈ 100 electrons per $1\,\mathrm{V}$. This capacitance value is obtained at a relatively high gate voltage of $|V_g| = 9.5 - 10\,\mathrm{V}$. Referring to Fig. 3.4 and applying our assumption that the structure in G is due to the energy-dependence of 1D subbands, we conclude that 4 subbands need to be occupied at this gate voltage. The number of states per unit gate voltage at this Fermi-level (i.e. gate voltage) position can be calculated and amounts to $\approx 5\,10^3\,\mathrm{V}^{-1}$. Hence, we encounter a factor of 50 discrepancy! It may seem tempting to suggest another cause for the apparent oscillation of $G(V_g)$, namely Coulomb-blockade oscillations. The period of CB oscillation of $3.5\,\mathrm{V}$ would correspond to a *very large* single-electron charging energy of $U_c \approx 0.4\,\mathrm{eV}$. If this were the case, G would be strongly suppressed already at $T = 60\,\mathrm{K}$, not to mentioned at $2\,\mathrm{K}$. Note, that the differential conductance is not suppressed if only a small source-drain voltage of a few mV is applied (see Fig. 3.5 (inset)), but is large of order $0.3\,e^2/h$. Therefore, Coulomb blockade can be disregarded as cause for the oscillation of $G(V_g)$ in Fig. 3.4. Since CB can be disregarded and because the 1D DOS in the fit of Fig. 3.4 reproduces the measurement very well, we think that the high-temperature data does reflect the 1d DOS. To get the number of states right, the resistance must be limited by a short section of the tube of length $1\mu\mathrm{m}/50 = 20\,\mathrm{nm}$, which in addition must be located close or possibly even under the contacts in order to screen the Coulomb interaction. At lower temperature this short tube section is not visible in transport, because the resistance is then dominated by the CB of the whole NT. Apparent oscillations in $G(V_g)$ of SWNTs were assigned to the energy dependent 1D DOS by Liu *et al.* [75]. However, no quantitative comparison with the expected DOS was performed. Moreover, the observed 10 'peaks' requires to fill 10 SWNT subbands, which is very unlikely. It seems to us that their result might have the same origin as our.
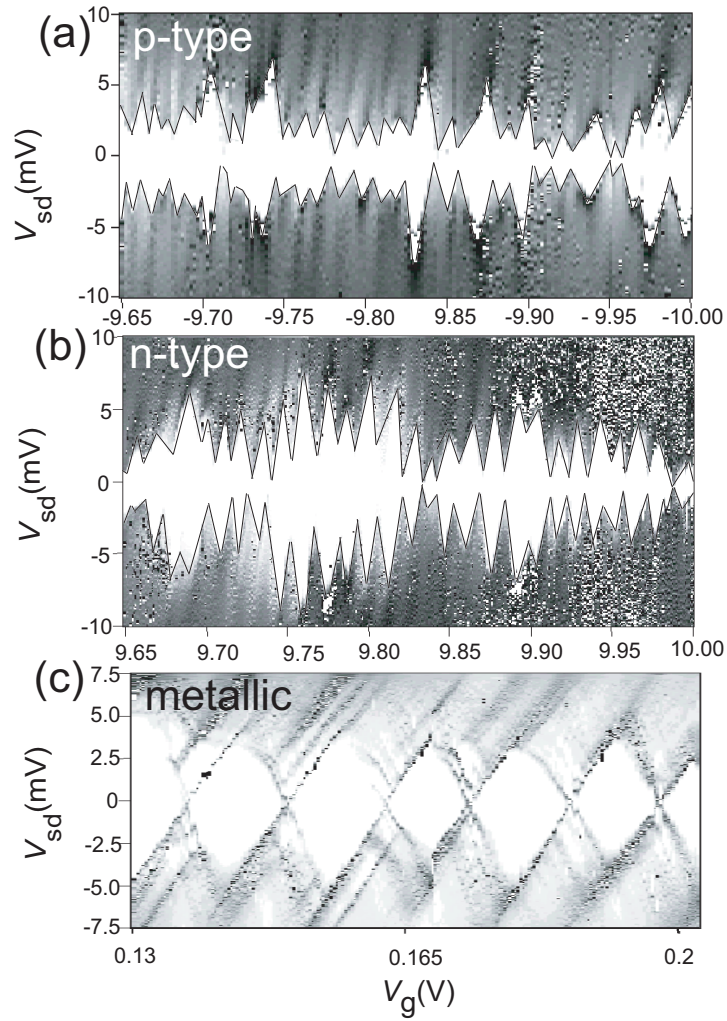
Figure 3.6: Differential conductance (dI/dV) plots as a function of V_g and V_{sd}. White corresponds to $dI/dV = 0$, and black to the maximum conductance of $0.3\,e^2/h$. (a) and (b) have been measured on one semiconducting SWNT in the p region (a) and n region (b) at 2 K. As a reference a similar plot of another metallic SWNT measured at 0.3 K is shown in (c). While excited states can clearly been seen in (c), they appear to be absent in (a) and (b). Furthermore, while (c) displays a regular Coulomb blockade (CB), it is irregular in (a) and (b). In all cases strong coupling to the gate is inferred.

3.3   Conclusions

In conclusion, we have shown that CVD-grown SWNTs, used as-grown, can display high coupling strength to a back-gate. The strong coupling enables to sweep the Fermi-level continuously from p to n-side, so that these field-effect transistors are ambipolar. At intermediate temperatures the overall two-terminal resistance R appears to be determined by a short tube segment close to the contacts, leading to the appearance of 1d DOS effects (van Hove singularities) in the linear conductance G versus gate voltage V_g. In contrast, at low-temperature the average resistance R is higher and determined by the whole nanotube, notably by single-electron charging. The observed fluctuating addition energy points to disorder which (partially) splits the tube in $1-3$ segments. As the maximum number of dots ≤ 3 at a contact separation of $L = 1\,\mu$m, it appears that single quantum dots should be feasible at smaller contact separations ($L \lesssim 300\,$nm). We emphasize that G can be swept from the p to the n side even at $T = 2\,$K with no apparent barrier. As inferred from non-linear transport any barrier must be smaller than $\lesssim 2\,$meV. Similarly low barriers were also observed in the work of Martel *et al.* [58]. These authors argue that the barriers originate from the metal-nanotube contact and are Schottky barriers which are expected to be large, i.e. of order $0.3\,$eV. The observed conductance at low temperature can only be reconciled with large Schottky barriers, if the barriers are so short that tunneling through them is permitted. The band-bending within a SWNT at the metallic contacts have been studied theoretically by Léonard and Tersoff [76, 77]. It is concluded that the depletion region can be sufficiently short (< 5Å) to permit sizable electron tunneling, provided the doping fraction (or carrier density) of the NT is sufficiently large, i.e. $f \gtrsim 10^{-3}$. As an estimate, the carrier density at $V_g = 10\,$V corresponds to a of charge fraction of $f \approx 10^{-3}$, which is in favour of short barriers. Similar doping density were inferred from electrochemical gating experiments of MWNTs [55].

Chapter 4

Single-wall carbon nanotubes as quantum dots

In the past decade, transport measurements have emerged as a primary tool for exploring the electrical properties of structures on the nanometer scale. Due to their unique electronic bandstructure, much attention has been focused on carbon nanotubes (CNTs) [35]. For metallic single wall carbon nanotubes (SWNTs) just two spin degenerate one-dimensional (1D) modes should govern their transport properties at low energies, which makes them interesting model systems to explore the physics in reduced dimensions [16].

Due to the finite length, given by the lithographically fabricated contacts on opposite sides of the CNT (two-terminal device with source and drain contacts), the one-dimensional CNT will be turned into a quantum dot [47] at low temperatures (typically at $\sim 10\,\mathrm{K}$), i.e. into a zero-dimensional object with a discrete level spectrum. The confinement is formed by the finite back-reflection at the edges of the contacts. The level spacing δE is determined by the contact separation L and is inversely proportional to it. This particle in the box-model holds provided the level-broadening Γ and the temperature are both smaller than δE. Γ describes the life-time broadening proportional to the coupling strength to the leads.

Until now, three transport regimes have been identified in SWNTs: A) single-electron tunneling [78, 79, 73, 80], which is dominated by the on-site Coulomb repulsion expressed by the energy term $U_c = e^2/C$, where C is the total capacitance; B) the regime of correlated electron transport, in which higher-order tunneling processes, so-called co-tunneling [81], are appreciable, leading to the emergence of the Kondo effect [82, 83]; and C) the open SWNT for which Coulomb interaction may be neglected and the residual gate-dependence of G can be described as in a tunable Fabry-Perot resonator [21]. A) holds for low, B) for intermediate and C) for high transparent contacts.

As in atoms, eigenstates in quantum dots (QDs) may be degenerate due to symmetries and together with the spin degeneracy and Pauli principle lead to the formation of electronic shells. Indeed, striking shell patterns have been observed in QDs [84, 85]. The eigenstates (Bloch-states) at the Fermi energy of graphene (two-dimensional sheet of graphite) is two fold degenerate. The two wave functions correspond to the two carbon sublattices (the unit-cell is composed of two C-atoms). This degeneracy is preserved in CNTs and should therefore lead to two degenerate orbitals in a finite-length nanotube in 0D. Together with the spin degeneracy, the shells are expected to be four-fold degenerate. This shell pattern has recently been observed by Buitelaar and coworkers [86] in multi-wall carbon nanotubes (MWNTs) and by Liang *et al.* in SWNTs [87]. Within one shell the ground-state spin was shown to follow the sequence $S = 0 \rightarrow 1/2 \rightarrow 0 \rightarrow 1/2$ in the former work, whereas a possible triplet ground state for two added electrons was suggested by the latter authors, i.e. the sequence $S = 0 \rightarrow 1/2 \rightarrow 1 \rightarrow 1/2$.

Here we focus on CVD-grown metallic carbon nanotubes (CNTs). We will first introduce the concept of QDs and Coulomb blockade. In this regime (low transparency), at low temperatures we observe characteristic features of single-electron tunneling. At intermediate transparency the Kondo effect emerges. In this regime, we examine the four-fold shell pattern in great detail and demonstrate that the half-filled ground state (i.e. 2 electrons added to an empty shell) is either the spin singlet with $S = 0$ or the six possible states are effectively degenerate due to a level broadening exceeding the orbital mismatch and exchange energy.

We will also present deviations from the expected shell filling when the orbital degeneracy is lifted. Furthermore measurements on several samples show striking gaps around zero bias. These gaps can not be accounted for within simple shell filling model. This anomaly is at present not understood.

In the final section, we present a sample where the coupling is so high that the levels start to overlap. Unlike the results observed in previous work [21], in which a weak periodic conductance modulation was found, we observe sharp resonances superimposed on a slowly varying background. These latter resonances can be understood as an interference effect and are known as Fano resonances [88, 89].

The SWNT devices

Single wall carbon nanotubes (SWNTs) have been grown from patterned catalyst islands by the chemical vapor deposition method on Si/SiO_2 substrates as described in Chapter 2. The degenerately doped silicon, terminated by a 400 nm thick SiO_2 layer, is used as a back-gate to modulate the electrochemical potential of the SWNT electrically contacted with a source

and drain terminal. The contacts are patterned by electron-beam lithography (EBL) using polymethylmethacrylate (PMMA) as resist, followed by metallization and lift-off. Once the samples are made, semiconducting and metallic SWNTs are distinguished by the dependence of their electrical conductance G on the gate voltage V_g measured at room temperature ($T \approx 300\,\mathrm{K}$).

Detailed electrical characterization of the devices has been performed at low temperature in a ^{3}He system at $300\,\mathrm{mK}$. We measure the electrical current I with a low noise current to voltage amplifier as a function of source-drain (V_{sd}) and gate (V_g) voltage and determine the differential conductance $G_d := \partial I / \partial V_{sd}$ numerically. Finally, the collected data $G_d(V_{sd}, V_g)$ are represented in a two-dimensional grey-scale representation in which the grey-scale corresponds to the magnitude of G_d. The linear-response conductance $G := I/V_{sd}$ with $V_{sd} \to 0$ is measured at a small but finite source-drain voltage of $40\,\mu\mathrm{V}$. The electric circuit diagram for a quantum dot (CNT) is illustrated in Fig. 4.1. Details about device fabrication and transport measurements are described in appendix A.
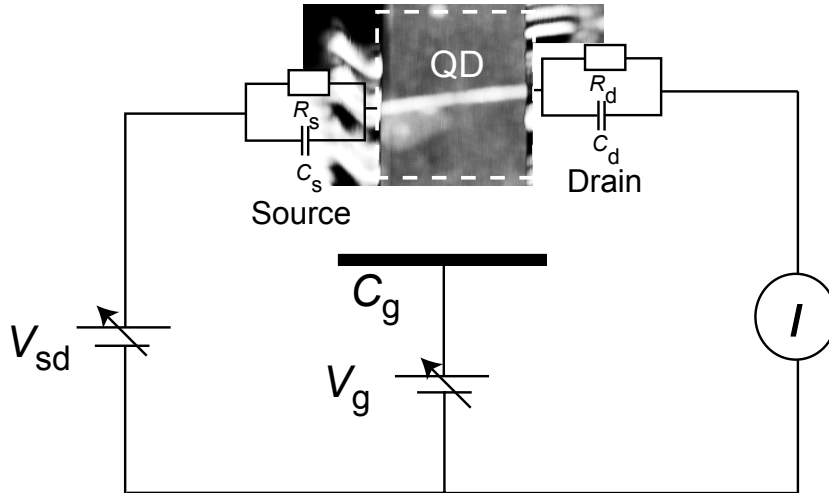

Figure 4.1: Electric circuit diagram for a quantum dot (CNT), with source and drain electrodes. Each contact between a QD with the source or drain electrode can be characterized by a RC junction. The gate voltage V_g couples only capacitively to the QD through the capacitance C_g.

4.1   Coulomb blockade

4.1.1   Introduction

Quantum dots (QDs) are small droplets of electrons, confined in three spatial directions. Energy and charge quantization result from this confinement. Because of the striking similarity with atoms, they are also named 'artificial' atoms. The analogy between 'real' and 'artificial' atoms has been exploited, both theoretically and experimentally. The main difference is in the energy scale. It is few orders of magnitude bigger for 'real' atoms. As in atomic systems, the electronic states in QDs are sensitive to Coulomb interaction. Once a carbon nanotube is attached to the leads with tunneling barriers it can behave as a QD. The scheme of a nanotube QD coupled with to two metallic leads (source-drain) is illustrated in Fig. 4.2a. The metallic electrodes impose boundary conditions on the k values along a CNT. This will lead to discrete values of the allowed wave-vector which results in energy quantization. The quantization of energy due to spatial confinement is shown in Fig. 4.2b for the two lowest energy lying subbands in a metallic SWNT. When the tunneling barriers are sufficiently high, electronic transport at low temperature is determined by two main effects: single-electron charging and the energy level quantization. Low temperature transport measurements, can provide detail information on the level structure and the underlying symmetry (shell structure). We will show that energy spectra found in a nanotube QD can be explained assuming a simple constant interaction model for Coulomb blockade regime [90].
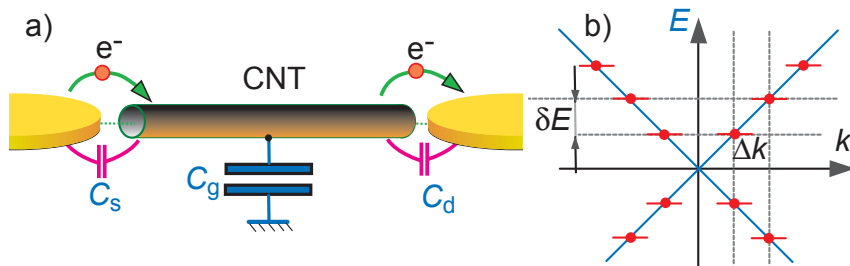
Figure 4.2: Schematic illustration of uncorrelated sequential electron tunneling through a nanotube QD. (b) Energy level quantization δE in a metallic SWNT due to spatial confinement along the nanotube.

4.1.2 Coulomb blockade theory

There are several excellent reviews on theoretical and experimental aspects of the Coulomb blockade (CB) phenomenon in mesoscopic devices [9, 78, 79, 73, 80]. In this section we will just briefly discuss the conditions when the Coulomb blockade regime is relevant and derive the main energy scales for a SWNT QD.

A CNT device that is connected via tunnel barriers to source and drain electrodes resemble a QD. Because of on-site Coulomb repulsion, the addition of an electron to a QD implies an energy change of $U_c = e^2/C$, where C is the total capacitance of the QD. This is known as a constant interaction model (CIM) of CB, where all electrostatic interaction on the QD is described by macroscopic and constant capacitance C [9].

The Coulomb blockade regime is relevant only when the number of electrons (N) on a QD is a well defined integer. This situation occurs when the tunnel barriers between a CNT and the contacts are sufficiently opaque that random changes of N are forbidden. From Fig. 4.1 it follows that the tunnel barriers are characterized by the capacitances C_s, C_d and resistances R_s, R_d to the corresponding leads. The condition that quantum fluctuation in the number of electrons on a QD is small, is satisfied if $R \gg R_Q = h/e^2$, where $R = R_s + R_d$ is the resistance of the whole CNT device and R_Q is the so-called *quantum resistance* [9, 78, 79].

The possibility to observe the Coulomb blockade effects is determined primarily by the capacitance of the QD device. The total capacitance of a metallic SWNT which forms a QD is given by (Fig. 4.1) $C = C_s + C_d + C_g$. As a first approximation, C_g can be estimated from the geometrical capacitance of a SWNT. For a metallic SWNT embedded in a dielectric ε_r, the gate capacitance is given by $C_g = 2\pi\varepsilon_0\varepsilon_r L/ln(2L/d)$ [91], where d and L are respectively diameter and length of a SWNT. For typical values: $\varepsilon_r = 4.4$ [92], $L \approx 1\,\mu$m and $d = 1.5\,$nm one obtains $C_g \approx 35\,$aF and a charging energy $U_c \approx 5\,$meV. This simple estimate shows that the CB regime should be easily accessible at low temperatures ($T < 60\,$K).

Except for the quantization around the circumference of a CNT, the finite length (contact spacing) of a CNT impose an additional quantization along it physical axes. The energy level spacing due to the spatial confinement δE is determined by the length L of CNT and the Fermi velocity $v_F = 8 \times 10^5\,$m/s. For a "particle-in-a-box" approximation, the level spacing derived from the linear dispersion relation for a metallic SWNT has the following form [17]

$$\delta E = (dE/dk)\Delta k/2 = \frac{hv_F}{4L}, \qquad (4.1)$$

where h is the Planck's constant and it is assumed here that orbital degen-

eracy is lifted.

The energy level filling in a QD can be described with the so-called addition energy ΔE. In the case when all degeneracies are lifted, the addition energy is simply given by the sum of the charging energy and the level spacing,

$$\Delta E = U_c + \delta E. \tag{4.2}$$

From Eq. 4.2, it follows that CB regime can be described with just two energy scales, U_c and δE. This is the main result which follows from the constant interaction approximation for CB. We will extensively use this approximation in the discussion of our experimental data. However, this assumption will be refined when we take into the account orbital and spin degeneracies in CNTs.

Full spectroscopy on a QD in the CB regime can be obtained if $k_B T < U_c$, δE. This is the so-called quantum regime of CB, where the electron transport occurs through an individual quantum level. Due to resonant tunneling [9] conductance G in the linear response ($V_{sd} \rightarrow 0$) displays the so-called Coulomb blockade peaks upon varying V_g. This can be understood following the illustrations in Fig. 4.3(a-c). The transport through a QD can be alternated by tuning V_g. The addition energy gap (ΔE) forbids electrons to jump on and off the QD (4.3a). By changing V_g, the electrostatic potential of the QD (ϕ_N) can be changed in such a way that one of the states now lies between μ_S and μ_D allowing electron to jump from the source to the drain electrode via the dot (4.3b). The current will flow until the chemical potential of the QD is changed again, leaving the QD with a $N+1$ or $N-1$ electrons (4.3c). The continuous change of V_g leads to periodic CB-peaks which appear at discrete gate voltages (4.3d). The period of CB-peaks is given by [73]

$$\Delta V_g = \frac{C}{eC_g}\Delta E = \frac{e}{C_g} + \frac{\delta E}{\alpha e}. \tag{4.3}$$

where we have defined the factor $\alpha \equiv C_g/C < 1$. The factor α converts a change in the gate voltage to a change in the electrochemical potential on a QD. In simple words, it describes the strength of the coupling between a QD and a gate.

The characteristics of the CB-peaks is now discussed. For an asymmetric double barrier structure, at $T = 0$, the full width at half maximum (FWHM) of the resonance Γ, is given by the sum of the coupling to left Γ_l and right Γ_r leads [9]. At finite temperature, the Fermi distribution of electrons in the reservoirs yields thermally broadened peaks [73]. The peak in the conductance in the CB regime can be expressed by [79],

$$G_{peak}(V_g) = \frac{1}{k_B T} \cosh^{-2} \frac{e\alpha(V_g - V_g^{res})}{2k_B T}, \tag{4.4}$$
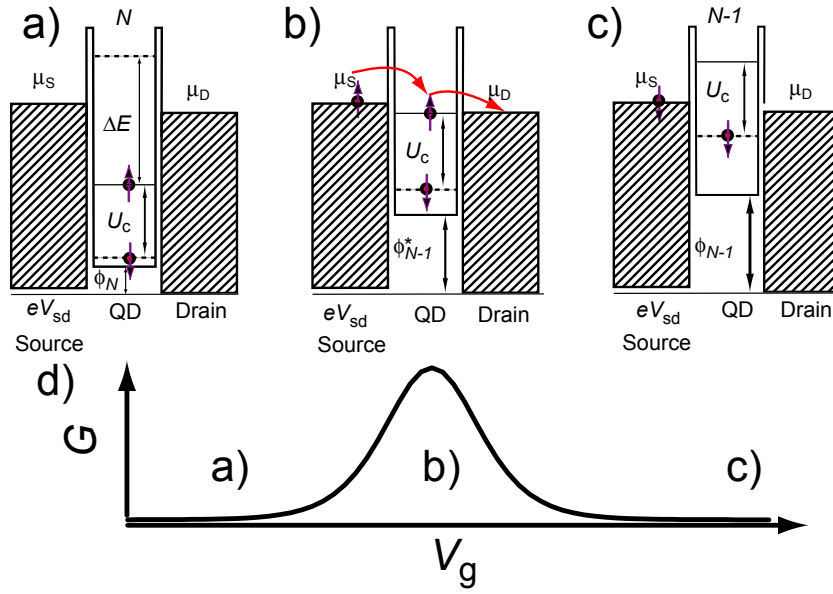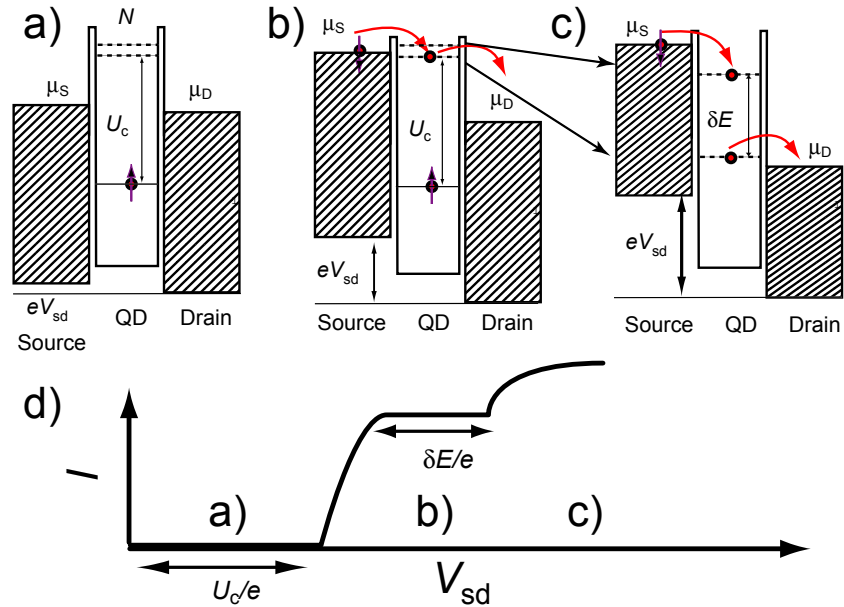
Figure 4.3: Schematic diagram of a quantum dot in the Coulomb blockade regime. Influence of the gate voltage on the transport through a QD is discussed. The quantum dot has discrete, spin degenerate, energy levels. Two tunnel barriers isolate the QD from the source and drain reservoirs with chemical potentials μ_S and μ_D, respectively. (a) The quantum dot has N electrons and the gap energy between highest populated level and the first unoccupied one is ΔE. For small source-drain bias, transport through the QD is forbidden. (b) Energy levels can be moved with changing electrochemical potential of the QD. Once an energy level is lying between μ_S and μ_D, a single electron transport occurs. In this case, the number of electrons on the QD alternate between N and $N-1$ making transport through QD possible. (c) If the chemical potential on the QD is changed even further, the level is no more in the bias window and transport ceases, leaving the QD with $N-1$ electrons. (d) Conductance versus gate voltage characteristic for the SET effect corresponding for the situation from (a-c).

where V_g^{res} determine the peak position for resonant tunneling. Eq. 4.4 reflects the derivative of the Fermi function in metallic leads and has FWHM of $\Delta V_g^{FWHM} = 3.5 k_B T / e\alpha$. From Eq. 4.4 it is evident that CB-peak in this regime should scale as $G_0 \sim 1/T$, where G_0 is the maximum conductance of the CB-peak. At the lowest temperatures for the tunneling through a single electron level, G_0 is expected to saturate (order of e^2/h) and peak

width should saturate to value of the energy level width Γ.

An increase of the bias voltage can also induce a change in the electron number on a QD. For a sufficiently large difference between the Fermi energies in the leads ($E_{F1} - E_{F2} > U_c$), one or more energy levels in the QD become available that SET can occur. This situation with the corresponding $I - V_{sd}$ characteristic is illustrated in Fig. 4.4a-d.

Figure 4.4: Schematic diagram of a quantum dot in the Coulomb blockade regime upon a change in the bias voltage. (a) For small source-drain bias (eV_{sd}), the electron transport is not allowed because there is no available level in the bias window. (b) Applying a large eV_{sd} the bias window extends to include the first unoccupied level in the QD. (c) Further increase in bias enables one to probe directly the level spacing in the QD. (d) Conductance versus bias voltage for the SET effect.

4.1.3 Experiments in the Coulomb blockade regime

The samples presented in this section are contacted with Ti/Au bilayer, where the contact separation amounts to $L \sim 1\,\mu$m. In Fig. 4.5a a low temperature measurements is shown of a metallic SWNT in the Coulomb

blockade regime. In the plotted V_g range ($\Delta V_g = 2\,\text{V}$) more than hundred CB-peaks appear. The conductance dependence versus temperature ($T \lesssim 10\,\text{K}$), is shown for several CB-peaks in Fig. 4.5b. One can see that the CB-peaks are getting more pronounced with decreasing temperature. Their hight increases and width reduces. This already suggests that resonant tunneling occurs through a single energy level. A continuum of energy levels would lead to a constant, temperature independent maximum conductance [78].
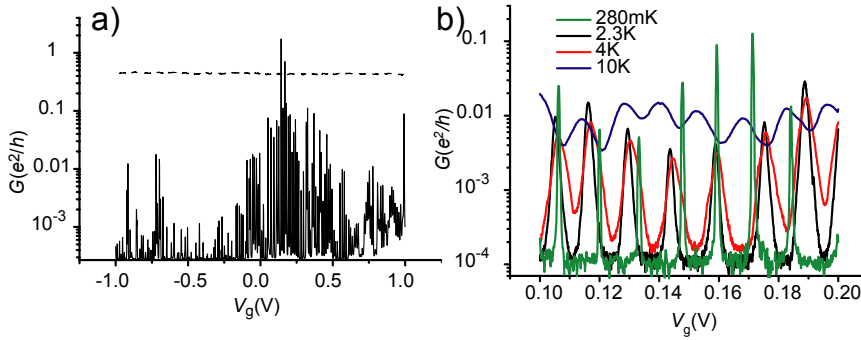
Figure 4.5: (a) Conductance G versus V_g at T=300 K (dashed line) and T=2.3 K (full lines). Pronounced CB-peaks are observed at low temperature. (b) The low temperature dependance of the conductance vs. V_g for several CB-peaks.

For a more quantitative analysis we will concentrate on the temperature dependance of a single CB-peak shown in Fig. 4.6a. The conductance of the CB-peak increases while its FWHM decreases if the temperature is lowered. The measured data are represented by symbols and solid curves are fits to Eq. 4.4. The fitting parameters are G_0, T and α. At the lowest temperature ($T \approx 300\,\text{mK}$) a very high conductance ($G \approx e^2/h$) is observed, proving that we indeed observe tunneling through a single quantum level. Since the contact separation for this device is $L \approx 1\,\mu\text{m}$ we conclude that the mean-free path in the measured SWNT is $l_e > 1\,\mu\text{m}$. This is in agreement with theoretical calculation and previous experimental observations [93, 66].

In Fig. 4.6b, the maximum conductance of the CB-peaks is plotted versus inverse of the temperature. The full line represents a linear fit which is expected from relation 4.4. Additional information can be obtained from the temperature dependance of the CB-peaks width. The FWHM of CB-peak is obtained from fits to a Breit-Wigner type of curve (Lorenzian), which describes tunneling through a single resonant level. In Fig. 4.6c the measured data for the width of CB-peak are plotted versus temperature and
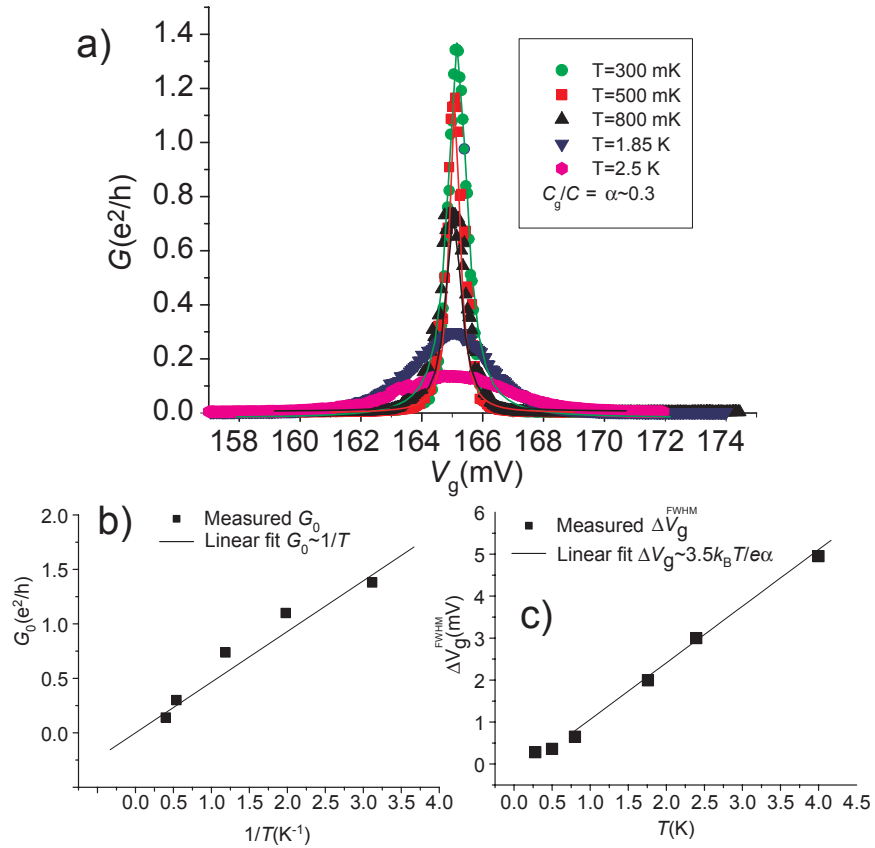
Figure 4.6: (a) Linear conductance of a SWNT QD as a function of the gate voltage and temperature. The symbols represent the measured data and the solid lines are fits to Eq. 4.4. (b) The conductance maximum of the CB-peaks (G_0) versus $1/T$. (c) The temperature dependance of FWHM of the CB-peak. The solid lines are linear fits to Eq. 4.3. From the fitting a coupling to the gate $\alpha \approx 0.3$ is extracted.

the full line is a linear fit to Eq. 4.4. The FWHM reduces linearly with lowering the temperature, as expected for the thermally broadened CB-peak (see Eq. 4.4). However, at the lowest temperature, we observe a saturation in the CB-peak width. This most likely reflects the intrinsic broadening of the quantum level Γ. From the linear fit of temperature dependance of the FWHM CB-peak, one can also extract the coupling to the gate, α. We

obtain $\alpha \approx 0.3$ assuming that the measured and electronic temperatures are equal. Note that this value indicates a very efficient coupling to the gate ($\alpha_{max} = 1$), which is also evidenced in a small period of CB-peaks as a function of the gate voltage ($\Delta V_g \approx 15$ meV). Once we know α and ΔV_g we can estimate the addition energy using Eq. 4.2, $\Delta E \approx \Delta V_g \cdot \alpha \approx 4.5$ meV. This is in fair agreement with the addition energy estimated from the contact spacing $\Delta E \approx 6$ meV.

Although, the gate dependence in the linear transport regime provides essential information about a QD, full spectroscopy can be obtained by acquiring a grey-scale plot, where differential conductances are represented as a function of both V_g and V_{sd}. The Coulomb blockade regime in a grey-scale plot shows up as a diamond like structure (Coulomb blockade diamonds) [9]. A typical grey-scale plot for yet another sample with the same contact separation as before is shown in Fig. 4.7. The important energy scales are indicated in the figure.

Inside the Coulomb blockade diamonds, no current flows through the device. The trace in the gate near zero bias is shown in Fig. 4.7b, where the finite conductance is recovered at degeneracy points as previously explained. The non-linear regime can be explored by fixing the gate voltage (for example in the middle of the Coulomb blockade diamond) and taking traces of dI/dV_{sd} versus V_{sd}. For small bias voltage ($V_{sd} < U_c/e$), the current through the device is blocked. However, at finite bias ($V_{sd} > U_c/e$) the current starts to flow i.e. the off set of the Coulomb blockade diamond directly reflects the charging energy. The $I - V_{sd}$ characteristic corresponding to this situation is shown in Fig. 4.7c as a black curve. From the grey-scale plot, the conversion factor α is easily deduced: $\alpha = U_c/e\Delta V_g \approx 0.3$. This is in excellent agrement with the value obtained from the analysis of individual Coulomb blockade peaks as previously described. In this way we can determine the conversion factor α without knowing the specific values of the capacitances in our system. Moreover, in the non-linear regime ($eV_{sd} > U_c$), one can probe the excited states of a QD. As illustrated in Fig. 4.4, every time when a new level enters the bias window, one more channel is available for transport through the QD. In this case current makes step-like jumps which appear in the differential conductance as sharp peaks. The additional lines outside the Coulomb blockade diamond in Fig. 4.7a correspond to such conditions. These excited states directly give access to the energy level spacing in the QD (as indicated in Fig. 4.7a). From the grey-scale plot the average level spacing is estimated to be $\delta E \approx 1$ meV. Inserting in Eq. 4.1 the length of the device $L = 1\,\mu$m, the level spacing of $\delta E = 0.8$ meV is obtained. The agreement with the measurements is good. This suggests that the QD is defined by the contact separation (edge-to-edge).
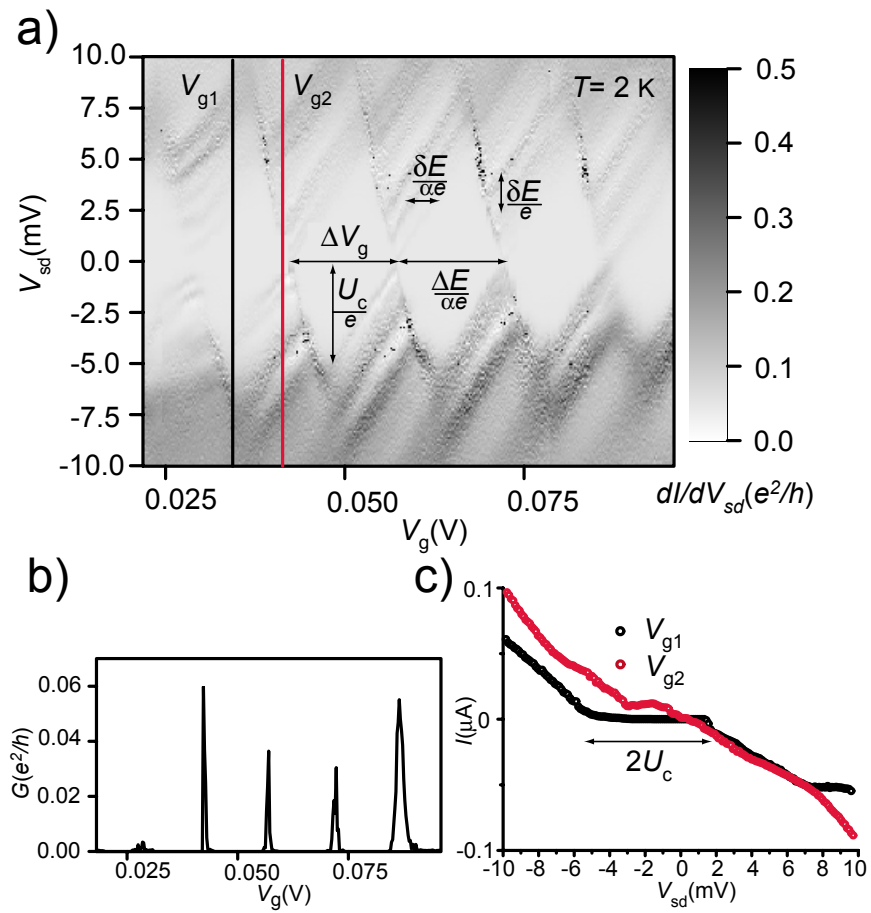
Figure 4.7: (a) A grey-scale plot of the differential conductance dI/dV_{sd} for a SWNT with contact separation $L \sim 1\,\mu m$ at $T = 2\,K$. The charging energy, the energy level spacing and the conversion factor α can be deduced as indicated in the plot. (b) The linear response for the same region in V_g as in (a). (c) $I - V_{sd}$ characteristics for the specific gate voltages indicated in (a).

4.2 The Kondo effect

We have seen in the previous section that tunneling barriers which are formed at the contacts determine the transport phenomena at low temperatures. In the Coulomb blockade regime electrons tunnel one by one. This is the lowest order of perturbation theory. However, when the transparency between the contacts and a QD is increased, higher-order tunneling processes i.e. cotunneling can play an important role. For QDs with large tunnel barriers at the contacts, such processes are hindered, because the simultaneous tunneling of two electrons is proportional to $\boldsymbol{T}^2$. When the transparency between the contacts and a QD is increased, the Heisenberg uncertainty relation allows the electron on the dot to tunnel to one of the leads and to be replaced by another electron from the leads via virtual state on a QD (although, the energy level of the electron ϵ_0 is well below the Fermi energies in the leads). The time scale for such cotunneling process is $\sim \hbar/U_c$. One can distinguish two cotunneling regimes: elastic and inelastic cotunneling processes. Elastic tunneling does not change the energy on a QD and is mainly responsible for transport off-the resonance at low bias (for example inside Coulomb blockade diamond). Inelastic cotunneling processes leaves a QD in an excited state. The condition to observe this process is $eV_{sd} \geq \Delta_{co}$, where Δ_{co} is the lowest on-site excitation energy. Note, that these processes are very general and do not depend on the number of electrons or the total spin of a QD [81]. However, when the spin on a QD is finite, spin-flip cotunneling processes add up coherently leading to the appearance of a narrow peak in the density of states (DOS) right at the Fermi level at sufficiently low temperatures. This is the *Kondo effect.*

4.2.1 Phenomenology of the Kondo effect

The Kondo effect was introduced about forty years ago to explain the resistivity minimum at low temperatures observed in nobel metals with a minute fraction of magnetic impurities [94]. The detailed microscopic theory explains this effect as follows: when the temperature T decreases below the so-called Kondo temperature T_K, the localized magnetic impurity starts to interact strongly with surrounding electron cloud, which finally results in a singlet many-body ground state (as illustrated in Fig. 4.8a), reaching its maximum strength at $T=0$ K. The increase in the sample resistance is explained as a consequence of magnetic impurity acting as scattering center for conducting electrons. This is illustrated in Fig. 4.8b with characteristic logarithmic increase of the resistance below T_K [94].

The unambiguous experimental detection of the Kondo effect in quantum dots structured in 2DEG [82, 95] and recently in CNTs [23] revived

the interest for this phenomenon. In contrast to the CB regime which only probes the electrons confined on a QD, the Kondo effect incorporates coherently delocalized electrons in the leads. The Kondo effect in QDs has different behavior compared to traditional Kondo effect mentioned above. The main phenomenological difference is that the resistivity increases for metals with magnetic impurities while in a QD the Kondo effect leads to increase in the conductance for temperatures below T_K as illustrated in Fig. 4.8c.

This effect can be described in an elegant way, by the use of the Anderson impurity model with single localized state. In the Anderson model, electrons on the quantum dot are described as a single localized state, coupled by tunneling barriers to two electron reservoirs. The electron in this state has an energy ϵ_0. The state has Lorenzian broadening with a full width at half maximum (FWHM) defined as Γ, which characterizes the contact barriers with their finite tunneling rates $\Gamma/h = \Gamma_l/h + \Gamma_r/h$. As we mentioned previously, open contacts (larger Γ) allow higher order tunneling processes to occur. In the case when the total spin on a QD has non-zero value cotunneling events will lead to spin-flipping processes. In that case, a narrow peak in the density of states (DOS) appear right at the Fermi level, forming the so-called Kondo resonance. This is illustrated in Fig. 4.8d. Appearance of the resonance in the DOS will enhance the electron transport through the QD, leading to increase in the conductance.

A detail quantitative description shows that the new ground state of the Kondo system can be described by the Kondo temperature T_K which can be expressed by three QD parameters [96, 97]:

$$T_K = \sqrt{U_c \Gamma} e^{\pi \varepsilon_0 (\varepsilon_0 + U_c)/U_c \Gamma}/2k_B. \tag{4.5}$$

For $T > T_K$ the singlet ground states is destroyed and conductance is attenuated. Out of equilibrium, when a bias voltage V_{sd} is applied the Kondo peak splits into two peaks, each one pinned to the chemical potential of the metallic leads [98]. In this situation, the electrons at the Fermi level in the higher energy lead can no longer resonantly tunnel into the enhanced DOS in the lower energy lead, which suppress the conductance. A magnetic fields alters the Kondo effect in the following way. The unpaired localized electron state splits in an applied magnetic field into the so-called Zeeman doublet. This also splits the Kondo resonance in the DOS into two resonances below and above the Fermi energy in the leads.

In QDs the Kondo phenomenon can be studied with many tunable parameters which are elusive in magnetic alloys. The spin on the QD is tunable by changing the chemical potential for example by a nearby gate electrode, the voltage difference can be applied to the leads exploring non-equilibrium
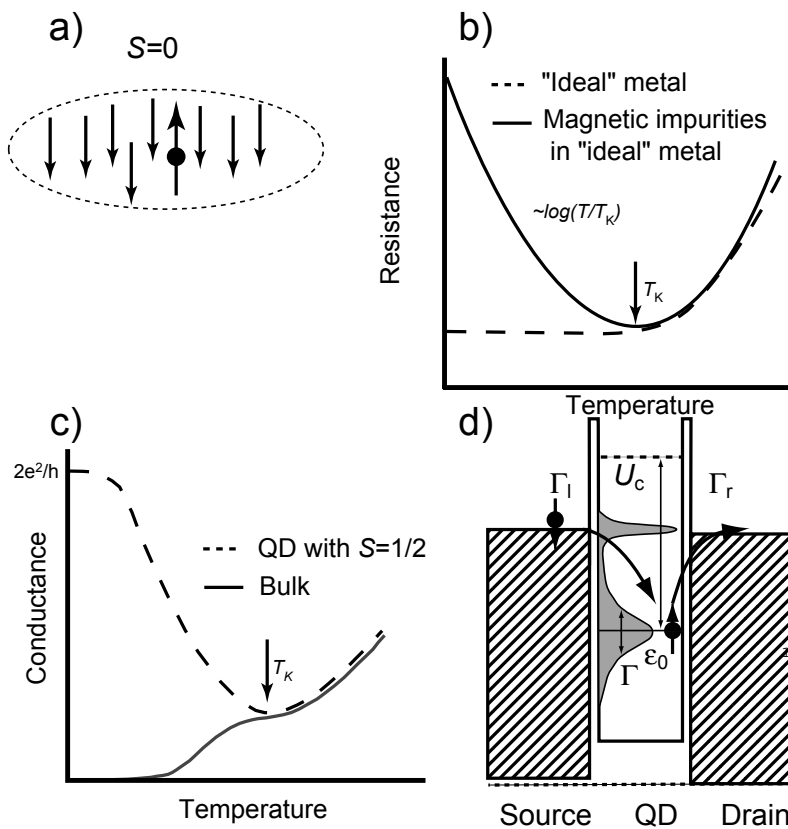
Figure 4.8: (a) The spins of the conduction electrons screen a localized magnetic impurity. (b) The resistance versus temperature for different metals. Ideal metal (for example gold) is shown with dashed line where at low temperatures resistance reduces to constant value. With solid line R-T characteristic is shown for a metal with magnetic impurities. Note the increase in the resistance below the Kondo temperature. (c) The conductance versus temperature for the Kondo effect in a QD with finite spin ($S = 1/2$) is shown with dashed line. Unlike, for the "bulk" Kondo effect (solid line) which decreases, the Kondo effect in a QD with localized spin leads to increase in the conductance below T_K. (d) Schematics of a QD with one electron in the single-particle level at energy ε_0 and broadening Γ. The Kondo state emerge as a consequence of the spin-flip cotunneling processes in the density of states at the Fermi level.

phenomena. Control of the Kondo effect in magnetic field is especially appealing in CNT QDs, where only Zeeman term contributes. Moreover, studying the Kondo effect for higher spin states i.e. $S = 1$ is possible in CNT QDs because of their unique band structure (two degenerate orbital levels) [23, 87].

4.2.2 Observation of the Kondo effect

The condition for observing the Kondo effect is a good coupling of the QD to the leads ($\boldsymbol{T} \sim 0.5$) and $T_{exp} < T_K$. To satisfy the first condition we have used palladium for the metallization of the electrodes which are attached to the CNT. As we have mentioned before palladium makes excellent contacts to CNTs. The samples presented in this section have the contact separation of $L \approx 300\,\text{nm}$. High conductive ($G \approx 2e^2/h$), metallic SWNTs are chosen by the electrical characterization at the room temperature (Chapter 2). The low temperature measurements have been preformed in a ^3He system with a base temperature of $T \approx 300\,\text{mK}$ to fulfill the second condition.

In the non-linear regime the Kondo effect manifests itself as a high conductive peak around zero bias. When $T \ll T_K$, the FWHM of the Kondo resonance is roughly given by $2k_B T_K$ [95]. This is one way to extract T_K. The traces in bias for two measured Kondo ridges are shown in Fig. 4.9 (full lines), together with fits (dashed lines) with the extracted T_K values. The other signature of the Kondo effect is the logarithmic increase of G with decreasing temperature. In the Kondo regime, conductance G is expected to approach the unitary limit $G_0 = 2e^2/h$ for $T \to 0$. Approaching the unitary limit by decreasing the temperature, G should follow a universal scaling form, which can be approximated by an empirical form [97, 99],

$$G(T) = G_0/(1 + (2^{\frac{1}{s}} - 1)(T/T_K)^2)^s, \tag{4.6}$$

where $s = 0.22$ for spin $S = 1/2$ on the dot. The temperature dependence (open circles) for the same Kondo ridges as in Fig. 4.9a are shown in Fig. 4.9b. The solid curves are fits to Eq. 4.6, where G_0 and T_K are used as fitting parameters. This is yet another way to extract T_K. If we compare T_K extracted from the differential conductance and the temperature dependence the agreement is good. Unfortunately, the base temperature in our fridge (T=300 mK) is not low enough to observe a clear saturation of the conductance at the Kondo ridges. The obtained values for G_0 from the fit, ($G_0 \approx 1.57e^2/h$ for the first Kondo ridge and $G_0 \approx 1.65e^2/h$ for the second one) suggests an asymmetry of the contacts which will reduce the maximum conductance according to the resonant tunneling result $G_0 \propto \Gamma_r \Gamma_l/\Gamma$.
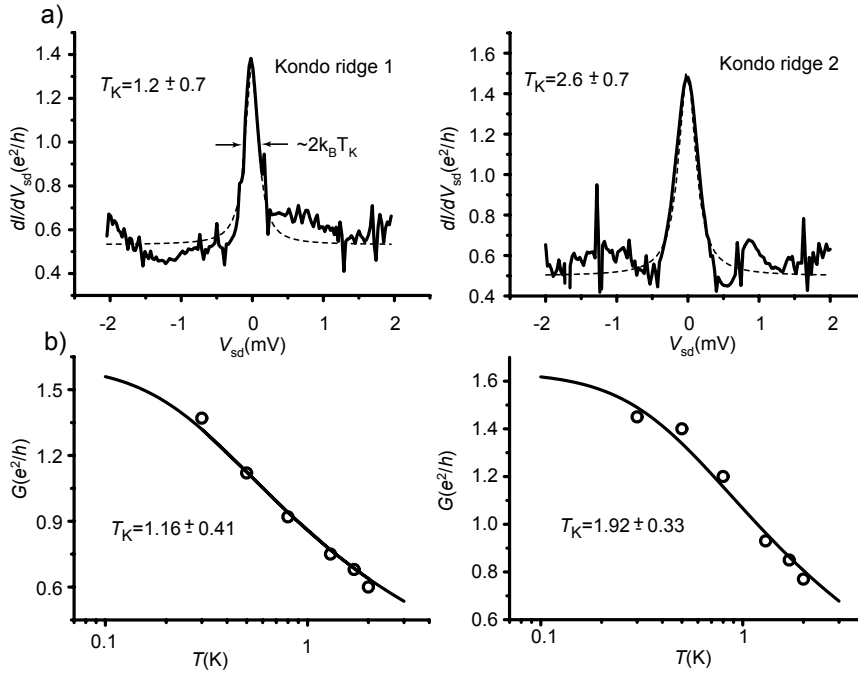
Figure 4.9: (a) dI/dV_{sd} versus V_{sd} for the two Kondo ridges taken at $T = 300\,\text{mK}$. The dashed lines are fits to the measured data. The width of the Kondo ridges is proportional to $2k_BT_K$. Extracted Kondo temperatures to corresponding curves are shown on the plots. (b) The temperature dependance of the maximum conductance for the Kondo ridges in (a). The solid curves are fits to Eq. 4.6. Corresponding Kondo temperatures are indicated.

Up to now, we have discussed the Kondo effect for $S=1/2$. As for the QD with $S=1/2$, the triplet state $S=1$ can also be screened by cotunneling processes. Since two orbital states should be degenerate in energy for a SWNT, expected degeneracy is the four-fold (including spin) and higher order spin state e.g. $S=1$ in principal can be formed for an even number of electrons. In the next section we report on the observation of the different shell filling in a metallic SWNT.

4.3   Shell pattern of a SWNT quantum dot

In this section, we will focus first on one set of measurements which we will analyze in great detail. This set of data is shown in Fig. 4.10. Fig. 4.10a shows the linear-response conductance G as a function of gate voltage V_g. Fig. 4.10b and c display the corresponding grey-scale plots of the differential conductance G_d in zero magnetic field and $B = 5\,\mathrm{T}$, respectively. White corresponds to low and black to high conductance.

The observed patterns correspond to a quantum dot with a relatively strong coupling to the contacts. Signatures of the latter are high conductance ridges, observed at zero bias ($V_{sd} \approx 0$) and $B = 0$, caused by the Kondo effect. This effect is a many-electron effect and requires a relatively high tunneling coupling to the leads in order to be appreciable at temperatures where the measurements take place. As required [82, 83], we find that G increases if the temperature is lowered below $\approx 4\,\mathrm{K}$ to saturate at the lowest temperature close to the unitary limit of $G = 2e^2/h$. The characteristic energy scale, i.e. the Kondo temperature T_K, has been deduced from the temperature dependence of G in ridge 3 (not shown) and found to be $T_K \approx 2\,\mathrm{K}$. The conductance enhancement due to the Kondo effect is observed at zero source-drain voltage if $B = 0$. In a magnetic field, however, the conductance enhancement is reduced and a splitting of the peak conductance to finite source-drain voltages is expected [82, 98]. This splitting is visible in Fig. 4.10c which was measured in a field of $5\,\mathrm{T}$. That the linear-response conductance G is suppressed in a magnetic field is clearly seen in Fig. 4.10a in which the solid (dashed) curve correspond to $B = 0$ ($B = 5\,\mathrm{T}$).

Because the many-electron effects (Kondo effect) are suppressed in magnetic field, we can use the linear-response conductance measurement in magnetic field (dashed curve in Fig. 4.10a) to assign the charge states of the quantum dot with reference to the single-electron tunneling picture. A transition from a ground state with N electrons in the dot to one with $N+1$ gives rise to a peak in the conductance, whereas G is suppressed in between. This pattern is nicely seen in the dashed curve of Fig. 4.10a, in which transitions have been labelled. Evidently, these conductance peaks form a repeating pattern in clusters of four. This pattern is the generic shell pattern of an ideal CNT quantum dot [86, 87]. It is caused by the four-fold degeneracy of 0D-eigenstates, two of which stem from spin and the other two from the so-called $K - K'$ orbital-degeneracy of graphene [35]. The four-fold pattern can be regarded as a measure of the quality of the SWNTs. It is not observed in all SWNTs and even if observed it is not usually present over the whole gate voltage range. But it can repeat over several shells, not just two as shown in Fig. 4.10. The degeneracy may be lifted by disorder and by
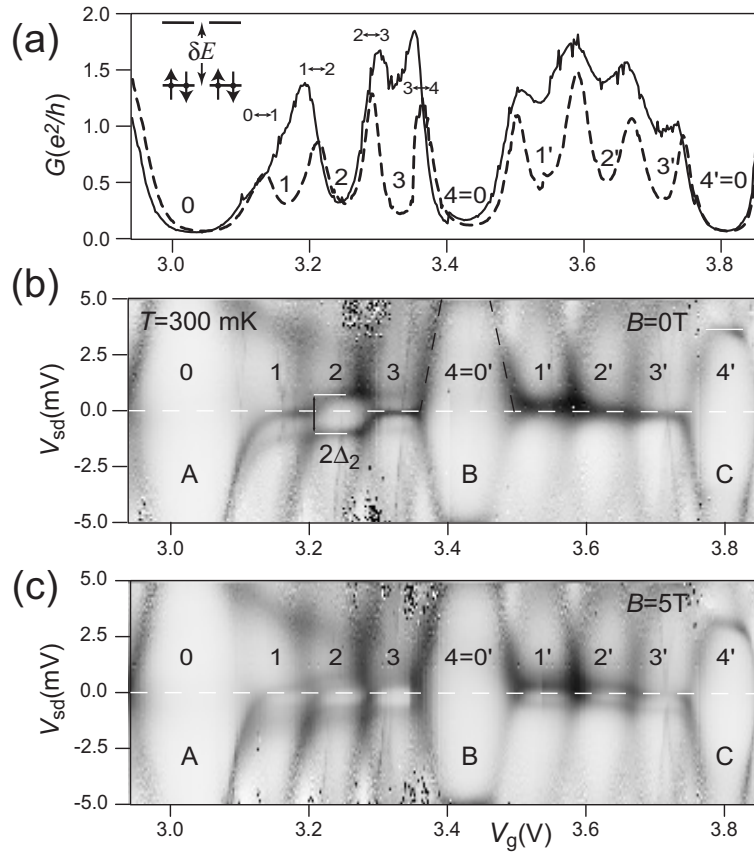
Figure 4.10: (a) Linear response conductance G as a function of back-gate voltage V_g of a SWNT device with contact separation $L \sim 300$ nm (edge-to-edge of reservoirs), measured at T=300 mK and in a magnetic field of $B = 0$ (solid curve) and $B = 5$ T (dashed curve). A clear clustering in four peaks is observed (pronounced in magnetic field), which suggests a single-electron shell pattern with four-fold degeneracy. Charge states corresponding to a filled shell (inset) are labelled as 0 or 4. (b,c) Corresponding grey-scale plots of the differential conductance dI/dV_{sd} (darker more conductive) at $B = 0$ (b) and $B = 5$ T (c) as a function of gate V_g and source-drain voltage V_{sd}. In the first shell, high conductance Kondo ridges (visible at $V_{sd} \sim 0$) are observed for charge states 1 and 3, whereas they appear for states $1'$, $2'$, and $3'$ in the second shell. The Kondo ridges clearly split in the applied magnetic field.

the contacts which may couple differently to the two orbital states. As has been pointed out be Oreg *et al.*, the four fold pattern may be absent even in a 'perfect' SWNT because the two orbital states can respond differently to the electrostatic gate-field if inhomogeneous [100].

Let us continue to analyze our data in terms of the constant-interaction model [90]. In order to assign the states only two parameters are needed: the single-electron charging energy $U_c = e^2/C$ and the single-electron level spacing δE. Note, that δE measures the energy difference between a filled shell to a state with one additional electron. This is sketched in the inset of Fig. 4.10a. To add an electron one has to provide an 'addition energy' composed of charging energy U_c plus level-spacing δE, the latter only if the electron must be added into a new shell. Since ΔE is proportional to the gate-voltage difference between adjacent conductance peaks, the labelling of states in terms of charge N in Fig. 4.10a should be understandable. $N = 0 \ mod \ 4$ corresponds to a ground state with a filled shell. Due to the large addition energy, the conductance is strongly suppressed for a filled shell, giving rise to the diamond-like white areas (denoted by A, B and C) in the grey-scale plots. Adding electrons to the filled shell one by one (peaks in G, dashed curve of Fig. 4.10a), we reach the state $N = 4$ which corresponds again to a filled shell.

In the following, the ground states will be labelled by $N = 0...3$ for the first quartet and $N = 0'...3'$ for the second, where $N = 4 = 0'$. Relying on the constant interaction model, the ratio between the average level spacing and charging energy amounts to $\delta E/U_c \approx 1$ in our data. It is seen, however, that U_c is constant to a good approximation, but that δE varies. For the respective diamonds A, B and C, the level spacing δE amounts to ≈ 7, 5, and 3 meV, respectively. Theoretically, the level-spacing of an ideal SWNT is given by $\delta E = h v_F/2L$, where $v_F = 8 \times 10^5$ m/s is the Fermi velocity and L the length of the tube that determines the 1D cavity [35]. Taking the nanotube length L measured from the edges of the contacts, which for this sample amounts to $L \sim 300$ nm, the equation predicts a level-spacing of $\delta E \sim 5.5$ meV in good agreement with the experimental values of $3 - 7$ meV. The data in Fig. 4.10 yields for the charging energy $U_c = 5.3 \pm 0.5$ meV and a gate-conversion factor of $\alpha := C_g/C$ of 0.08.

Focusing on the high-conductance Kondo ridges at zero bias voltage, we see in Fig. 4.10 a ridge at charge states $N = 1$ and $N = 3$, whereas G is suppressed at half-filling, i.e. at $N = 2$. The situation is different for the second quartet, where Kondo ridges are observed for all three states $N = 1$, 2 and 3. This phenomenon was reported before by Liang *et al.* [87]. Whereas a spin-1/2 Kondo effect is expected for $N = 1$ (one electron) and $N = 3$ (one hole), the situation at half-filling, i.e. at $N = 2$ is less obvious. The observed Kondo-effect was assigned to a spin-1 triplet state in

Ref. [87]. In the following we re-examine this assignment. To do so, we have to go beyond the 'free' electron model and consider among other things the exchange interaction. There are three additional parameters: First, it has been pointed out that the orbital degeneracy need not to be exact [86, 87]. The orbital mismatch is denoted by δ. With regard to on-site charging energy the doubly occupancy of one orbital is a bit higher in energy as compared to placing each of the two electrons in a separate orbital. This parameters has been introduced by Oreg *et al.* [100] and is denoted by δU. Finally, placing the two electrons in different orbitals gives rise to a spin-dependent exchange energy term, which according to Hund's rule favors the triplet state, i.e. the state with spin $S = 1$. This parameter is denoted by J. These parameters have been extracted, both for MWNTs [86] and SWNTs [87] and the analysis of our data confirm the previously obtained values. The importance of the parameters in descending order is δ, J and δU as the least important one. The former work by Buitelaar *et al.* reports $\delta \approx 0.2$ and $J < 0.09$ and the latter work by Liang *et al.* reports $\delta \approx 0.3$, $J \approx 0.1$ and $\delta U < 0.1$ (all numbers are measured in units of level spacing δE). We neglect δU because it is small and typically much smaller than the bare level broadening Γ, which - as we will emphasize - matters as well. Since the Kondo effect is the dynamic screening of the local spin by exchange with a sea of electrons, it is tempting to assign the Kondo ridge for $N = 2$ to a spin-1 (triplet) ground state. However, with regard to the just mentioned parameters, this appears to be unlikely, because $J < \delta$, favoring a spin-0 ground state [100].

Let us first contrast the possible states at $N = 1$ and $N = 2$ for the case of degenerate orbitals ($\delta = 0$) and without exchange ($J = 0$), shown in Fig. 4.11a, with the case of a finite level mismatch and a finite exchange energy, shown in Fig. 4.11b. In the first (maybe too naive) model of Fig. 4.11a, the degeneracy equals 4 at $N = 1$ and clearly Kondo physics can emerge. At $N = 2$ the degeneracy is even larger, amounting to 6 and second-order elastic spin-flip processes are energetically allowed so that Kondo physics can emerge as well. Here, two states are paired-electron states and the other four may be labelled as one singlet state with spin $S = 0$ and three triplet states with $S = 1$, denoted as S and T states. The Kondo effect may be expected to be even enhanced in this case due to the larger number of states [101]. This scenario corresponds to the Kondo effect for which the singlet and triplet states are degenerate. This has been realized experimentally in semiconducting quantum dots by tuning the states with either magnetic or electric fields [101, 102, 103]. Once we go over to the more realistic model shown in Fig. 4.11b, assuming that exchange and level mismatch are non-zero and of comparable magnitude, the $N = 1$ states remains 'normal' in the sense that only the lowest lying orbital need to be considered.

At half-filling, i.e. at $N = 2$, there are however two possibilities [100]: if exchange dominates ($J > \delta$), the ground state is the spin triplet (T) state, whereas if the opposite holds, the ground state is a paired electron (PE) residing on the lowest orbital state. The energy difference between the T and PE states is given by $\Delta = \delta - J$ [104]. Although the Kondo effect is (in principle) possible for the triplet, there is no Kondo effect possible for paired electrons. Note, that unlike previous discussions, there are *three* cases to consider at half-filling. Two may give rise to Kondo and one does not. To have an abbreviation at hand we denote the three $N = 2$ states with ST (degenerate ground state), PE (paired electron ground state) and T (triplet ground state). As mentioned above, the Kondo ridge at $N = 2$ has been assigned to the triplet state [87]. Though this is tempting at first sight, there is no necessity. In fact, this assignment is unlikely, first because J is measured to be small (usually smaller than δ) and secondly, the Kondo temperature T_K for triplet Kondo is predicted to be much smaller than T_K for $S = 1/2$-Kondo [105] (an estimate will follow below).
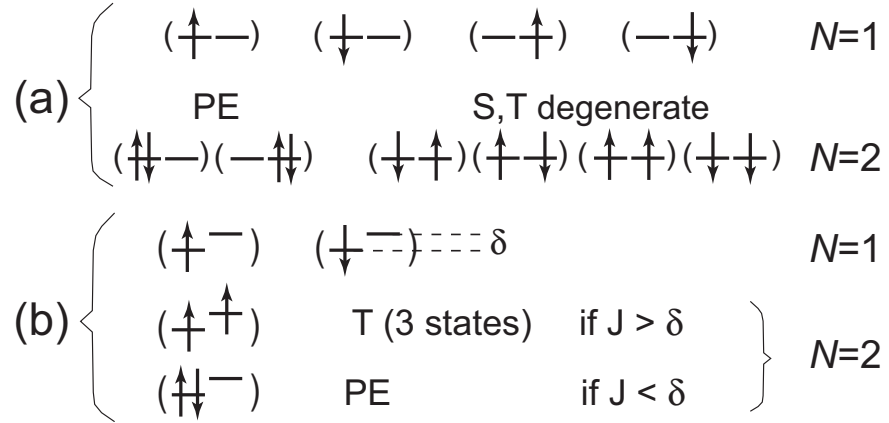
Figure 4.11: Illustration of the state-filling scheme for one ($N = 1$) and two ($N = 2$) excess electrons. In (a) the level-mismatch δ and the exchange energy J are zero, whereas these parameters are non-zero in (b). PE denotes a paired-electron state, S (T) the singlet (triplet) two electron state. The Kondo-effect may arise in three cases: obviously for the spin-1/2 with one excess electron ($N = 1$) and if $N = 2$ for the spin-1 triplet state, but also for the case for which $\delta = J = 0$, i.e. when the singlet and triplet states are degenerate (ST state).

We now look at the excitation spectra for $N = 1, 3$ and $N = 2$ in zero field. This is shown in Fig. 4.12(a-c), where (a) and (b) correspond

to odd filling ($N = 1, 3$) and (b) to half-filling ($N = 2$). The energy Δ of the first excited state at fixed N relative to the ground state is given by the level mismatch δ, both for $N = 1$ and $N = 3$, i.e. $\Delta_{1,3} = \delta$. This is illustrated in the respective insets on the right. The first excited states show up as a conductance peak at finite V_{sd}, corresponding to the excitation energy. This is a so-called inelastic co-tunneling process. We obtain from the measurement $\Delta_1 = 0.92\,\text{meV}$ and $\Delta_3 = 0.85\,\text{meV}$. Hence, the level mismatch is given by $0.89 \pm 0.4\,\text{meV}$. For the $N = 2$ case we have to distinguish two possibilities: if $J > \delta$, the ground state is the triplet (T) and the excited state the paired electron (PE) state, yielding $\Delta_2 = J - \delta$. If on the other hand $J < \delta$, the states are reversed, yielding $\Delta_2 = \delta - J$. In general, $\Delta_2 = |\delta - J|$. From the experiment (Fig. 4.12c) we deduce $\Delta_2 = 0.88\,\text{meV}$. We stress that we measure on one and the same shell so that we can use the parameter δ, measured for the $N = 1, 3$ case, also for the $N = 2$ case. Comparing the numbers, leaves open two possibilities: either the exchange parameter is quite small, i.e. $J \sim 0$ (taking the possible errors into account $J \lesssim 0.1\,\text{meV}$), or it is quite large $J \gtrsim 1.65\,\text{meV}$. If the latter would be true, it would be a remarkable coincidence that we find $|\delta - J| \sim \delta$ with $J \approx 2\delta$. Moreover, the ratio $J/\delta E > 0.3$ would be quite remarkable with regard to previous measurements. On the other hand, comparable values for J have theoretically been predicted, however only for small diameter tubes. For example, $J/\delta E$ was estimated to be ≥ 0.22 and ≥ 0.44 for a $(10, 10)$ and $(5, 5)$ tube, respectively [100]. However, the diameter d of CVD-grown NTs is known to vary substantial and in particular we find that $d \gtrsim 2\,\text{nm}$ (chapter 2.), from which one would theoretically predict an exchange parameter of order $J/\delta E \sim 0.1$, which disagrees with the finding above. If J were indeed as large as 2δ, and therefore $J > \delta$, the triplet state would be the ground state at half-filling, i.e. at $N = 2$ and $N = 2'$. The Kondo effect at half-filling must then be assigned to the $S = 1$ Kondo effect. To explain the absence of the Kondo effect for $N = 2$ and its presence for $N = 2'$, one would have to argue that the Kondo temperature is smaller than $300\,\text{mK}$ at $N = 2$, whereas it is larger at $N = 2'$. Pustilnik *et al.* [106] showed that the Kondo temperature $T_K^{S=1}$ for the triplet state is smaller than $T_{K,1/2}$ for the spin-1/2 case. More precisely, $T_{K,1}$ can be estimated according to $k_B T_{K,1} = \left(k_B T_{K,1/2}\right)^2 / \delta E$. The average width of the zero-bias resonances at $N = 1, 3$ in the left quartet is measured to be $0.35\,\text{meV}$, yielding as a prediction $T_{K,1} \approx 0.25\,\text{K}$. In the right quartet the same procedure yields for $N = 1', 3'$ a mean width of $0.8\,\text{meV}$, from which one predicts $T_{K,1} \approx 1.5\,\text{K}$. Hence, the comparison with the measuring temperature does not exclude $S = 1$ Kondo, as $T_{K,1} \lesssim 0.3\,\text{K}$ in the left quartet and $T_{K,1} > 0.3\,\text{K}$ in the right one. However, the ratio $T_{K,1}/T_{K,1/2}$

measured in the right quartet is inconsistent with theory which predicts $T_{K,1/2}/\delta E$. The former is evaluated to $0.8\ldots 1.6$, whereas the latter is at most 0.3. In simple terms, the appearance of the two resonances at $N = 1'$ and $N = 2'$ with essentially one and the same width (1.1 and 0.9 meV, respectively), makes triplet-Kondo quite unlikely.

In magnetic field the states further split due to the Zeeman energy given by $\pm g\mu_B B/2$, where μ_B is the Bohr magneton and g the so-called g-factor. g has been measured in related electrical measurements on carbon nanotube quantum dots and found to agree with the free electron value of $g = 2$ [86, 47, 107]. Due to the Zeeman-splitting the excitation spectrum changes. At $N = 1$ and for small magnetic fields (with regard to the level mismatch), the spin-1/2 Kondo resonance is expected to split [86], evolving into inelastic co-tunneling with an excitation energy given by $\Delta_Z = g\mu_B B$. Because of the relatively large width of the zero-bias resonances, this shift is hardly visible for small magnetic fields in the experiment. That is why we have chosen a relatively large field of 5 T. This field yields for the Zemann excitation energy 0.58 meV, taking $g = 2$. Note, however, that there is a second excited state given by the level mismatch $\delta \approx 0.9$ meV. If we analyze the non-linear differential conductance as a function of V_{sd}, we see two excitation lines (one at positive and one at negative bias), which are markedly broadened, suggesting an overlap of two excitation features, see Fig. 4.12a (grey overlaid graph). The onset of the excitation peaks agrees with the Zeeman energy (arrows from below). This analysis is of particular importance in the $N = 2$ case, because it allows us to distinguish the PE from the T ground state unambiguously, see Fig. 4.13. If the ground state is the paired-electron state, the first excitation occurs at energy $\Delta_2 = \delta - \Delta_Z - J \approx \delta - \Delta_Z$ (because $J \approx 0$) and the second lies at δ. In contrast, if the ground state is the spin-1 triplet state the first two excited states have energy $\Delta = J + \Delta_Z - \delta \approx \delta + \Delta_Z$ and $J + \Delta_Z \approx 2\delta + \Delta_Z$ (because $J \approx 2\delta$ in this case). This is shown (approximately to scale) in the illustrations of Fig. 4.13b and c, respectively. Based on the field-dependence of the excitation spectrum we can predict the position of the excitation peaks for the two cases. In the measurement, shown in Fig. 4.13a, the upper black arrows point to expected excitations if the ground state is the paired-electron (PE) state, whereas the upwards pointing open arrows correspond to the expected excitations for the triplet (T) ground state. It is obvious that the agreement with the PE state is much better. The excitation peaks at zero field do not move out to larger energies expected for the T ground state, but rather shrink. In particular there are clear low-energy shoulders visible which agree quite reasonably with the expected lowest energy excitation energy for the PE ground state.

Taking all arguments together, this makes a convincing case for the ground state at half-filling, i.e. for $N = 2$, which is the paired-electron
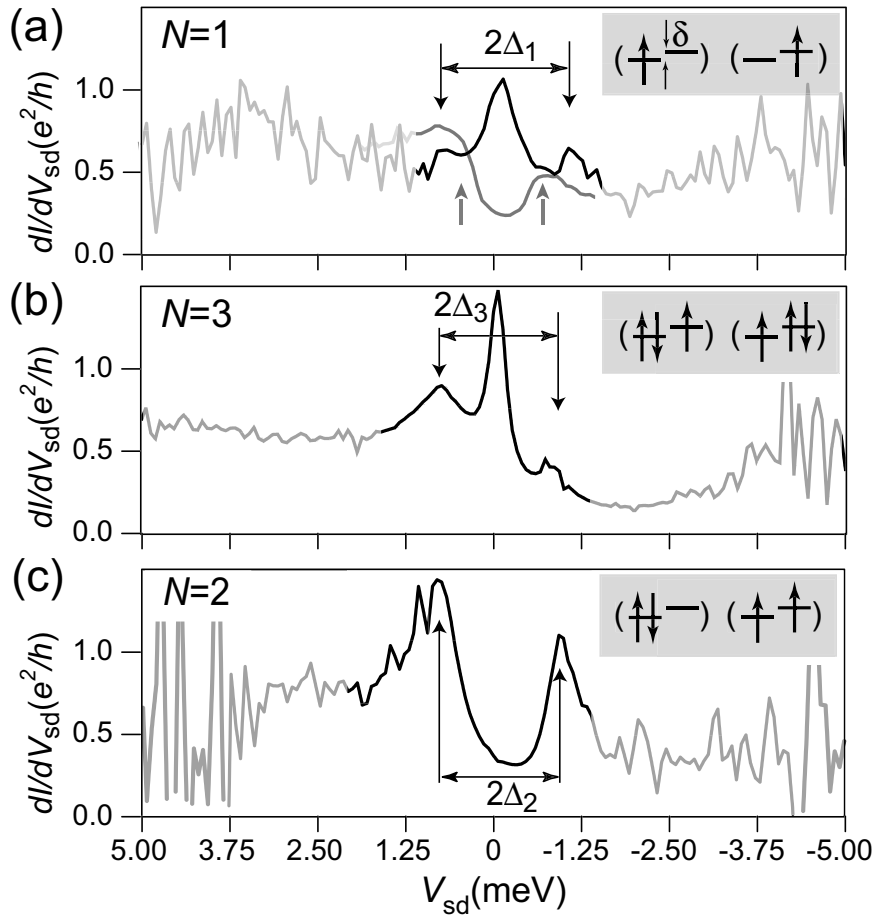
Figure 4.12: Non-linear differential conductance dI/dV_{sd} as a function of V_{sd} at $V_g = const$ deduced from the data shown in Fig. 1b at zero magnetic field. (a) and (b) correspond to the states $N = 1$ and $N = 3$, whereas (c) correspond to the half-filled shell $N = 2$. All three dI/dV_{sd} cuts have been placed in the middle of the charge state. The visible excitation peaks occur at energy Δ and are due to inelastic co-tunneling through the excited state. The relevant states are illustrated in the respective insets on the right. The grey curve in (a) has been measured in a magnetic field of 5 T. Arrows point to $\Delta_Z = g\mu_B B = 0.58$ meV using $g = 2$.

state. Moreover, the exchange energy must be very small. How do we then have to explain the pronounced Kondo ridge at $N = 2'$, visible in Fig. 4.10b
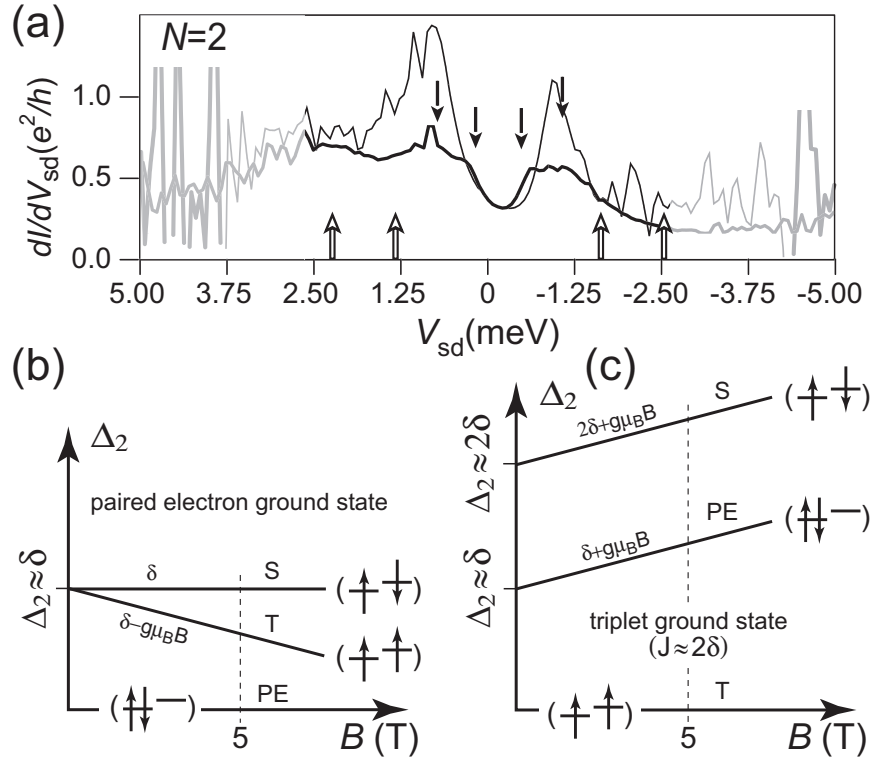
Figure 4.13: (a) Non-linear differential conductance dI/dV_{sd} as a function of V_{sd} taken from the data shown in Fig. 4.10b at a fixed gate-voltage corresponding to $N = 2$. The thick (thin) curve was measured in a magnetic field of $B = 5\,\mathrm{T}$ ($B = 0\,\mathrm{T}$). (b) and (c) illustrate the magnetic-field dependence of the first two excited states at $N = 2$. The two cases are drawn approximately to scale using the fact that J is either ≈ 0 (PE ground state) or $\approx 2\delta$ (T ground state) deduced from the data of Fig. 4.10 and Fig. 4.11.

? As we have pointed out when discussing Fig. 4.10, there are two cases at half-filling that allow for Kondo: spin-1 Kondo in case of the triplet state or the degenerate ground state, i.e. the ST-state. Based on our previous discussion the former can be excluded, so that the only remaining possibility requires degenerate orbitals. We know that the orbitals are not exactly degenerate. The level mismatch, as deduced from the $N = 1 - 3$ states amounts to $\delta \approx 0.9\,\mathrm{meV}$, which is quite appreciable. Due to the relative large width of the zero-bias conductance peaks at $N = 1' \ldots 3'$ we are not

able to deduce the level mismatch on the second shell along the same lines as before for the first shell. Though it is possible that δ is smaller in the second shell, it is unlikely zero. We emphasize, however, that it is crucial to compare the level mismatch with the level width, due to the tunneling couplings Γ_s and Γ_d to the respective contacts. If $\delta < \Gamma$, where $\Gamma := \Gamma_s + \Gamma_d$, the two orbital states cannot be distinguished and are in effect degenerate. We know from other measurements on carbon nanotubes (and will show a dramatic example latter on) that Γ may vary a lot with gate voltage. Our picture of the half-filled state is correct, if we can show that Γ is smaller than δ within the first shell, but larger within the second. There are several ways to deduce Γ. One possibility is to deduce it from the width of the excitation features at fixed N, another one is to analyze the transitions at finite bias at the edge of the Coulomb-blockade (CB) diamonds. For the left shell the excitation spectra for states $N = 2$ and $N = 3$ (see Fig. 4.12) yield $\Gamma \approx 0.7\,\text{meV}$, whereas a cut at $V_g = 3.1\,\text{V}$, corresponding to the transition $0 \leftrightarrow 1$, yields $\Gamma \approx 0.9\,\text{meV}$. Because we cannot resolve excitation features in the right shell, we have to rely on transitions at the edge of CB-diamonds. We deduce $\Gamma \approx 3\,\text{meV}$ at $0' \leftrightarrow 1'$ and $\Gamma \approx 1.9\,\text{meV}$ at $3' \leftrightarrow 4'$. Clearly $\Gamma \lesssim \delta$ for the left shell and $\Gamma > \delta$ for the right one in support of our statement. To conclude this part, we can say that the Kondo effect at $N = 2'$ is not a triplet Kondo, but arises because Γ is larger than the level mismatch, resulting in a ground state in which the paired-electron, the singlet and triplet states are effectively degenerate. Our data is only consistent with a very small exchange exchange term of $J/\delta E \lesssim 0.02$. Such a small value can only be reconciled with theory [100] if either the tube has a large diameter of order $\lesssim 10\,\text{nm}$ or the interaction is locally screened, possibly by the presence of other nanotubes forming a bundle.

Examination of the measured data shows that for the Kondo resonances labelled with $1'$ and $3'$ in Fig. 4.10b, the positions of the maximum conductance are situated at non-zero bias. This is shown in Fig. 4.14. This phenomenon has been observed in semiconducting quantum dots and was termed the anomalous Kondo effect by Simmel *et al.* [108]. It was suggested by these authors that the effect is due to asymmetric and energy-dependent coupling strengths Γ_s and Γ_d to the two reservoirs. The effect has thereafter been confirmed theoretically in a single-impurity Anderson model [109]. The authors show that the peak conductance is shifted provided that $\Gamma_s \neq \Gamma_d$, but an energy dependence of $\Gamma_{s,d}$ is not required. We stress here, however, that the Anderson model introduces an additional model-dependent asymmetry in condition that $U \to \infty$, which is not realized in a real quantum dot. At half-filling, there is particle-hole symmetry where electrons (holes) can be exchanged via both the bare state at energy ϵ_0 and the one at $\epsilon_0 + U$. In this case, no shift of the Kondo peak is expected even if
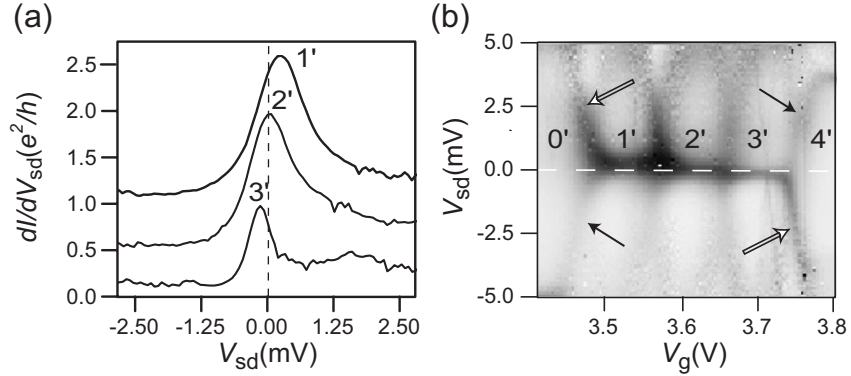
Figure 4.14: The Kondo resonance is observed to be offset with respect to the bias voltage V_{sd} for the mixed-valence state with filling 1/4 ($N = 1'$) and 3/4 ($N = 3'$), whereas it is centered at $V_{sd} = 0$ at half-filling. (a) shows the respective differential conductance at constant gate voltage corresponding to part (b), which reproduces the second shell of Fig. 4.10b. Arrows emphasize an additional asymmetry, discussed in the text.

$\Gamma_s \neq \Gamma_d$. Extrapolating $G(T)$ to the unitary limit $G(0)$ at zero temperature (not shown) using the standard expression to fit the Kondo effect, i.e. $G(T) = G(0)/\left[1 + (2^{1/s} - 1)(T/T_K)^2\right]^2$ [110], we obtain for the ridge at charge state $N = 3$ a zero temperature conductance of $G(0) = 1.68\,e^2/h$, out of which the Γ ratio is estimated to be ≈ 2. Hence, there is an asymmetry of magnitude comparable to Ref. [108]. Our statement, that the shift of the Kondo peak to finite bias is absent at half-filling is beautifully reflected in the data of Fig. 4.14. Due to the four-fold symmetry, half-filling corresponds to charge state $N = 2'$ and indeed, this peak has its maximum at $V_{sd} = 0$. The other two resonances are shifted oppositely, one to $V_{sd} > 0$ ($N = 1'$) and the other to $V_{sd} < 0$ ($N = 3'$). The shift amounts to $0.22\,\text{meV}$. These shifts are comparable in magnitude to the ones seen by Schimmel *et al.*, although they have observed only unipolar shifts. Finally we remark that the transitions to the Coulomb-blockade diamonds, i.e. $2' \leftrightarrow 1'$ and $3' \leftrightarrow 4'$ are asymmetric with respect to the V_{sd}, see arrows. Cross-sections at constant gate-voltage through these transitions allow to deduce the respective Γ's and their ratio: $\gamma := \Gamma_s/\Gamma_d$. We point out, that this asymmetry is a consequence of the level degeneracy. Consider tunneling at finite bias into the $N = 1'$ state. Because there is a four-fold degeneracy the effective in-tunneling rate is enhanced by a factor of 4. In contrast, this phase-space

argument does not hold for the out-tunneling rate. The respective current steps are then given by $(4e/h)\Gamma_s\Gamma_d/(\Gamma_s + 4\Gamma_d)$ for one bias polarity (e.g. $V_{sd} > 0$) and $(4e/h)\Gamma_s\Gamma_d/(4\Gamma_s + \Gamma_d)$ for the other polarity, where the factor 4 counts the degeneracy. It is clear from these two relations that the current steps are only different for the two polarities if $\gamma \neq 1$. The two current steps, measured for the transition $3' \leftrightarrow 4'$, amount to ≈ 20 and $\approx 30\,\text{nA}$, yielding for the Γ-ratio $\gamma \sim 2$ (in agreement to what we have deduced before in a different way) and $\Gamma_s \approx 1.4\,\text{meV}$ and $\Gamma_d \approx 0.7\,\text{meV}$, so that the total level broadening is approximately $\Gamma \approx 2\,\text{meV}$. Also the latter value is in agreement with the previously mentioned width of the transition, which we measured to be $\Gamma \approx 1.9\,\text{meV}$.

4.3.1 Two-fold degeneracy

The observation of four-fold degeneracy reflects the band structure of an ideal SWNT. We have just shown that the orbital degeneracy in a SWNT is not complete i.e. the orbital mismatch (δ) is finite. This is not surprising, since the hybridization with the contacts or scatterers inside a nanotube can lower the symmetry of the system [86, 87]. Furthermore, because of poor control during the fabrication at nanometer scale it is expected that δ vary randomly in different CNT devices. In the case of large δ the band degeneracy can be completely lifted, where the single-electron levels repel each other ($\delta E \sim U_c$). However, the spin degeneracy is expected to be still preserved. This is known as the two-fold degeneracy.

Schematics of the shell filling in a QD with two-fold degenerate levels is illustrated in Fig. 4.15a. In the CB regime, the two-fold degeneracy reflects in a grey-scale plot, as an alternating sequence of small and large Coulomb blockade diamonds. Starting from an even filling number, $\Delta E = U_c + \delta E$ for the first added electron (large CB diamond) and U_c for the second one (small CB diamond). This is represented in Fig. 4.15b for the sample with the contact (Ti/Au) separation of $\sim 1\,\mu\text{m}$. Note that from the difference between large and small diamonds, the energy level spacing can be directly deduced, $\delta E \approx 2\,\text{meV}$. The size of the small diamonds reflects the charging energy $U_c \approx 2.5\,\text{meV}$. In addition, the observation of the excited states, imply coherent transport through a single resonant level.

Since, the two-fold degeneracy reflects the fundamental property of the single orbital state in a QD (Pauli principal) it is expected to be readily observed. Surprisingly, deviations exist also in this case. The set of CB-peaks is shown in Fig. 4.16a. The spacing of CB-peaks versus gate voltage position is shown in Fig. 4.16b. A change in a period of the CB-peaks directly reflects the energy level spacing. For this gate voltage region, the two-fold degeneracy is present to some extent. However, for $V_g > -0.3V$,
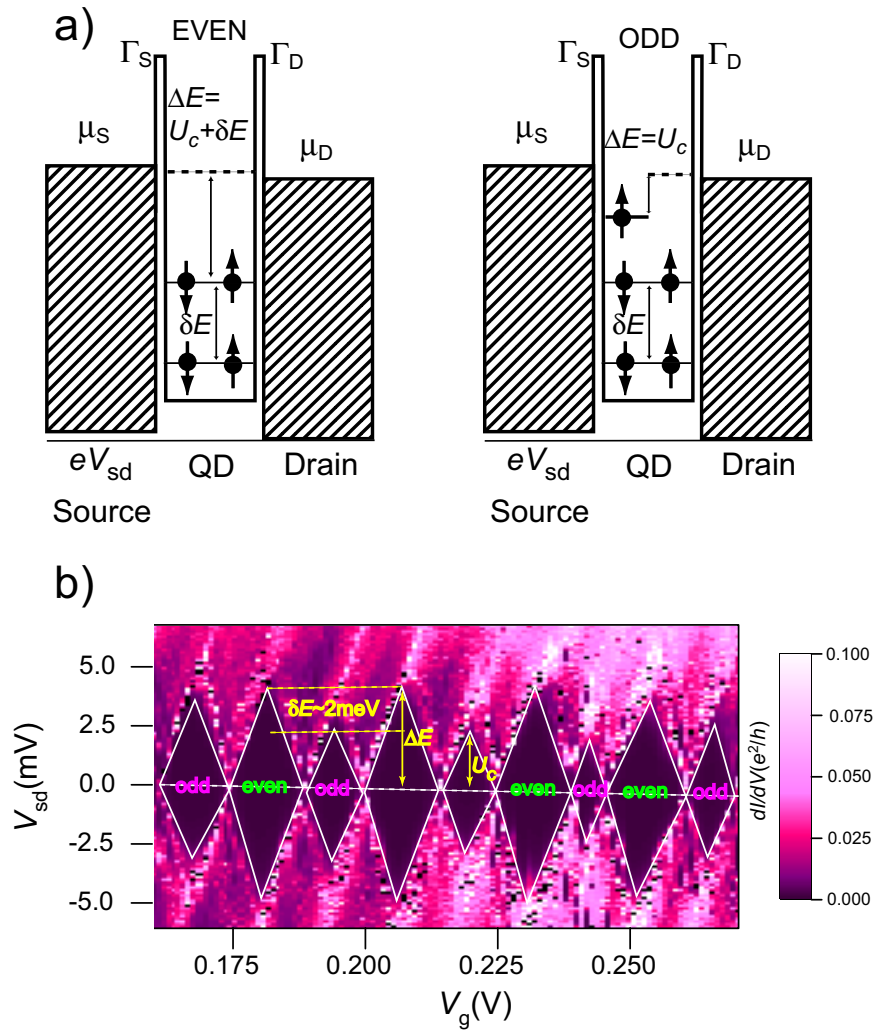
Figure 4.15: (a) A schematic illustration of the shell filling for an odd and an even number of electrons on a QD. (b) A grey-scale plot for a metallic SWNT contacted with Ti/Au bilayer, $L \approx 1\,\mu\text{m}$ taken at $T = 300\,\text{mK}$. The alternation in a size of the Coulomb blockade diamonds is assigned to spin degeneracy of the single electron level. In this case, the spin ground state on the QD has a sequence $S = 1/2 \rightarrow 0 \rightarrow 1/2 \rightarrow 0$.

the addition energy does not follow the expected alternating pattern for two degenerate states. We emphasize that this is just a typical example and our other measurements show similar or even more random behavior. At this moment, the origin of this deviations are not fully understood. We believe that most probably the presence of disorder in/on CNT induce the potential which perturbed electron states in the QD, leading to the absence of the expected two-fold degeneracy. Moreover, a non-uniform gate potential profile can rise various spin flip processes, where the intuitive scheme of the shell filling can be altered [47, 100].
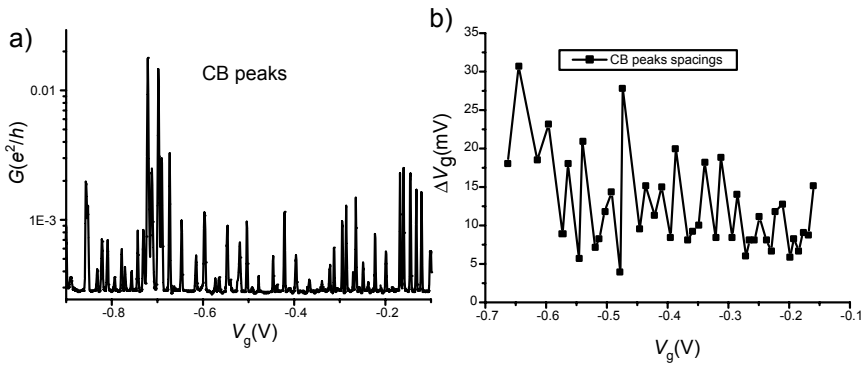
Figure 4.16: (a) Conductance G versus gate voltage V_g in the linear response regime, for a SWNT QD. (b) The spacing between CB peaks versus the same gate region as in (a). To some extent the two-fold degeneracy can be observed from the alternation of the CB-peaks spacing. However, a random change in the spacing for $V_g > -0.3$ most likely originate from the imperfection of the device.

4.3.2 Deviations from the expected shell filling

In the last part of this section, we will point to further deviations which can not be accounted for within the simple shall filling pattern. Fig. 4.17 displays the dependance of the linear-response (a) and differential conductance (b) of another sample contacted with Pd. The contact separation amounts to $L \sim 0.8\,\mu$m. The linear-response conductance is bound by $2e^2/h$ suggesting that we measure individual SWNT. Four-fold clustering in the electron addition spectrum is observed for more then five shells $(A-E)$, corresponding to 20 electrons. Due to the three times larger length of this device as compared to the one in Fig. 4.10 the energy scale is reduced by approximately a factor of three. The level-spacing amounts to $\delta E \approx 1 - 1.5\,\text{meV}$

and the charging energy to $U_c \approx 1\,\mathrm{meV}$. As with the data of Fig. 4.10 the Kondo effect may appear at half-filling (α) or may be absent (β), which according to the previous discussion would correspond to the PE and S ground state, respectively. There are differences, however. The most dramatic one occurs in shell D for the three electron state (filling 3/4), marked with O. Instead of the expected spin-1/2 Kondo, the conductance is actually suppressed. This is seen as a pronounced white bubble. Because the Kondo effect is present for the one electron state (filling 1/4), this implies breaking of particle-hole symmetry. This effect is quite surprising and has not been reported before. We do not have a convincing explanation but mention one possibility. The three electrons at $N = 3$ may like to form a high-spin state with total spin $S = 3/2$. However, this requires three different orbitals, but there are only two in an ideal tube. It may be that the nanotube is not perfect, rather a bundle or a multi-shell tube, which may provide additional orbitals. We think that this scenario is unlikely, because we have previously shown that the exchange in CNTs is small, and it is particularly small if the interaction is screened by other tubes. It may be caused by a magnetic defect due to residual catalyst particles, which may enhance the exchange energy.

Similar gap-features are sometimes seen over the entire grey-scale plot. We show in Fig. 4.18 a short section taken out of an extensive differential conductance grey-scale plot of another sample. The contacting material is Au in this case and the contact separation amounts to $L \sim 1\,\mu\mathrm{m}$. The contact transparencies are lower here and typical two terminal conductances are of order $0.1\,e^2/h$. Consequently, the main features in the differential-conductance are Coulomb blockade (CB) diamonds. The generic four-fold shell structure is not apparent. It is masked by the charging energy which dominates here. The observed addition energy amounts to $\Delta E \approx 5\,\mathrm{meV}$. We stress that the dI/dV_{sd} measurements of Fig. 4.18a extend over more than 17 electrons without any noticeably change. The linear-response conductance (Fig. 4.18c) shows a very regular set of high conductance peaks at the transition between neighboring charge states with peak values approaching $0.8\,e^2/h$. The spacing between these CB-oscillation peaks is surprisingly constant, amounting to $\Delta V_g = 73 \pm 5\,\mathrm{mV}$.

We present this measurement here, because of the presence of a striking gap-structure, which is seen inside of *all* CB diamonds and which might be related to the gap which we have mentioned before, i.e. the feature labelled O in Fig. 4.17b. Two dI/dV_{sd} cross-sections at constant V_g are presented in Fig. 4.18b. We find that the size of the gap Δ_g varies a bit in different charge state and is estimated to be $\Delta_g \approx 0.7\,\mathrm{meV}$ ($0.3\ldots0.9\,\mathrm{meV}$). Additional suppression may be caused, if the nanotube is split by a strong scattering center into two segments in series. In this case, however, a regu-
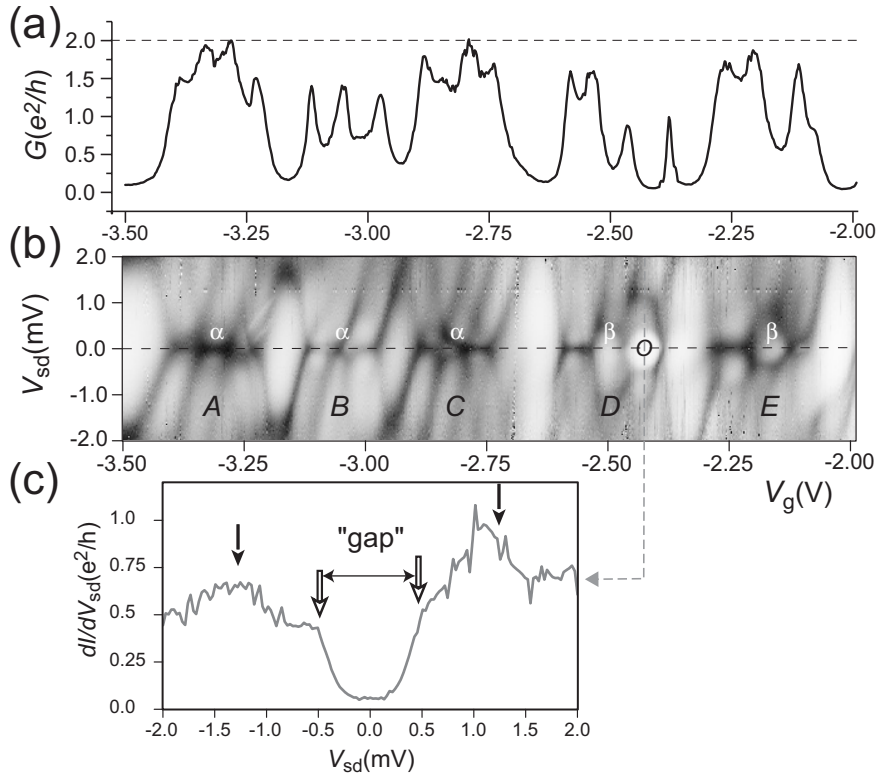
Figure 4.17: (a) Linear response conductance plotted as a function of the gate voltage V_g and (b) differential conductance dI/dV_{sd} (darker more conductive) plotted as a function of V_g and V_{sd} for an another SWNT device with length $L \sim 800$ nm contacted by palladium. The shell pattern of four electrons each extends over 5 shells ($A - E$). The Kondo effect occurring at half-filling is marked with α, while β corresponds to the singlet ground state. O points to an anomaly, a strong gap-feature arising for a three electron state. The non-linear dI/dV_{sd} through the middle of this state is shown in (c).

lar periodic CB-oscillation pattern is not expected, because single-electron transport requires that two charge states are degenerate in both segments simultaneously. While this maybe possible occasionally, it would be surprising if the levels would move in both segments with gate voltage exactly equally. We therefore are convinced, that this scenario is wrong. Also a possible parallel conductance through two (or more) different tubes can
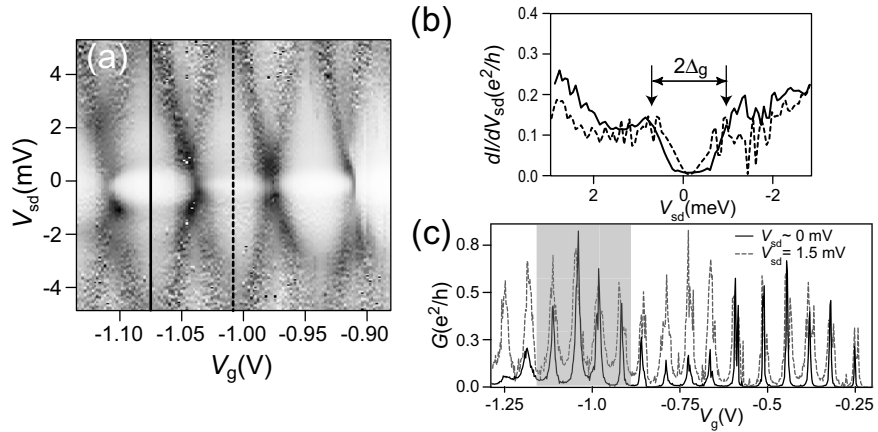
Figure 4.18: (a) Differential-conductance plot of a SWNT device with contact separation $L \sim 1\,\mu$m at T=300 mK (maximum conductance $= e^2/h$, black). Coulomb blockade diamonds are clearly seen. In addition gaps appear near zero bias. (b) dI/dV_{sd} as a function of V_{sd} and at constant V_g along the corresponding lines, shown in (a). Conductance plotted as a function of the gate voltage. The full line represent measurement taken at $V_{sd} = 0$ while dashed line at $V_{sd} = 1.5$ mV. The shaded region correspond to (a).

be excluded, because this should appear in the grey-scale-plot as a bare superposition of two CB-patterns. Moreover, the observed grey-scale plot cannot be modelled as a regular CB-pattern multiplied by a gap-feature in the vicinity of $V_{sd} \approx 0$. This is evident from the Fig. 4.18c which shows $G(V_g)$ at $V_{sd} = 0$ (full curve) and at $V_{sd} = 1.5$ mV (dashed curve). In the shaded region, corresponding to Fig. 4.18a, the suppression is only active in between the CB-oscillation peaks, whereas the peaks themselves are not suppressed, suggesting that the 0D orbitals extend from source to drain. The low-conductance 'bubbles' are therefore confined to the CB-region of the nanotube and this new effect is observable in transport through a single carbon nanotube. This does not mean that there is only one single-walled carbon nanotube present. The device may still consist of a small bundle or a multishell tube, of which only one tube is effectively coupled to the reservoirs. In addition, the presence of magnetic impurities in the form of catalyst particles cannot be excluded, so that the observed gaps may originate from magnetic interactions with these particles. The Kondo effect which results in a high conductance resonance can be described as an anti-ferromagnetic exchange between the leads and the quantum dot. It is tempting to sug-

gest that the opposite scenario, namely ferromagnetic exchange with, for example, a magnetic particle, may suppress the conductance [99]

4.4 The Fano effect

In this section we analyze the high-G regime, where the transition from a quantum dot to a weak link appear on the same CNT upon varying V_g. Nonetheless, sharp resonances appear superimposed on the background which varies slowly with gate voltage. The resonances are identified by their lineshape as Fano resonances. We think that the interfering channel, leading to these Fano resonances, have to be found in other tubes (within a single bundle), which are weakly coupled to the reservoirs.

4.4.1 Introduction

The Fano resonance (FR) is a universal physical phenomenon which has historically been discovered as asymmetric line profiles in spectra of rare gases [111]. This effect has successfully been interpreted by U. Fano in terms of the interference between an auto-ionized state and the continuum [112]. FRs have for example been observed in the spectroscopy of atoms and molecules [111], in electron, neutron and in Raman scattering [113, 114, 115].

Generally speaking, the interference of a resonant state (the resonant channel) with a continuum (the non-resonant channel) gives rise to Fano line shapes. An illustration is shown in Fig. 4.19a. This phenomenon can also naturally arise in coherent electrical transport through nanostructures. Indeed, Madhavan *et al.* [116] observed Fano line shapes in the differential electrical conductance dI/dV vs. V, while tunneling with a scanning tunneling microscope through an impurity atom on a metal surface. The first observation of FRs in mesoscopic devices has been reported by Göres *et al.* in a single-electron transistor fabricated into a gated two-dimensional electron gas [89]. Recently, several groups reported the observation of FRs in multi-wall carbon nanotubes (MWNTs). Kim *et al.* [117] observed the FR on crossed MWNTs, while Yi *et al.* [118] reported on FRs measured in MWNT bundles. Furthermore, Fano resonances have been measured on an individual MWNT [119]. However, similar observations have not yet been reported for SWNTs.

Following the notion of U. Fano [112], the energy-dependent conductance $G(E)$ of a Fano resonance observed in a transport measurement can be described in the following form [89]:

$$G(\epsilon) = G_{nonres} + G_{res} \frac{(\epsilon + q)^2}{\epsilon^2 + 1},$$

(4.7)
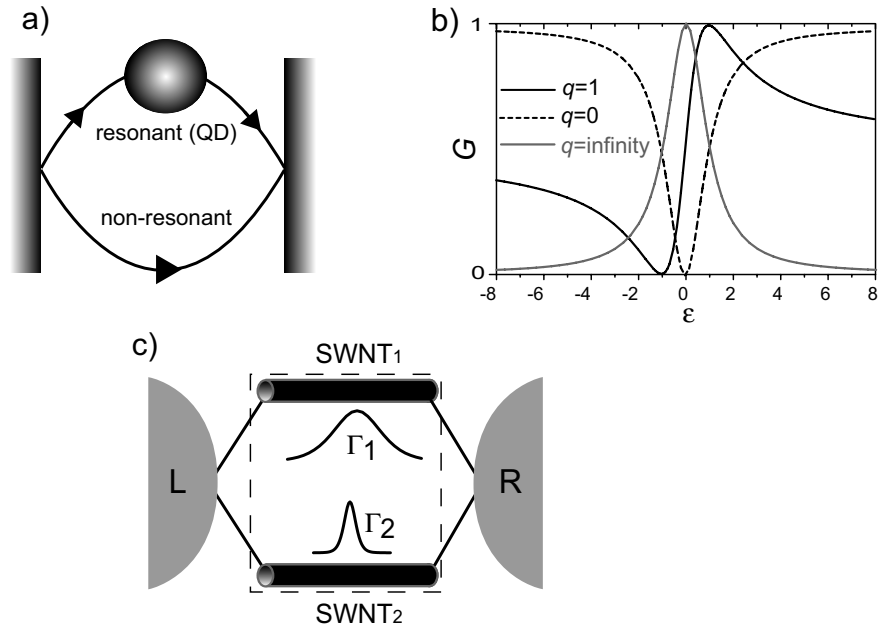
Figure 4.19: (a) Schematic view of a Fano system consists of a resonant channel through, e.g. a quantum dot (QD), and a non-resonant channels. (b) Normalized Fano line shapes calculated from Eq.4.7 for several asymmetry q parameters. (c) A scheme of two SWNTs connected to the left (L) and right (R) leads. Due to different coupling strength the zero-dimensional states of each SWNT acquires a different width expressed by $\Gamma_{1,2}$. The two interfering channels may be due to two 'individual' SWNTs of a bundle or may represent the two transport channels of one and the same SWNT.

where G_{nonres} and G_{res} denote incoherent and coherent contributions to the conductance. The detuning of the energy E from the center of the resonance E_0 is described by the dimensionless parameter $\epsilon \equiv 2(E - E_0)/\Gamma$, where Γ denotes the width of the resonant state. q is the so-called asymmetry parameter. Its magnitude is proportional to the ratio of the transmission amplitudes of the resonant and non-resonant channel. In the original Fano work [88], q was introduced as a real parameter, in general however, it must be treated as a complex quantity [120, 121, 122]. In the limit $q \to \infty$, resonant transmission dominates which leads to symmetric Breit-Wigner resonances, see Fig. 4.19b. In the opposite limit $q \to 0$, the resonant transmission appears as an anti-resonance, i.e. a symmetric dip. In all other

cases e.g. $q = 1$, asymmetric line shapes are obtained. These asymmetric line shapes are characteristic for the Fano effect and that is why one refers to them as Fano line-shapes.

Since the Fano resonance is the result of an interference effect, its line shape is sensitive to the phase difference between the two transmission pathways. Fano resonances can therefore provide essential information on dephasing in mesoscopic systems [123, 121, 122]. In this respect it has the same power as all other two-path ineterference experiments, for example the Aharonov-Bohm experiment [124].

Here we report on the observation of Fano resonances in electrical transport measurements on CVD-grown SWNTs, which were contacted by two macroscopic Pd electrodes, serving as source and drain contacts. We discuss the possible origin of the Fano resonances along the theoretical modelling.

4.4.2 Observation of Fano resonances in SWNTs

Fig. 4.20a shows the differential conductance in the form of a grey-scale plot for the same carbon nanotube (CNT) of Fig. 4.10, but now for a wider gate voltage range. The corresponding dependence of the linear response conductance on gate voltage V_g is displayed in Fig. 4.20b. For large positive gate voltages ($V_g \gtrsim 4\,\text{V}$) a clear Coulomb blockade pattern is observed. As the gate voltage is reduced cotunneling effects start to dominant, forming Kondo resonances within the well known four-fold shell pattern. This behavior indicates that the coupling of the CNT to the reservoirs can be increased substantially upon decreasing the gate voltage as discussed in the previous section. Reducing the gate voltage further and hence increasing the transparency to the contact blurs the Coulomb blockade diamonds. This signals the transition from a quantum dot to an open wire, which occurs if the life-time broadening Γ approaches the level spacing δE which is of the same order than the charging energy U_c. In the limit $\Gamma >> U_c$, interaction can be neglected. The overall transparency is then expected to approaches unity, which for a single nanotube with four channels relates to an upper bound in conductance of $G = 4e^2/h$. Because of residual backscattering at the contacts, a weak periodic conductance modulation is expected. This has been observed recently in SWNTs at a mean transparency of $T = 0.7$ [21] and was termed the Fabry-Perot interference effect. The mean net transparency in our device approaches $T = 0.5$ for the lowest gate voltage.

Instead of a smooth continuation from the cotunneling to the Fabry-Perot regime, sharp resonances appear below $V_g = 2\,\text{V}$. The two resonances visible in Fig. 4.20a (labelled 1 and 2) are identified by their asymmetric line shapes as Fano resonances. To show this, the measured gate dependence of the linear conductance for the two resonances is magnified in Fig. 4.21
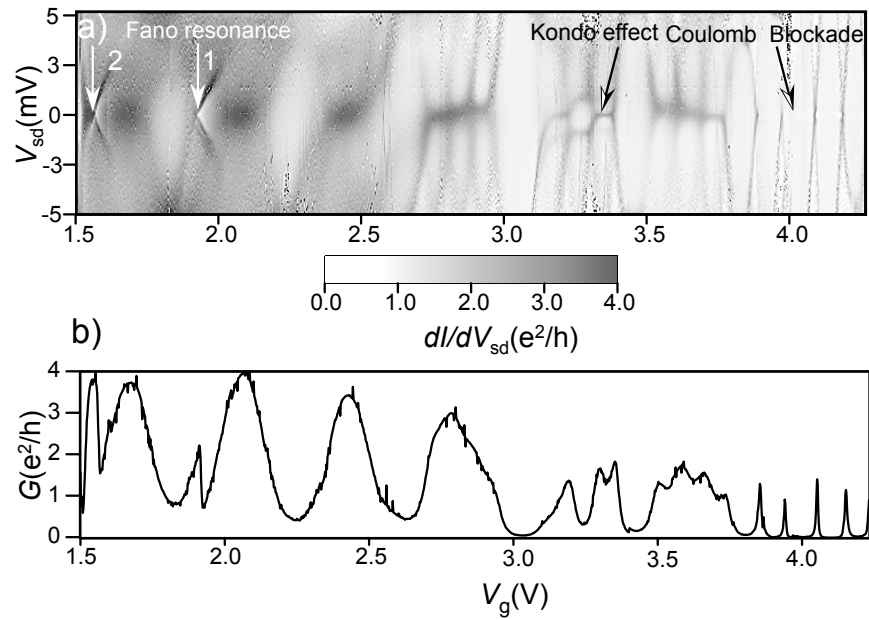
Figure 4.20: (a) Grey-scale representation of the differential conductance (dI/dV_{sd}) versus bias (V_{sd}) and gate voltage (V_g), and (b), the corresponding linear response conductance versus gate voltage. Due to the strong dependence of the tunneling coupling to the leads on gate voltage, several physical phenomena are observed together. These are from right to left: Coulomb blockade, the Kondo effect and Fano resonances, corresponding to regimes of low, intermediate and high tunneling coupling. Note, that the conductance dramatically increases for $V_g \lesssim 3\,\text{V}$ reaching a maximum value of $G \approx 4e^2/h$ as expected for an ideal metallic SWNT.
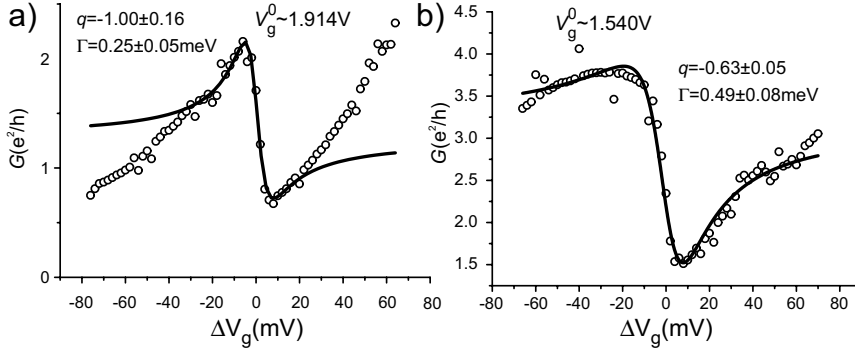
Figure 4.21: Comparison of the measured (symbols) linear response conductance G for the resonances labelled 2 (a) and 1 (b) in Fig. 4.20a with the Fano formula Eq. 4.7 (sloid curves). $\Delta V_g := V_g - V_g^0$, where V_g^0 denotes the gate voltage at the center of the resonance: $V_g^0 = 1.9$, $1.54\,\text{V}$ for resonance 1 and 2. The extracted values from the fits to the Fano equation are: $q = -1.0 \pm 0.16$, -0.63 ± 0.05 and $\Gamma = 0.25 \pm 0.05$, $0.49 \pm 0.08\,\text{meV}$ for resonance 1 and 2, respectively.

(symbols) and shown together with fits (solid curves) of Eq. 4.7 using the appropriate factor to convert gate voltage in energy (i.e. eC_g/C_Σ). Here, we compare two parameters that are obtained from the fitting procedure, Γ and q. Γ equals ≈ 0.25 and $\approx 0.5\,\text{meV}$ for resonance 1 and 2, respectively. Before, we have analyzed Γ in the cotunneling regime and found values $\sim 2\,\text{meV}$. Hence, the width of the two new features is substantially smaller than the width of the broadened nanotube levels. This difference gets even larger if we take into account that Γ grows further if one proceed from the cotunneling regime at $V_g \sim 3.5\,\text{V}$ to the 'open' regime at $V_g \sim 2\,\text{V}$. Both fits yield an asymmetry parameter q close to unity, i.e. $q = -1$ and $q = -0.65$ for resonance 1 and 2, respectively. An asymmetry parameter with a magnitude close to 1 corresponds to asymmetric line-shapes that are characteristic for Fano resonances, see Fig. 4.19b. We note that both resonances have comparable q parameters of order 1 and that the change in conductance is for both cases large and of order e^2/h. The Fano fit is very good for resonance 2 and it is reasonable for resonance 1. In the latter case the deviation are getting appreciable away from the resonance. Referring to the greyscale plot in Fig. 4.20a we see that this resonance is superimposed on a low-conductance and strongly blurred Coulomb blockade diamond. The assumption of the Fano description that the background contributes to the interference with a constant non-energy dependent term

is only approximately valid here. These two resonances will be analyzed further below.

The emergence of Fano resonances in single-wall carbon nanotubes is exciting and we have therefore measured this sample again, now lowering the gate voltage even further. This measurement is shown in Fig. 4.22. A complex pattern of resonances appears (arrows). We find resonances, anti-resonances and asymmetric Fano lines shapes. All features resemble Fano resonances for different q values. Although the overall pattern looks quite irregular at first sight, regular structures can be identified: In the first place one can identify 'inverted' Coulomb diamonds (indicated with white arrows) and secondly, all resonances have slopes which are quite comparable to the one in the Coulomb blockade regime suggesting that the nanotube itself is the source of the resonant state. The latter is also suggested by the fact that in the whole gate-voltage range the differential conductance reaches the maximum conductance for a single SWNT of $4e^2/h$, but never exceeds it.
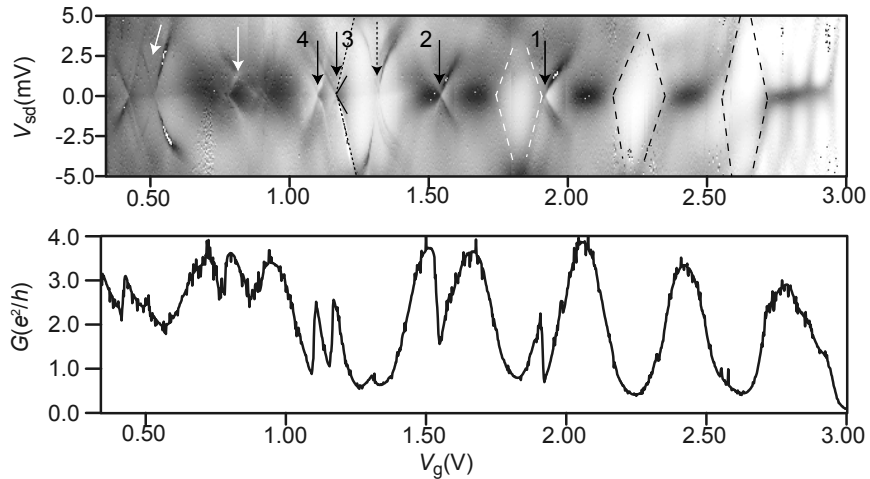
Figure 4.22: (a) Differential conductance (dI/dV_{sd}) versus bias voltage (V_{sd}) and gate voltage (V_g). Dark correspond to high (maximum= $4e^2/h$) and white to low conductance. Fano resonances are indicated with the arrows. (b) Corresponding linear response conductance G.

4.4.3   Discussion and Modelling

The origin of the interfering paths, necessary for the Fano effect, in mesoscopic devices is often unclear [89, 125]. In carbon nanotubes the first account of Fano resonances have been reported for crossed MWNTs [117]. Because these authors have not observed similar resonances in single tubes, they assigned the origin of the Fano resonance to the particular geometry of two crossed tubes. In further accounts of Fano resonances in MWNTs, the origin has been assigned to either an additional carbon nanotube [118] acting as the non-resonant background or to defects in the nanotube [119].

Our experiment is the first for single-walled carbon nanotubes (SWNTs) and the origin is puzzling as well. We point out, that an individual SWNT contains two channels (not counting spin), leading to the peculiar shell pattern of CNTs discussed before. In principle, this is enough for interference to occur. Assume that the two nearly degenerate eigenstates are coupled with different strength to the source and drain contacts, one with large coupling and the other with a weak one. Then, there is a broad and a narrow channel that can interfere and give rise to Fano resonances. This is schematically shown in Fig. 4.19c, where $SWNT_1$ and $SWNT_2$ refer to the two orbital channels. This problem has recently been studied theoretically in the limit of vanishing interaction [126]. Two quantum dot states are coupled to the reservoirs with different coupling parameters. The calculation shows that even for similar coupling strength the two-dot ground state consists of a narrow and a wide orbital. This is the result of hybridization leading to a symmetric bonding and an asymmetric antibonding state. The latter has a node at the contacts resulting in weak coupling to the leads and therefore a small effective width Γ. If all coupling terms are exactly the same, the life time of the antibonding states become infinite large. This never happens in practice, so that one can expect intrinsic Fano resonances in SWNTs. This is for sure the most attractive scenario. However, it is obvious that Fano resonances can also occur for two separate individual SWNTs, provided they are geometrically located within the phase-coherence length. Otherwise, a pure superposition of two individual conductance patterns are expected and not an interference effect. The problem of the interference between two quantum dot states has recently also been addressed using the scattering-(S)-matrix approach [127, 128]). These authors also derive the correspondence between the Green's function and S-matrix approach.

In the case of intrinsic Fano resonances (FRs) the regular periodic pattern, which is evident in our measurement in the Coulomb blockade and cotunneling regime, see Fig. 4.21a, should evolve into a periodic pattern of FRs at higher tunneling coupling. Although this looks promising in Fig. 4.21a, the FR pattern is rather irregular and certainly not periodic in Fig. 4.22a.

We therefore think that we do not observe intrinsic Fano resonances in a single tube but rather the interference of two (or possibly more) nanotubes. Our anlaysis of the CNT groundstate, for example the very low value of the exchange energy, has already hinted towards the close proximity of others tubes, which can screen the short-range interaction. It is therefore plausible that the interfering channels are embedded in a bundle of SWNTs. This would immediately make clear why the Fano resonances shift with gate and bias voltage in magnitude comparable to what is observed for the states in the Coulomb blockade regime.

Because we have measured both the gate and bias dependence we can extend our analysis of the Fano resonances further and try to fit the differential conductance in the vicinity of the resonance. Below, we will do this for the two resonances 1 and 2. We model the problem as two interfering channels in the Landauer-Büttiker formalism [124]. The transmission amplitude through the resonant channel is described by $t_r = \sqrt{T_r}i/(\epsilon + i)$, where $\epsilon = 2(E - E_0)/\Gamma$. The square modulus of this function corresponds to a simple Lorenzian. The transmission amplitude for the non-resonant channel is a constant $t_n = \sqrt{T_n}e^{i\phi}$, where the phase ϕ has been introduced. Assuming spin degeneracy, the conductance at zero temperature is given by $G(\epsilon) = 2e^2/h \cdot T_t(\epsilon)$ with the total transmission probability $T_t = \mid t_r + t_n \mid^2$. We obtain for T_t

$$T_t = T_n + \frac{1}{1+\epsilon^2}\Big\{T_r + 2\sqrt{T_r T_n}(\cos(\phi) + \epsilon\sin(\phi))\Big\}. \qquad (4.8)$$

The differential conductance can then be obtained from

$$\frac{\partial I}{\partial V_{sd}} = e^2/h\Big\{T_t(eV_{sd}/2 - \alpha V_g) + T_t(-eV_{sd}/2 - \alpha V_g)\Big\}, \qquad (4.9)$$

where $\alpha := C_g/C_\Sigma$ denotes the gate-coupling strength as before.

We first discuss the symmetry of Eq. 4.9 and the fitting procedure. The transmission amplitudes through the resonant and non-resonant channel are chosen such that the linear conductance is a Lorenzian for $\phi = 0$, whereas it has a Fano line shape ($q = \pm 1$) for $\phi = \pm\pi/2$. Far from the resonance ($\epsilon \to \infty$) the conductance asymptotically approaches the value of $2e^2/h \cdot T_n$. For $\phi = \pm\pi/2$, the total transmission probability is $T_t=(T_n + T_r)$ at resonance. Note, that the dI/dV_{sd} vs. V_{sd} characteristic will not have mirror symmetry for positive and negative gate voltages in general.

The following fitting procedure has been adopted: First, we fit the gate dependence of the linear conductance by changing the phase. Then, the dI/dV_{sd} curves vs V_{sd} are fitted for specific gate voltages close to the resonance. The phase is fixed, whereas T_n, T_r, α and Γ are free parameters.

Thereafter, the gate dependance is plotted again using the average parameters from the fits found from the non-linear regime. These average parameters are used to calculate the grey-scale plots.
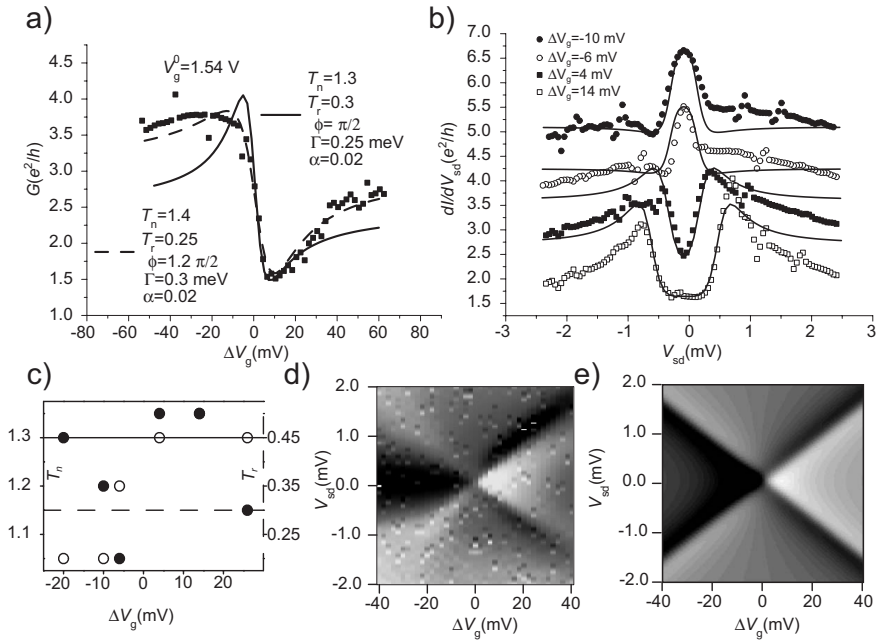
Figure 4.23: Comparison between the measured differential conductance of the Fano resonance 2 (see Fig. 4.22a) and fits to Eq. 4.9. In (a) the solid curve represents the best fit taking into account only the linear response conductance, whereas the dashed curve is calculated from average parameters deduced by fitting the non-linear differential conductance dI/dV_{sd} vs. V_{sd} for a set of gate-voltages, shown in (b). The curves are vertically offset by e^2/h for clarity. For a) the whole set of parameters are given in the figure, whereas we only represent the deduced transmission probabilities for the non-resonant T_n (full circle) and resonant T_r (open circle) channel of part (b) in (c). The calculated differential conductance (e) is compared with the measured one (d). The parameters are $T_n = 1.3$, $T_r = 0.3$, $\Gamma = 0.25\,\mathrm{meV}$, $\phi = \pi/2$ and $\alpha = 0.02$.

For both resonances this procedure yields a phase close to $\pi/2$ which agrees reasonably with the asymmetry parameter of $q \approx 1$ deduced before. The fitting has been preformed for four Fano resonances indicated with white arrows in Fig. 4.22a, but we present only the results for the resonances 1 and 2. We start with resonance 2, which is a particularly nice example.

Fig. 4.23a shows the gate dependence and Fig. 4.23b the bias dependence for four different gate voltages. The solid curve in Fig. 4.23a corresponds to the fit obtained from the linear conductance, whereas the dashed one shows the resonance using the average parameters deduced from the bias-dependence. We find for Γ values of $0.25 - 0.3\,\mathrm{meV}$ which is a bit less than before and a consistent gate-coupling parameter of $\alpha = 0.02$. The different values for T_n and T_r are plotted in Fig. 4.23c. The spread of $\approx \pm 0.15$ can be seen as a measure of the accuracy of this procedure. Up to this error $T_n = 1.3$ and $T_r = 0.3$. The average parameters are used to calculate the dI/dV_{sd} greyscale plot, which is shown together with the measurement in Fig. 4.23d and e. A reasonable agreement is found. The model clearly captures the main features and accounts for the correct energy scales. The transmission probability of the resonant channel of $T_r = 0.3$ relates to a conductance of $0.6e^2/h$, which is quite a substantial value. Whether this resonance is measured at the unitary limit could only be answered with temperature dependent measurement, which we have not preformed. However, this reduced value as compared to the unitary limit of $2e^2/h$ could simply reflect asymmetric couplings to the leads.

We now turn to resonance 1. As we have pointed out before, the agreement is less good here. This is due to the underlying blurred Coulomb blockade structure, which results in a sizable suppression of the conductance on one side of the resonance (left side), see Fig. 4.22a. The result of the same procedure is shown in Fig. 4.24. Fig. 4.24a displays the gate dependence of the linear conductance. The solid curve corresponds to the fit of the linear conductance vs gate voltage, whereas the dashed curve has been calculated from the average parameters deduced from dI/dV_{sd} vs. V_{sd}. Because of the mentioned suppression for $\Delta V_g < 0$, the differential conductance has only been fitted in the non-linear regime for three positive ΔV_g. This is shown in Fig. 4.24b, where we see that the fits match (apart from the asymmetry) the measurements quite well. Due to the strongly varying background a sizeable disagreement appears between the two fits in Fig. 4.24a. However, we think that this can be fully accounted for, by the background. The obtained parameters ϕ, α and Γ compare very well with the ones deduced before in Fig. 4.21b: $\phi = \pi/2$, $\alpha = 0.02$, and $\Gamma = 0.2\,\mathrm{meV}$. Not surprisingly the two fitting procedure yield somewhat different values for T_r and T_n. $T_n \approx 1$ and $T_r \approx 1.2$ in one case and $T_n \approx 0.6$ and $T_r \approx 0.25$ in the other.

Important for the following is the observation of an excitation line which appears at negative bias voltage in the measurement and is visible in Fig. 4.24b (arrows), as well as in the greyscale plot (inset). If we stick to the assumption that the cause of the Fano resonances is another tube, the deduced excitation energy of $\delta E = 0.6 \pm 0.1\,\mathrm{meV}$ should then corre-

spond to the level spacing of that nanotube. This is quite a small value as compared to the measured level spacing of $\delta E \approx 5\,\text{meV}$ in this tube, which agrees very well with the particle in a box model assuming spin and orbital degeneracy. If we assume only spin degeneracy for this small energy excitation feature, the underlying nanotube should have a length of as much as $L = 2.5\,\mu\text{m}$. This appears to be impossible, since the electrodes are spaced by only 300 nm. However, already in early work on carbon nanotubes (CNTs) two types of characteristics have been found [22]: Contacting tubes by evaporating metals over the tubes yielded 'end-contacted' CNTs [36], whereas CNTs lying on metal electrodes usually displayed a weaker coupling to the contacts and yielded 'bulk-contacted' tubes [36, 20]. Moreover, the single electron level spacing δE was found to agree with the contact separation from edge to edge in the first case, whereas the whole CNTs appeared to contribute, as apparent from small values of δE, in the latter. The states leading to Fano resonances in our measurements are also much weaker coupled to the leads. This is seen in the relative small Γ values deduced from the Fano resonances. Hence, the underlying resonant channel may very well be a weakly coupled SWNT which resides in one and the same bundle. This model is very likely because bundling in nanotubes is an ubiquitous phenomenon. It is strong in arc-discharge and laser-evaporated tubes, but it also occurs in CVD-grown CNTs (Chapter 2). There is, however, a remaining problem. If two tubes can contribute to transport, the maximum conductance does not have to be bound to $4e^2/h$. Future work will have to clarify this issue.

We next compare the gate-coupling parameter for the Fano resonance (FR) and the cotunneling regime. For the former we have obtained $\alpha = 0.02 \pm 0.005$, whereas $\alpha = 0.08 \pm 0.01$ for the latter. This is a significant difference amounting to a factor of four. The difference supports our picture as we explain now. Assume that there are indeed two tubes contributing to the conductance in a small bundle. The gate-capacitance C_g can be assumed to be roughly equal, while the capacitances to the leads should be strongly different. The weakly coupled tube, which electrically appears to be much longer than the contact separation, should have much larger source and drain capacitances. The four-times smaller α relates into a four-times larger total capacitance, and hence, into a four-times smaller charging energy. The cotunneling regime of this tube yields $U_c = 5.3\,\text{meV}$, so that the weakly coupled tube should have a charging energy of $U_c \approx 1.3\,\text{meV}$. Togther with the level spacing of $\delta E \approx 0.6\,\text{meV}$ yields an addition energy of $\Delta E \approx 1.9\,\text{meV}$. This relatively small addition energy explains the structure of the Fano resonances at $V_g \approx 1.2, 0.8\,\text{V}$ which are shaped in a diamond-like pattern with an energy scale corresponding to the reduced addition energy, see Fig. 4.22a. However, at even smaller gate voltage of $V_g \approx 0.5\,\text{V}$ an-
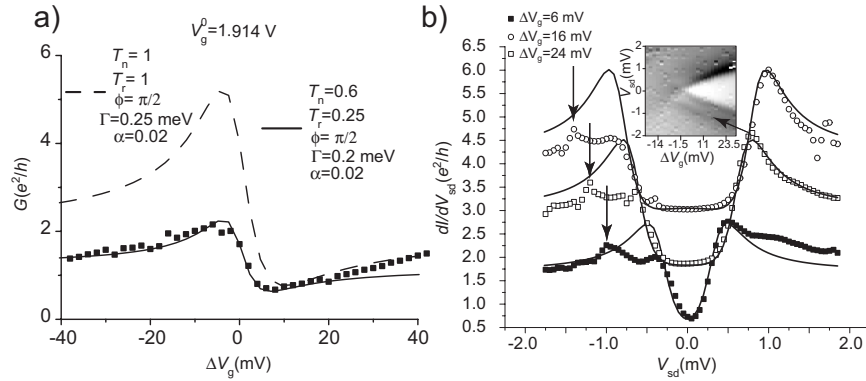
Figure 4.24: Comparison between the measured differential conductance of the Fano resonance 1 (see Fig. 4.22a) and fits to Eq. 4.9. In (a) the solid curve represents the best fit taking into account only the linear response conductance, whereas the dashed curve is calculated from average parameters deduced by fitting the non-linear differential conductance dI/dV_{sd} vs. V_{sd} for a set of (only) positive gate-voltages, shown in (b). The curves are vertically offset by e^2/h for clarity. For a) the whole set of parameters are given in the figure, whereas the parameters for the three fits in (b) are: ■: $T_n = 0.85$, $T_r = 0.9$, $\Gamma = 0.25\,\text{meV}$, $\phi = \pi/2$, and $\alpha = 0.027$; □: $T_n = 1$, $T_r = 1.2$, $\Gamma = 0.25\,\text{meV}$, $\phi = \pi/2$, and $\alpha = 0.02$; ◯: $T_n = 1.1$, $T_r = 1.4$, $\Gamma = 0.25\,\text{meV}$, $\phi = \pi/2$, and $\alpha = 0.017$. The observed asymmetry in bias voltage originates from different coupling of the resonant states to the leads. The inset in (b) shows the measured differential conductance. An excited state is visible for $V_{sd} < 0$, both in the greyscale plot and the $dI/dV_{sd}(V_{sd})$ (arrows).

other 'Fano-diamond' appears with obviously a larger addition energy, but also a larger coupling parameter. Hence, the interfering tube either evolves with increasing tunneling coupling from a weakly coupled 'long' tube to a stronger coupled end-contacted one, or yet other tubes start to participate in the interference.

With regard to the phases, which were obtained by fitting resonance 1 and 2, we mention that there is nothing peculiar about the value of $\phi = \pi/2$. The same fitting procedure has also been performed for Fano resonances (FRs) labelled in Fig. 4.22a with 3 and 4 (not shown). Here we obtain the following parameters: $T_n = 0.8$, $T_r = 0.2$, and $\Gamma = 0.23\,\text{meV}$ for FR 3 and $T_n = 0.73$, $T_r = 0.2$, and $\Gamma = 0.23\,\text{meV}$ for FR 4, while the phase is now negative amounting to $\phi = -\pi/2$. $\alpha = 0.02$ is consistent with the previous value and the same for both resonances. In addition, if we go further out

to even smaller gate voltages other phase values appear.

Finally, we briefly address the evolution of the Fano resonances (FRs) at larger source-drain voltage V_{sd}. We observe that most of the resonances vanish at $|V_{sd}| \gtrsim 2.5 \, \text{meV}$. This can easily be understood by noting that additional transport channels open up if $V_{sd} > \delta E$. In particular if $V_{sd} > \Delta E \approx 2 \, \text{meV}$ the resonant channel can involve excited levels for a fixed charge state and even different charge states. Because different phases are likely, the Fano resonance is smeared out. A peculiar FR is observed at $V_g \approx 1.3 \, \text{V}$ in Fig. 4.22a (dashed arrow). This resonance starts with a large gate-coupling α around zero source-drain voltage V_{sd} and evolves into a smaller coupling parameter α for larger V_{sd}. This apparent curving, which can also take up the reversed order, is currently not understood.

4.5 Conclusion

We have shown that a SWNT can act as a QD. Tunneling contacts are often formed between a CNT and metal electrodes driving the behavior of a QD at low temperatures to the CB regime. The large number of electrons on a CNT QD greatly simplifies the description of the system. Our experimental observations are in good agreement with the constant interaction model of CB. The deduced values for the charging energy and the level spacing suggest that the transport occurs through an individual SWNT and that the contact separation defines the size of the QD.

When the transparency of the contacts is increased cotunneling processes play dominant role in transport through a QD. The consideration of such higher-order processes is important for the proposed operation of single electron transistor, since these effects ultimately determine the accuracy of single charge transfer. In detail, the Kondo effect has been investigated in a QD formed from a metallic SWNT. We have confirmed the main predictions expected for the Kondo effect in the QDs: the logarithmic temperature dependance, the conductance resonance at zero bias and its splitting in a magnetic field. We observe the expected four-fold shell pattern for an ideal SWNT together with Kondo physics at intermediate transparency $G \sim 2e^2/h$ and a transition to the open regime in which the maximum conductance is doubled and bound by $G_{max} = 4e^2/h$. Except for the canonical example of Kondo $S=1/2$, we have analyzed the ground state of CNTs at half-filling, i.e. for $N = 2$ added electrons to one shell, and demonstrate that this state is either the singlet or a state for which the singlet and triplet are effectively degenerate, allowing in the latter case for the appearance of the Kondo effect at $N = 2$. The results presented here shows that many-electron phenomena as the Kondo effect as well as

the control of the single, localized spin are highly relevant for molecular nano-structures [83].

For the high transparency Fano resonances are observed. In a good approximation, the observed Fano resonances can be modelled as a simple interference between the resonant and non-resonant channels. Our measurements suggest that both channels correspond to individual SWNTs within a same bundle. The resonant and non-resonant channels are discriminated with different coupling to the leads. Although, the modelling seems to explain main observations, there are several issues which urge for the further investigations. For example, the dephasing in a CNTs due to Fano resonances should be possible to quantify, which is essential for the implementation of e.g. a spin transport in CNTs.

Finally we would like to emphasize even though some of the samples show nice consistency with the expected theory (for example constant-interaction model of Coulomb blockade), this is far away to be always the case. Complicated, less regular structure are often observed. At this stage, the transport research on CNTs relay on mass production of the samples where few of them are usually handful. Because of a poor control during the fabrication of the samples most of the crucial information are not known. The issues like: imperfection in a grown CNT, defects produced during their processing, contaminations, where and how nanotube makes contact to the leads, charged trapped on a substrate, etc; are still open questions. In this respect each CNT device is unique, which can to some extent explain discrepancies between the theoretical predictions and experimental observations. One such example is striking gap structure observed around zero bias, for several samples in different transport regimes (sequential electron tunneling and cotunneling). On the other hand, it is still not well understood when and how important is 1D nature of SWNT (the Luttinger liquid model) in the interpretation of its transport properties. Recently, some evidences for Luttinger liquid behavior have been presented [22, 32]. In our opinion further research is needed to experimentally address this issue in the controlled manner.

Chapter 5

# *Intrinsic thermal vibrations of suspended doubly clamped single-wall carbon nanotubes*

In this chapter, we report on the observation of thermally driven mechanical vibrations of suspended doubly clamped carbon nanotubes, grown by chemical vapor deposition (CVD). Several experimental procedures are used to suspend carbon nanotubes. The vibration is observed as a blurring in images taken with a scanning electron microscope. The measured vibration amplitudes are compared with a model based on linear continuum mechanics.

5.1 Carbon nanotubes as high frequency resonators

Carbon nanotubes (CNTs) form a material with unique mechanical properties [43, 44, 129, 130, 131]. The high Young's modulus and low specific weight qualify single-wall carbon nanotubes (SWNTs) as ultimate mechanical resonators. Similar to lithographically patterned SiC beams, whose resonance frequency has recently crossed the border from MHz to GHz [132], it would be highly desirable to integrate CNTs into nanoelectromechanical systems (NEMSs) and to electrically excite the mechanical vibration modes [133]. A first step in this direction has been the observation of electrically driven mechanical vibrations of multi-wall carbon nanotubes [44]. Nanometer-sized resonators oscillate at high frequencies, but simultaneously have small vibration amplitudes, which are difficult to measure. At cryogenic temperatures, the resonant adsorption of an external electromagnetic field could successfully be measured using superconducting elements attached to a freely suspended CNT [134]. At room temperature a tunnelling

probe in the form of, for example, an STM tip would be a versatile detector. Integrating a sensitive measuring transducer with a CNT nanomechanical oscillator is however challenging. In a first step, it would be desirable if the mechanical vibrations could be imaged directly. Here, we report on the observation of thermal vibrations of suspended doubly clamped SWNTs, imaged by scanning electron microscopy (SEM), which is schematically illustrated in Fig. 5.1.
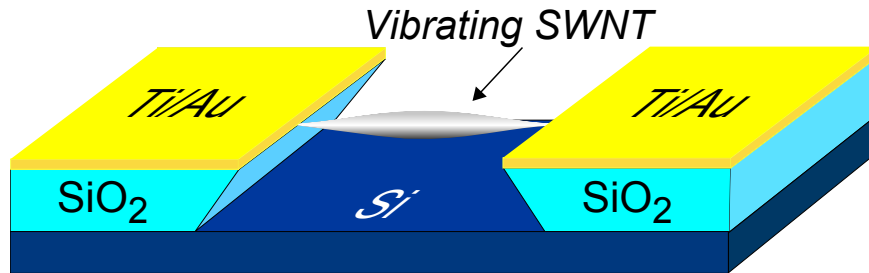
Figure 5.1: A schematic illustration of vibrating doubly-clamped SWNT. Blurring in the middle is expected for a sample observed with a SEM.

Thermally driven excitations of multi-wall carbon nanotubes (MWNTs), clamped at one end only, were first investigated by Treacy *et al.* [43]. The mechanical oscillation appeared in the images, which were collected with a transmission electron microscope (TEM), as a blurring that increased towards the free end of the MWNTs.

5.2   Doubly clamped SWNT

In order to see whether a similar experiment is possible with doubly clamped SWNTs, we will first estimate the expected amplitude in thermal equilibrium at room temperature. A schematics with coordinate system is shown in Fig. 5.2a. Assuming that linear continuum mechanics is a good approximation, the equation of motion for the vertical displacement ξ is given by [135]

$$\frac{\partial^2 \xi}{\partial t^2} + \left(\frac{YI}{\rho A}\right) \frac{\partial^4 \xi}{\partial x^4} = 0. \tag{5.1}$$

Here, ρ is the mass density, A the cross-sectional area, Y the Young's modulus, and $I = \pi d^4/64$ the moment of inertia, which depends only on the diameter d. Applying the boundary conditions for doubly clamped beams, i.e. $\xi = 0$ and $\xi' = 0$ at the two boundaries, the spectrum of eigenfrequencies

is obtained:

$$\omega_i = \frac{\beta_i^2}{L^2} \sqrt{\frac{YI}{\pi d \rho_{2d}}} \quad (i = 1, 2, 3 \dots) , \tag{5.2}$$

where L is the suspended length, ρ_{2d} is the surface mass density of a graphite sheet $(7.7 \cdot 10^{-7}\,\mathrm{kgm^{-2}})$ and $\beta_1 = 4.73$, $\beta_2 = 7.85$, and $\beta_3 = 11.0$ for the first three modes.

The equipartition theorem predicts that each vibration mode carries the energy $k_B T$ in thermal equilibrium at temperature T, where k_B is the Boltzmann constant. Together with the appropriate solutions of Eq. (5.1), one obtains an expression for the variance of the maximum deflection amplitude, which for the fundamental frequency $(i = 1)$ occurs in the middle:

$$\sigma_1^2 \equiv < \xi_1^2(L/2) > = \frac{k_B T L^3}{\gamma_1 YI}, \tag{5.3}$$

where $\gamma_1 = 192$ [136]. Table 5.1 summarizes the eigenfrequencies and the thermal vibration amplitudes at room temperature of a 'typical' SWNT with diameter $d = 1.5\,\mathrm{nm}$ and Young's modulus $Y = 1\,\mathrm{TPa}$ for different (practically feasible) suspension lengths $L = 0.2 - 5\,\mu\mathrm{m}$. This table demonstrates that thermal vibration amplitudes can be of appreciable magnitude, of order $\approx 10\,\mathrm{nm}$ $(L = 1\,\mu\mathrm{m})$. Since state-of-the-art scanning electron microscopes have resolutions well below $10\,\mathrm{nm}$, thermal vibration should appear on SEM images.

Table 5.1: Characteristic quantities of a suspended SWNT $(d = 1.5\,\mathrm{nm}$, $Y = 1\,\mathrm{TPa})$. The eigenfrequencies and maximum thermal amplitudes are calculated using relations (5.2) and (5.3), respectively.

| $L\,(\mu\mathrm{m})$	$\omega\,(\mathrm{MHz})$	$\sigma_1\,(\mathrm{nm})$
0.2	4600	0.8
0.5	740	3.4
1	185	9.3
3	21	48.3
5	7.4	104

There are already many reports on the fabrication of suspended CNTs. For example, SWNTs were grown between distant silicon towers [137, 138], spread over metal posts [139], or grown over solid terraces [140] and etched trenches [131]. Though devices with suspension lengths of $L \gtrsim 5\,\mu\mathrm{m}$ were realized and imaged with SEM, the thermal vibration has surprisingly not

yet been reported, although it should readily have shown up in respective SEM images, provided the reported SWNTs were *single* SWNTs. In the work of Dai and coworkers [137, 138, 140], the SWNTs were coated with a metal layer to increase the contrast in the SEM, whereas others have explicitly reported on suspended *ropes* of SWNTs or MWNT [130, 139], which are inherently stiffer.

5.3   Sample fabrication

Carbon nanotubes are synthesized by chemical vapor deposition (CVD) as previously reported [141]. We would like to emphasize that not all grown CNTs are individual SWNTs. This will be explained further in the text. To account for the possible influence of substrate during imaging in SEM, we have suspended CNTs using three different methods.

Method I, shown in Fig. 5.2b, is based on the work of Nygård *et al.* [142]. The CNTs are grown on thermally oxidized (400 nm) Si substrates. Electrical contacts are patterned by electron-beam lithography (EBL), followed by evaporation (Ti/Au) and lift-off. The SiO_2 is etched in buffered HF [143]. To stop etching, the sample is heavily rinsed in water followed by isopropanol. With this method we find it possible to suspend CNTs over distances up to $1\,\mu$m. For larger lengths, the surface tension of the etchant tends to pull the CNT down to the substrate.
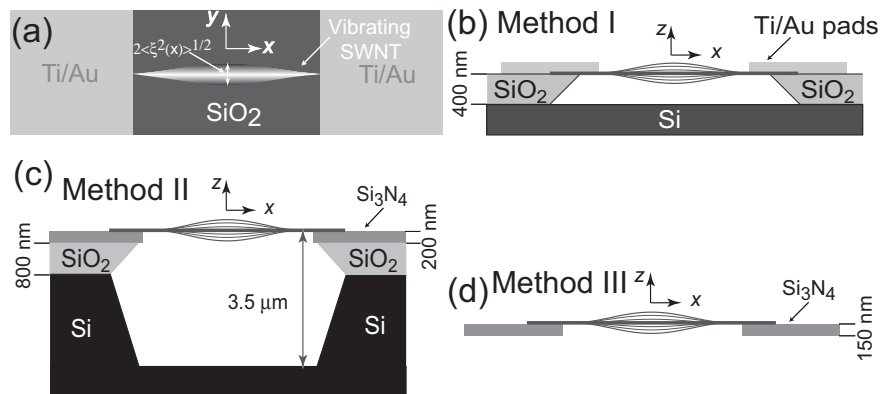
Figure 5.2: Schematic drawings of doubly clamped vibrating SWNT which are suspended by different methods. (a) top view, (b-d) side views.

In method II, shown in Fig. 5.2c, the CNTs are grown across predefined trenches. We start with a Si substrate with layers of 800 nm of SiO_2 and 200 nm of Si_3N_4. Slits of width $1-5\,\mu$m and length $10\,\mu$m are first etched

into the top Si_3N_4 layer using a CHF_3-based plasma etching process [144]. Next, the slit is further wet-etched into SiO_2 and the Si substrate using HF and KOH [145], respectively. This results in deep trenches $\sim 3.5\,\mu$m, a prerequisite for CNTs to bridge the trenches in the CVD growth process.

In method III, shown in Fig. 5.2d, slits are defined in Si_3N_4 membranes of thickness 150 nm and lateral size 0.5 mm following a similar procedure as in method II.

The key difference between the three methods is the depth of suspension. It is 400 nm, $3.5\,\mu$m, and ∞ for methods I-III, respectively. The samples are imaged with SEM (Philips XL30 FEG) at room temperature. To generate an image, a focused electron beam is raster scanned.

5.4   Results

To deduce the vibration amplitude quantitatively two assumptions have to be made: 1) the intensity profile of the electron beam centered at coordinate (x, y) has a Gaussian distribution and 2) the measured intensity of secondary electrons reflects the (time-averaged) probability $P(x, y) \equiv P_x(\xi)$ to find the CNT at position (x, y) convoluted with the intensity profile of the primary beam. 1) is a convenient assumption and 2) should hold, because scanning in SEM is slow as compared to the vibration of the CNT. The latter results in a blurring of the CNT in SEM images. The examples of a vibrating suspended CNTs are shown in Fig. 5.3a and b. The vibration is observed as a blurring, which is largest in the middle. In contrast, the CNT appears sharp at the edges of the trench, limited by the finite resolution of the SEM. To deduce the vibration amplitude, more precisely the variance $\sigma^2(x) \equiv \langle \xi^2(x) \rangle$, we note that $P_x(\xi)$ is Gaussian and determined by Boltzmann statistics. The deconvolution is simple because of assumption 1). We only need to extract $\sigma^2(x)$ from the intensity distribution of the SEM image perpendicular to the CNT and subtract $\sigma^2(0)$. To do so, we average the intensity profile in Δx slices as shown in Fig. 5.3c and fit it to a Gaussian. Such an analysis was first done for MWNT cantilevers by Krishnan *et al.* [43].

Figure 5.3c shows a SEM image of a suspended doubly clamped vibrating CNT fabricated by method I. The free suspension length is relatively short, i.e. $L \approx 650$ nm. Applying the analysis procedure mentioned above, the maximum rms vibration amplitude is determined to be $\sigma = 27 \pm 5$ nm. We have also analyzed σ as a function of x and compare the result with analytical curves for the first three eigenmodes in Fig. 5.3d. The agreement between the measured points and the theoretical curves is reasonably good. Matching between experiment and theory is improved if the first *and* second modes are taken into account, each of which carries $k_B T$ energy. Contri-
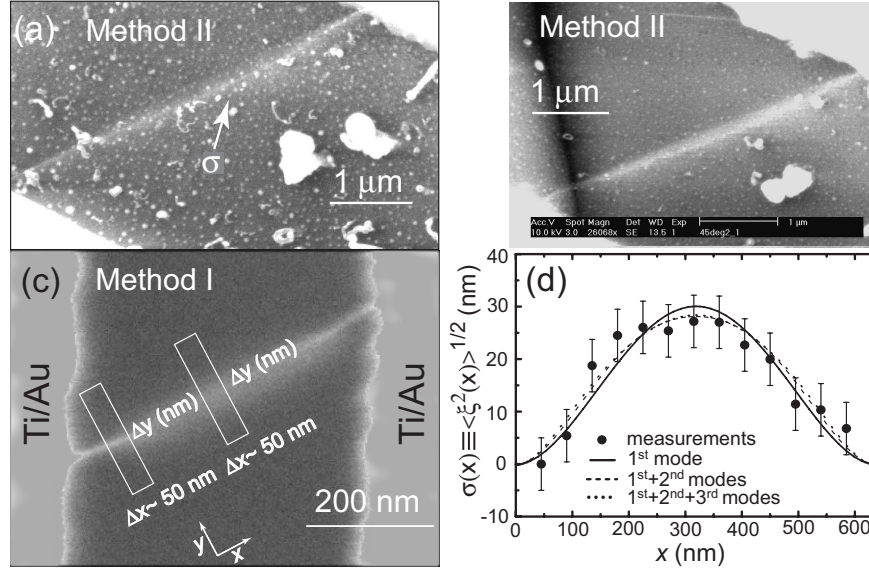
Figure 5.3: (a) and (b) SEM images of a vibrating SWNT grown over a trench. A strong blurring is clearly visible (indicated by arrows), which is a consequence of intrinsic thermal vibrations. (c) Another vibrating SWNT, whose root-mean-square displacement along x is plotted in (d). Circles are measured points and the curves represent fits.

butions from higher order modes decay very rapidly and can be neglected. Note, there is one fitting parameter Yd^4, which will be discussed below.

Figure 5.4a shows another CNT grown over Si_3N_4 membrane. Here, the suspension length is rather large, i.e. $L \approx 6.2 \,\mu$m. Correspondingly, the observed blurring is much larger. The maximum rms vibration amounts to $\sigma = 80 \pm 5$ nm. Applying Eq. (5.3) and assuming the typical high Young's modulus value of SWNTs of $Y = 1$ TPa the diameter of this CNT is estimated to be $d = 2 \pm 0.5$ nm.

The SEM image displayed in Fig. 5.4b shows three suspended CNTs. Though grown in one run, only one CNT seems to vibrate, namely the middle one. This, at first sight surprising result, points to a variability of CNTs that are grown during one and the same process. The only parameter in our experiment, which is not predetermined, is Yd^4, see Eq. (5.3). Though different values for the Young's modulus were reported, we suspect that the diameter d is the cause for the variability, because it enters in the fourth power. The absence of visible vibrations for the upper and lower CNT in Fig. 5.4b suggests that these have a larger diameter. They may be multi-
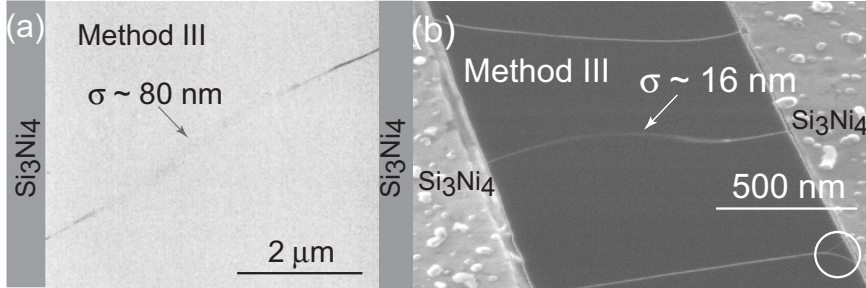
Figure 5.4: (a) SEM image of long ($L \approx 6.2\,\mu$m) vibrating SWNT grown over a slit in a Si$_3$N$_4$ membrane. In (b) three CNTs are imaged simultaneously. Only the middle one is vibrating. A white circle indicates branching of the lower CNT into two CNTs.

wall nanotubes or ropes of tubes. In fact, the lower one must be a rope, because a clear branching is observed at the right end (highlighted by a circle). Having looked through a large number of samples, the fraction of vibrating tubes is very small (a few %). This is a clear indication that not all of the grown CNTs are SWNTs.

Table 5.2: Properties of some vibrating CNTs. L is the suspended length, σ the measured maximum rms vibration, Yd^4 obtained using Eq. 5.3, $Y_{1.6}$ Youngs' modulus assuming $d = 1.6$ nm (see text), and d_1 the CNT diameter assuming $Y = 1$ TPa.

L (μm)	σ (nm)	Yd^4 (GPa(nm)^4)	$Y_{1.6}$ (GPa)	d_1 (nm)	Method
0.55	25	117	18	0.58	I
0.63	27	150	23	0.62	I
1.35	16	4221	644	1.4	III
4.05	85	4038	616	1.4	II
4.30	90	4311	658	1.45	II
6.25	80	16754	2556	2.0	III

We summarize the measured rms vibration of several CNTs in table 5.2. Determined are L and $\sigma(L/2)$. Using Eq. (5.3), we obtain an estimate for Yd^4, which is given in the third column. What is immediately noticed is the large spread in Yd^4 of more than two orders of magnitude. Unfortunately, we are not able to unambiguously deduce the Young's modulus Y and diameter d, independently. We have tried to measure the diameter using atomic-force microscopy (AFM). Due to surface roughness and the strong d^4 dependence, the error bar is too large to deduce Y with an acceptable accuracy. For the

discussion we instead rely on an average diameter for SWNTs, which we have obtained from electrical measurements of contacted semiconducting CNTs [67]. We have analyzed the band-gap, which is inversely proportional to the diameter d, of more than 10 semiconducting SWNTs and obtained as an average $d = 1.6 \pm 0.3$ nm. We note, that taking this diameter, the estimated Young's modulus (column 4 in table 5.2, denoted by $Y_{1.6}$) has an accuracy of 'only' 75 %. Well graphitized CNTs have a large Young's modulus. For example, $Y = 1.4 \pm 0.4$ TPa was reported for SWNTs grown by laser ablation [43], whereas 1 TPa was found in simulations independent of helicity and number of shells [146]. In column 5 of table 5.2 we therefore also list the diameter d_1, which we deduce from the measured $Y d^4$, assuming $Y = 1$ TPa. d_1 is varying between 0.58 to 2.0 nm. Since we have never observed SWNTs with diameters < 1 nm in TEM, the first two CNTs (row 1 and 2), both belonging to samples prepared by method I, cannot have a large Young's modulus $Y \sim 1$ TPa. Taking d to be 1.6 nm leads to a modulus of only $Y_{1.6} \approx 20$ GPa. Because method I uses HF-etching, it is possible that the NT's are affected during this process step. It is also possible that the under-etching changes the clamping conditions (boundary conditions) at the edges. In contrast to method I, the as-grown CVD CNTs of methods II and III yield consistent results, which are in agreement with a large Young's modulus of 1 TPa and with the diameter, which we have deduced by electrical measurements. Though we observe ropes and small diameter MWNTs (only a few number of shells) in TEM, their diameter is typically larger than 2 nm. This strongly suggests that the CNTs of row $3 - 6$ in table 5.2 are *single*-wall carbon nanotubes.

To our knowledge there are no reports on the Young's modulus of CVD-grown SWNT. Though we are not able to accurately determine Y, our results suggest that CVD-grown SWNTs can have a large modulus of order $Y \approx 1$ TPa. The exception are wet-etched CNTs, for which our data suggest $Y \ll 1$ TPa. Small Young's modulus have previously been reported for CVD-grown MWNTs [147].

5.5 Conclusion

In conclusion, we have demonstrated that it is possible to observe thermally driven vibrations of suspended doubly clamped SWNTs in SEM. From the measured rms vibration amplitude, the Young's modulus Y of CVD-grown SWNTs has been estimated. Only a small fraction of suspended CNTs are seen to vibrate, although they are suspended over a comparable length and grown at the same time. This suggests that the majority of grown tubes are *not* single SWNTs, but rather ropes and MWNTs, a finding, which is supported by TEM. We suspect that this is the reason why thermal vibrations of SWNTs has not already been observed before.

Chapter 6

Summary

Single-wall carbon nanotubes after a decade of research show fascinating properties with a promising prospective for possible applications. Their nanometer size and micrometer lengths make them an ideal material for research in nanotechnology. Contrary to most of the molecules, experiments in different scientific areas have been possible due to their robust, chemical inert characteristics (Chapter 1).

We have successfully produced CNTs by CVD method. It has been shown that this method is well suited for the investigation of their electrical and mechanical properties. The main advantages of the CVD technique is that CNTs can be grown at specific location with flexibility to routinely implement them for different investigation purposes. Their electronic transport properties have been explored by fabricating the contacts by EBL or optical lithography in straightforward manner. In this thesis, investigation has been focused on CNT's electronic transport properties from room to low temperature. Although their main characterization at room temperature (the gate dependance and high bias characteristics) does not depend dramatically on the contact resistance, low temperature measurement reveal the importance of the contact resistance and their correlation with the observed phenomena. We have found that problem of the contact resistance can be overcome by annealing of the devices contacted with Ti or using Pd as metallic electrodes on as grown CNT (Chapter 2).

Ambipolar field-effect transistor action has been demonstrated on as-grown semiconducting SWNTs (Chapter 3). The observed ambipolar FETs can be tuned with a back-gate from p- to n-type conduction through the semiconducting gap. We have attributed high tunability of our devices to hydrogen presence during the CVD grow, which probably reduce trapped charges in a Si/SiO_2 substrate, making coupling to the gate more effective. Electron and hole transport in the Coulomb blockade regime have been investigated in detail. A strong sensitivity on disorder has been observed in

semiconducting SWNTs, which effectively brake the nanotube in small sections $\approx 40\,\mathrm{nm}$ forming multi-dot system. However, for sufficient doping i.e. by the gate voltage, localized states can be populated, where the transport occurs through an individual orbital. Moreover, doping of the tube section to higher subbands has been demonstrated.

Detailed, two terminal transport measurements at low temperature have been performed on the metallic SWNT devices (Chapter 4). Spectroscopy on a SWNT QD can be performed by measuring the conductance as a function of the gate and bias voltages. For low transparent contacts, a SWNT behaves as a quantum dot where the transport phenomena are dominated by the single-electron charging effect (Coulomb blockade). For high transparent contacts, the four-fold degeneracy is observed with the Kondo effect. We have discussed several possible shell filling scenarios in SWNTs. In detail, the ground state of CNTs at half-filling, i.e. for $N = 2$ added electrons to one shell, is analyzed. We demonstrate that this state is either the singlet or a state for which the singlet and triplet are effectively degenerate, allowing in the latter case for the appearance of the Kondo effect at $N = 2$. For even higher transparency Fano resonances are observed. The origin of these resonances are identified as an interference between the resonant and non-resonant channels within a bundle of SWNTs.

Finally, as grown CNTs have been suspended with three different methods to explore their mechanical properties (Chapter 5). We have shown that thermal vibrations are readily observed in SEM if the suspended length of a SWNT is sufficient ($\gtrsim 1\,\mu\mathrm{m}$). Good agrement is found between thermal vibration derived for an elastic beam in continuum mechanics, with corresponding Young's modulus in TPa range. However, for the SWNTs suspended by wet etching Young's modulus seems to be smaller ($\approx 20\,\mathrm{GPa}$). The possible interpretations are that wet etching severely damage CNT or that the boundary conditions are different than in the cases for the growth over predefined trenches and $\mathrm{Si_3N_4}$ membranes. Our investigation showed that possible implementation of CNTs as nano-electromechanical resonators urges for careful design of the experiments with desirable control of their physical properties (diameter).

In this thesis, we have demonstrated that transport investigation in CNTs show pronounced quantum effects with fascinating possibilities to explore the fundamental phenomena which has been elusive in other systems (S-QD-S, spin injection in low dimensional systems, Luttinger liquid, etc). In that respect, the exploration of CNTs opened a new chapter in material science and nanotechnology, as important milestone for the future investigation of molecular based devices.

Appendix A

Device fabrication and measurement set-up

The fabrication of nanotube devices presents main practical challenge in the experimental studies of these systems. To preform different kinds of experiments wide range of processing techniques have been used which are analogous to semiconductor nanostructuring. In this chapter we will describe how we have implemented a CNT device fabrication, with emphasize on structuring techniques which enables us to preform transport measurements on CNTs connected to external electronic circuits. Moreover, the transport measurement set-up from room to low-temperature is described.

A.1   Electron beam lithography and evaporation

All devices used in electronic transport measurements have been made on silicon wafer, capped with a silicon-dioxide layer with typical thickness of $400\,\mathrm{nm}$. The silicon substrate is degenerately doped $(p++)$ to conduct at low temperatures $(T < 1\,\mathrm{K})$ where it can be effectively used as a back-gate.

The PMMA resist (Poly-methacrylate 950 K from *Allresist*) for EBL is used with typical thickness between $500-600\,\mathrm{nm}$. The resist is first spun on the substrate and then baked for 45 minutes at $T{=}175\,^{\circ}\mathrm{C}$. The desired electrodes, markers or catalyst deposition patterns are structured with EBL technique. Our system consists of a JEOL (model *JSM:IC848*) equipped with Proxy software. The microscope is operated at $35\,\mathrm{keV}$ acceleration voltage. Used electron beam (e-beam) current depends on the size of the written structures. For the structures with a writing field of $200\,\mu\mathrm{m} \times 200\,\mu\mathrm{m}$ or less, a beam current of $45\,\mathrm{pA}$ is used, while for bigger structures typically $18.5\,\mathrm{nA}$ are used. The size of the writing field A depends on the magnification settings on the microscope, M, in the following
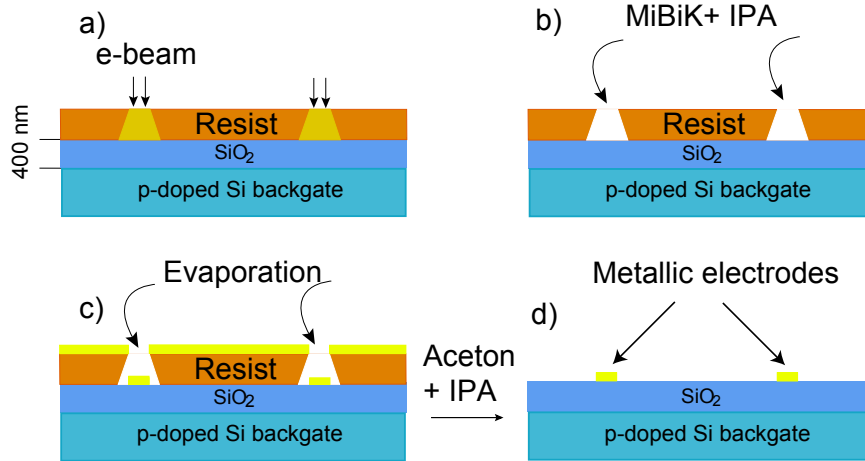
Figure A.1: Illustration of EBL lithography, followed by evaporation and lift-off. (a) Desired pattern is structured by EBL, where PMMA is exposed by e-beam at specific positions. (b) The pattern is developed in appropriate solvent. (c) Metal is evaporated onto the substrate. (d) Remaining resist is dissolved in acetone, leaving the metal electrodes only at the positions which have been patterned by EBL.

way:

$$A \times M = 50000. \tag{A.1}$$

For example, a typical writing field of $200 \times 200\,\mu\text{m}^2$ the appropriate magnification is 250.

Exposed structures can be developed (PMMA is removed) due to the fact that the areas of PMMA resist which have been exposed to e-beam irradiation have higher solubility then unexposed ones. The structured patterns are developed by dipping the wafer in appropriate solvent. As solvent we use methyl-isobutyl-ketone (MIBK) diluted in 2-propanol (IPA) in 1:3 volume ratio, for 45 sec, followed by rinsing the wafer in IPA for additional 45 sec. The substrate with developed structures is then transferred to evaporation chamber (*Balzers Pfeffier* PLS 500) with base pressure $< 10^{-7}$ mbar. It rotating stage with multiple target pockets enable us to deposit different metals during the same evaporation process without breaking the vacuum. Once the desired metals are evaporated, the substrate is transferred to acetone to dissolve the resist and subsequently it is rinsed in IPA. With this the so-called lift-off technique metal deposited in predefined patterns remains,

forming now the desired electrode pattern. In Fig. A.1 different procedures are schematically illustrated for the fabrication of metallic electrodes on a Si/SiO_2 substrate. SEM (*Philips XL30 FEG*) images of different patterns made by EBL followed by evaporation are shown in Fig. A.2.
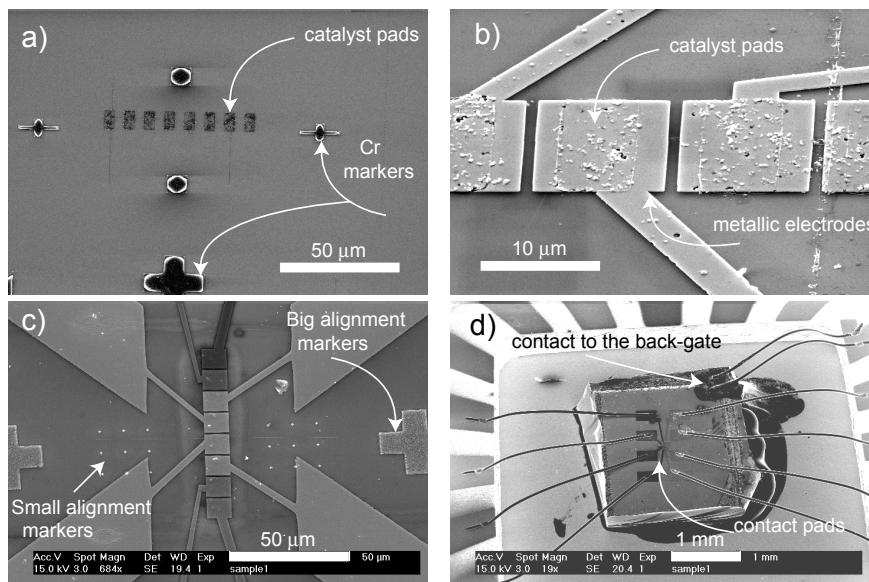
Figure A.2: The SEM images of different structures patterned by EBL during the preparation of the SWNT devices. (a) Catalyst islands and Cr alignment markers. (b) Catalyst pads covered with metallic electrodes. (c) Contacts with different alignment markers. Big Cr markers serve for rough alignment and small ones for precise alignment (200 nm). With EBL, contacts can be written corresponding to the alignment markers. (d) A sample glued on a chip carrier. Bonding pads are connected by an Al wire ($d = 50 \,\mu$m) to the pads on the chip. A back-gate is connected by silver-paint followed by bonding on one of the chip pads.

Up to now the influence of the e-beam irradiation on CNT devices has not been fully understood. We found that EBL processing does not seem to influence dramatically the final characteristics of the CNT devices. Nevertheless, the exposure of prepared devices to e-beam irradiation can dramatically degrade their characteristics. Fig. A.3 shows the change in a metallic CNT conductance characteristic before and after the exposure to e-beam irradiation near the contacts.
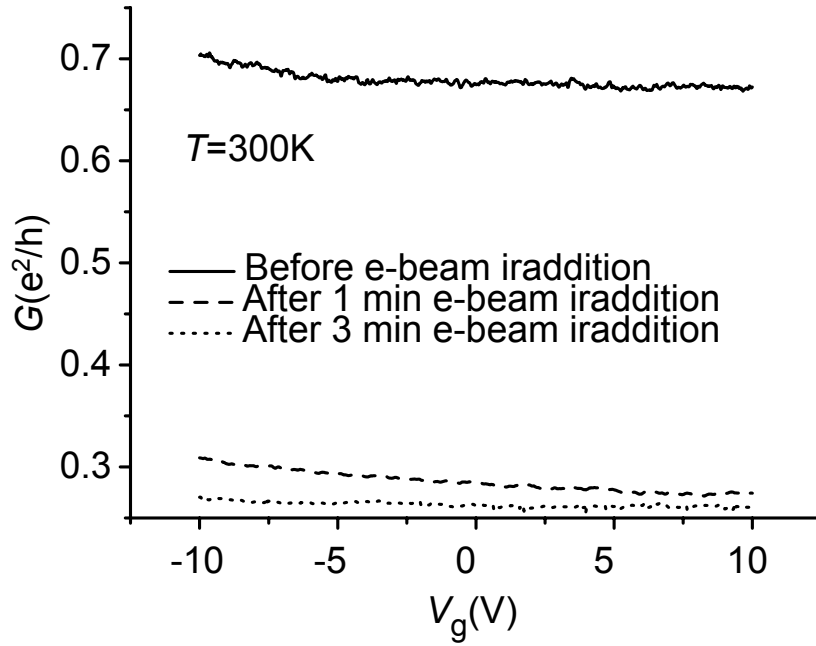
Figure A.3: Dependance of the conductance versus the gate voltage for a CNT device. E-beam is irradiated by SEM at acceleration voltage of $15\,\mathrm{keV}$ in vicinity of the physical contact between CNT and a lead.

A.2 Electronic set-up and cryostat

Once the samples are structured on the substrate they are cut in individual devices by a diamond knife and glued onto a commercially available chip carrier. The electrodes are connected to the pads on the chip by an ultrasonic bonding machine.

At room temperature, samples are characterized in a test box. The test box consist of a chip holder with 25 BNC connections. All the devices are measured in two-terminal DC (voltage bias) set-up as illustrated in Fig. A.4. The source electrode is biased with a voltage V_{sd} and current I is measured via a low noise current to voltage amplifier. The output voltage from the current amplifier is recorded by a digital voltmeter connected via DAQ card to PC. Furthermore, a voltage V_g is applied to the gate (substrate). The acquisition of data and control of the input parameters in the experiments are acquired with a PC equipped with Lab-View software.
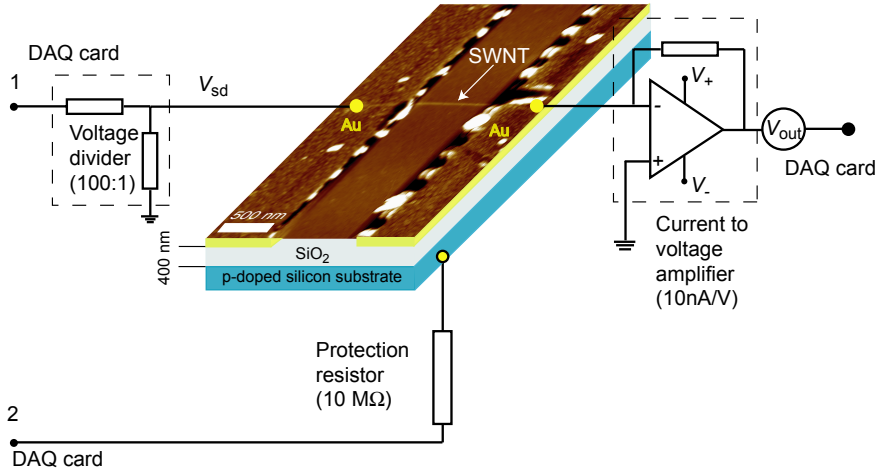
Figure A.4: A schematic diagram of the electronic set-up used for low temperature DC transport measurements on CNT devices. Sample is biased by an applied voltage (V_{sd}) through a voltage divider (100:1). Simultaneously, voltage V_g is applied to the back-gate. Current through the sample is amplified and converted to voltage by a current to voltage amplifier. Finally, out-put voltage is recorded by a digital voltmeter.

For a simple characterization at low temperature ($T \gtrsim 4.2\,\mathrm{K}$) a dip stick is used which is inserted into a helium transport dewar. The sample can be brought to equilibrium at higher temperatures by raising the holder above the helium level. The temperature is measured by a thermometer mounted on the sample holder.

For the studies at lower temperature a ^{3}He system (from Cryogenics) is used with a base temperature around $300\,\mathrm{mK}$. Since the vapor pressure of ^{3}He is much smaller than that of ^{4}He, pumping on the ^{3}He space leads to lower temperatures than pumping on ^{4}He. Once ^{3}He is condensed, pumping is preformed by cooling charcoal adsorbate pump below $20\,\mathrm{K}$. Since this is a commercial system operated by well known principles we will just mention that the condensation to the base temperature typically has taken $1-2$ hours, while the base temperature is preserved around 20 hours. The reduction of electrical noise in the system is filtered by thermocoax at low temperature and ceramic π filters at room temperature. A photograph of our ^{3}He system is shown in Fig. A.5.
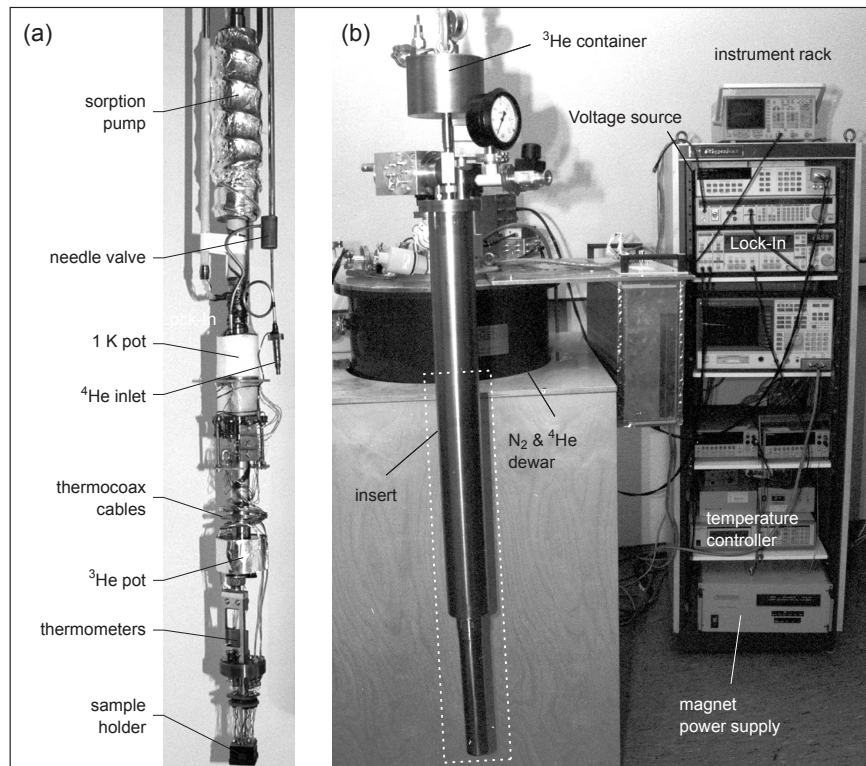
Figure A.5: (a) Insert of low temperature ^{3}He cryostat. Here, the tube of the isolation vacuum has been removed. (b) ^{3}He cryostat with measurement rack.

Appendix B

Superconducting contacts to SWNTs

Exploration of the superconductivity and the proximity effect in nanosize systems attracted enormous theoretical attention [12]. The injection of entangled Copper pairs via superconducting contacts attached to a QD is considered as an excellent candidate for the creation of non-local spin entangled pairs, which could be used as a building block for a quantum computer.

We have taken an endeavor to explore superconductivity in SWNTs. Except for the above mentioned reason, this step has been motivated by the controversial observation of intrinsic superconductivity in bundles of SWNTs [148] and proximity effect in individual SWNTs [51].

Recently, our group has reported the observation of resonant multiple Andreev reflections in a MWNT QD coupled to superconducting leads [149, 52]. The lithographically defined leads were evaporated over the MWNT, 45 nm of Au followed by 135 nm of Al. The gap energy Δ_{al} for Al is 0.18 meV, corresponding to $T_c = 1.17$ K. However, this value is usually reduced to $\Delta_{al} \approx 0.1$ meV due to an intermediate Au layer [150]. Below the T_c of Al/Au bilayer a sharp drop of the resistance is observed indicating Andreev reflection effect. Resonant multiple Andreev reflections (MAR) appear inside the superconducting gap (Δ) due to proximity effect. For the observation of MAR processes, good contacts between QD and superconducting leads are necessary since they are proportional to $\boldsymbol{T}^2$, where $\boldsymbol{T}$ is the transmission probability. Moreover, on-site Coulomb repulsion reduces Andreev processes even further. Favorable condition for the observation of MAR in a QD is that the life time broadening Γ of the levels in the QD should be comparable with Δ_{al}, and that the charging energy U_c is smaller than the superconducting gap $U_c < \Delta_{al}$. Although, we were aware of the fact that $U_c > \Delta_{al}$ in a SWNT, we have tried to make transport measurements on the SWNTs contacted with an Al/Au bilayer. As explained in

the chapter 2, we found that the devices contacted with Au behave at low temperature as QDs in CB regime. In some of our devices we have seen increase in the conductance below $T = 1\,\mathrm{K}$ as shown in Fig. B.1a. However, we have not found evidence of MAR effects probably because the transmission between contacts and SWNT was too low. The observed increase in conductance is most likely due solely to Al transition to superconducting state in the leads.

We have also tried to use different superconducting materials as leads, namely In and Nb. The reason for this is their higher superconducting transition temperature In ($T_c \approx 3.41\,\mathrm{K}$), Nb ($T_c \approx 9.25\,\mathrm{K}$), where CB effects are expected to be smaller (chapter 4.). The device made by evaporated In contacts on a SWNT is shown in Fig. B.1b. The granularity of In contacts, have been the main obstacle for achieving good contacts to CNTs. We have tried to solve this problem with a Ti adhesion layer followed by Al and In evaporation, nevertheless reliable contacts have not been achieved. From the other side, because of high melting temperature of Nb, it was very unreliable to realize metallic interconnections for structures patterned with EBL. Well developed methods for structuring Nb in the semiconductor research have been useless for our purposes considering that any reactive ion oxygen etching destroys CNTs. However, using optical lithography it is possible to make Ti contacts followed by a Nb layer. In this case, contacts have been found to be low transparent, suggesting that mainly Ti-CNT interface determine over all conductance of our devices as explained in chapter 2.
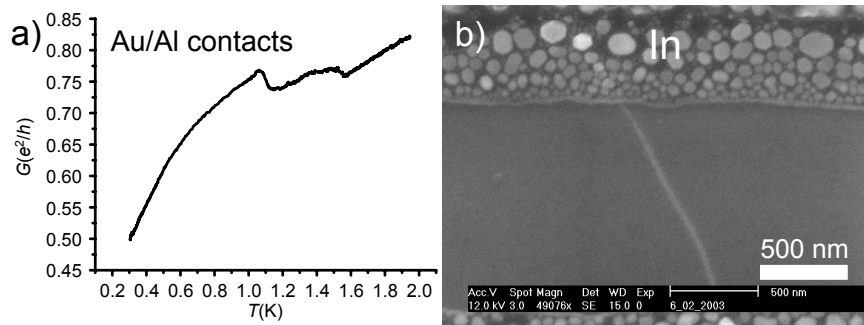
Figure B.1: (a) Dependance of the conductance versus temperature for a SWNT device contacted with Al/Au bilayer. Increase in the conductance around $T \approx 1\,\mathrm{K}$ is attributed to superconducting transition of the electrodes. (b) A SEM image of a CNT contacted with In. Granular In leads have been the main obstacle to implement reliable contacts in CNT devices.

Bibliography

[1] R. P. Feynman, there's Plenty of Room at the Bottom, APS meeting, 1959, http://www.zyvex.com/nanotech/feynman.html.

[2] R. Heath, P. J. Kuekes, G. S. Snider, and R. S. Williams, Science **280**, 1716 (1998).

[3] A. Aviram and M. Ratner, Chem. Phys. Lett. **29**, 277 (1974).

[4] G. Binnig, H. Rohrer, C. Gerber, and E. Weibel, Phys. Rev. Lett. **49**, 57 (1982).

[5] J. S. Foster, J. E. Frommer, and P. C. Arnett, Nature **331**, 322 (1988).

[6] H. F. Kroto *et al.*, Nature **318**, 162 (1985).

[7] S. Iijima and T. Ichihashi, Nature **354**, 56 (1991).

[8] C. Muller, J. van Ruitenbeek, and L. de Jongh, Physica C **318**, 162 (1992).

[9] D. K. Ferry and S. M. Goodnick, *Transposrt in Nanostructures* (Cambridge University Press, New York, 1997).

[10] S. Datta, *Electronic Transport in Mesoscopic Systems* (Cambridge University Press, New York, 1998).

[11] D. S. Saraga and D. Loss, Phys. Rev. Lett. **90**, 166803 (2003).

[12] P. Recher and D. Loss, Phys. Rev. B **65**, 165327 (2002).

[13] A. Thess *et al.*, Science **273**, 483 (1996).

[14] A. Krishnan *et al.*, Phys. Rev. B **58**, 14013 (1998).

[15] J. H. Hafner, C. L. Cheung, and M. Lieber, J. Am. Chem. Soc. **121**, 9750 (1999).

[16] C. Dekker, Physics Today **52(5)**, 22 (1999).

[17] S. J. Tans, R. M. Verschueren, and C. Dekker, Nature **393**, 49 (1998).

[18] J. Kong *et al.*, Nature **395**, 878 (1998).

[19] R. Krupke, F. Hennrich, H. v. Lohneysen, and M. M. Kappes, Science **301**, 344 (2003).

[20] S. J. Tans *et al.*, Nature **386**, 474 (1997).

[21] W. Liang *et al.*, Nature **411**, 665 (2001).

[22] M. Bockrath *et al.*, Nature **397**, 598 (1999).

[23] J. Nygård, D. Cobden, and P. E. Lindelof, Nature **408**, 342 (2000).

[24] Y. Saito *et al.*, Nature **389**, 554 (1997).

[25] J. Kong *et al.*, Science **287**, 622 (2000).

[26] S. S. Wong *et al.*, Nature **394**, 52 (1998).

[27] P. Kim and C. M. Lieber, Science **286**, 2148 (1999).

[28] J.Zhao, A.Buldum, J.Han, and J. Lu, Phys. Rev. Lett. **85**, 1706 (2000).

[29] S. J.Wind *et al.*, Appl. Phys. Lett. **80(20)**, 3817 (2002).

[30] C. Zhou, J. Kong, E. Yenilmez, and H. Dai, Science **290**, 1552 (2000).

[31] J. Kong, J. Cao, and H. Dai, Appl. Phys. Lett. **80**, 73 (2002).

[32] Z. Yao, H. W. C. Postma, L. Balents, and C. Dekker, Nature **402**, 273 (1999).

[33] N. W. Ashcroft and N. D. Mermin, *Solid State Physics* (Saunders College Publishing, New York, 1976).

[34] J.W.G.Wildoer *et al.*, Nature **391**, 59 (1998).

[35] M. S. Dresselhaus, G. Dresselhaus, and P. C. Eklund, *Science of Fullerenes and Carbon Nanotubes* (Academic Press, New York, 1996).

[36] P. L. McEuen *et al.*, Phys. Rev. Lett. **83**, 5098 (1999).

[37] C. Kittel, *Introduction to Solid State Physics* (John Wiley and Sons, New York, 1996).

[38] Z. Yao, C. L. Kane, and C. Dekker, Phys. Rev. Lett. **84**, 2941 (2000).

[39] J. Kong, A. M. Cassel, and H. Dai, Chem. Phys. Lett. **292**, 567 (1998).

[40] J. H. Hafner *et al.*, Chem. Phys. Lett. **296**, 195 (1998).

[41] Two different substrates are used: Si/SiO_2 or $Si/SiO_2/Si_3N_4$ heterostructure.

[42] Calibrated massflow controllers were used, except for the large flow rate of methane of $5000\,cm^3/min$, which was adjusted and meseared with a floating ball meter calibrated to air. The correction factor for methan is ≈ 1.4, i.e. the actual flow was 1.4 times larger.

[43] M. M. J. Treacy, T. W. Ebbesen, and J. M. Gibson, Nature **381**, 678 (1996).

[44] P. Poncharal, Z. L. Wang, D. Ugarte, and W. A. Heer, Science **283**, 1513 (1999).

[45] A. Javey *et al.*, Nature **424**, 654 (2003).

[46] Chromium is used because it could sustain high temperature of CVD process with no apparent diffusion.

[47] S. J. Tans, M. H. Devoret, R. J. A. Groeneveld, and C. Dekker, Nature **394**, 761 (1998).

[48] M. Bockrath *et al.*, Science **275**, 1922 (1997).

[49] P. G. Collins, M. S. Arnold, and P. Avouris, Science **292**, 706 (2001).

[50] M. Büttiker, *Quantum Mesoscopic Phenomena and Mesoscopic Devices in Microlectronics* (Kluwer, New York, 2000), pp. 211–242.

[51] A. Y. Kasumov *et al.*, Science **284**, 1508 (1999).

[52] M. R. Buitelaar *et al.*, Phys. Rev. Lett. **91**, 057005 (2003).

[53] A. Jensen, J. Nygård, and J.Borggreen, World Scientific 33 (2003).

[54] R. Martel *et al.*, Phys. Rev. Lett. **87**, 256805 (2001).

[55] M. Krüger *et al.*, Appl. Phys. Lett. **78**, 1291 (2001).

[56] R. J. Chen *et al.*, Appl. Phys. Lett. **79**, 2258 (2001).

[57] S. Heinze *et al.*, Phys. Rev. Lett. **411**, 89 (106801-1).

[58] R. Martel *et al.*, Phys. Rev. Lett. **87**, 256805 (2001).

[59] V. Derycke, R. Martel, J. Appenzeller, and P. Avouris, Appl. Phys. Lett. **80**, 2773 (2002).

[60] M. Bockrath *et al.*, Phys. Rev. B **61**, R10606 (2000).

[61] R. Martel, V. Derycke, J. Appenzeller, and P. Avouris, Nano. Lett. **1**, 453 (2001).

[62] J. Kong, C. Zhou, E. Yenilmez, and H. Dai, Appl. Phys. Lett. **77**, 3977 (2000).

[63] M. Bockrath *et al.*, Phys. Rev. B **61**, R10606 (2000).

[64] M. Radosavljevic, M. Freitag, K. V. Thadani, and A. T. Johnson, Nano Lett. **2 No.7**, 761 (2002).

[65] A. Javey, M. Shim, and H. Dai, Appl. Phys. Lett **80**, 1064 (2002).

[66] A. Bachtold *et al.*, Phys. Rev. Lett. **84**, 6082 (2000).

[67] B. Babić, M. Iqbal, and C. Schönenberger, Nanotechnology **14**, 327 (2003).

[68] J. Park and P. L. McEuen, Appl. Phys. Lett. **79**, 1363 (2001).

[69] M. Bockrath *et al.*, Nature **397**, 598 (1999).

[70] A. Bachtold *et al.*, Phys. Rev. Lett. **87**, 166801 (2001).

[71] M. Freitag, M. Radosavljevic, Y. Zhou, and A. T. Johnson, Appl. Phys. Lett. **79**, 3326 (2001).

[72] T. Nakanishi, A. Bachtold, and C. Dekker, Phys. Rev. B **66**, 073307 (2002).

[73] C. W. Beenaker, Phys. Rev. B **44**, 1646 (1991).

[74] J. W. G. Wildöer *et al.*, Nature **391**, 59 (1998).

[75] K. Liu, M. Burghard, S. Roth, and P. Barnier, Appl. Phys. Lett. **75**, 2494 (1999).

[76] F. Léonard and J. Tersoff, Phys. Rev. Lett. **83**, 5174 (1999).

[77] F. Léonard and J. Tersoff, Phys. Rev. Lett. **84**, 4693 (2000).

[78] H. Grabert and M. H. Devoret, *Single Charge Tunneling, Coulomb Blockade phenomena in Nanostructures* (Plenum Press, New York, 1992), Vol. NATO ASI Series B 294.

[79] L. Kouwenhoven *et al.*, *Electron transport in quantum dots* (Kluwer, New York, 1997), Vol. Proceedings of the NATO Advanced Study Institute on Mesoscopic Electron Transport (Series E345).

[80] W. G. van der Wiel *et al.*, Rev. Mod. Phys. **75**, 1 (2003).

[81] S. D. Franceschi *et al.*, Phys. Rev. Lett. **86**, 878 (2001).

[82] D. Goldhaber-Gordon *et al.*, Nature **391**, 156 (1998).

[83] L. Kouwenhoven and L. Glazman, Physics world **January 2001**, 33 (2001).

[84] W. D. Knight *et al.*, Phys. Rev. Lett. **52**, 2141 (1984).

[85] S. Tarucha *et al.*, Phys. Rev. Lett. **77**, 3613 (1996).

[86] M. R. Buitelaara *et al.*, Phys. Rev. Lett. **88**, 256801 (2002).

[87] W. Liang, M. Bockrath, and H. Park, Phys. Rev. Lett. **88**, 126801 (2002).

[88] U. Fano, Nuovo Cimento **12**, 156 (1935).

[89] J. Göres *et al.*, Phys. Rev. B. **62**, 2188 (2000).

[90] D. V. Averin, A. N. Korotkov, and K. K. Likharev, Phys. Rev. B **44**, 6199 (1991).

[91] This is an approximation for a cylindrical metallic object surrounded by a diaelectric.

[92] The relative dielectric constant of SiO_2 is 4.4.

[93] C. T. White and T. N. Todorov, Nature **393**, 240 (1998).

[94] J. Kondo, Solid State Physics **23**, 183 (1969).

[95] S. M. Cronenwet, T. H. Oosterkamp, and L.P.Kouwenhoven, Science **281**, 540 (1998).

[96] L. Glazman, J. Low. Temp. Phys. **118**, 247 (2000).

[97] D. Goldhaber-Gordon *et al.*, Phys. Rev. Lett. **81**, 5225 (1998).

[98] Y. Meir, N. S. Wingreen, and P. A. Lee, Phys. Rev. Lett. **70**, 2601 (1993).

[99] G. A. Fiete, G. Zarand, and B. I. Halperin, Phys. Rev. B **66**, 024431 (2002).

[100] Y. Oreg, K. Byczuk, and B. I. Halperin, Phys. Rev. Lett. **85**, 365 (2000).

[101] S. Sasaki *et al.*, Nature **405**, 764 (2000).

[102] A. Fuhrer *et al.*, Phys. Rev. Lett. **91**, 206802 (2003).

[103] M. Eto and Y. V. Nazarov, Phys. Rev. Lett. **85**, 1306 (2000).

[104] M. Pustilnik and L. Glazman, Phys. Rev. Lett. **85**, 2993 (2000).

[105] M. Pustilnik, L. Glazman, D. H. Cobden, and L. P. Kouwenhoven, Lecture Notes in Physics **3**, 579 (2001).

[106] M. Pustilnik, L. Borda, L. I. Glazman, and J. von Delft, cond-mat/0309646 (2003).

[107] D. H. Cobden *et al.*, Phys. Rev. Lett. **81**, 681 (1998).

[108] F. Simmel *et al.*, Phys. Rev. Lett. **83**, 804 (1999).

[109] M. Krawiec and K. I. Wysokiński, Phys. Rev. B **66**, 165408 (2002).

[110] T. A. Costi, A. C. Hewson, and V. Zlatic, J. Phys. Cond. Matter **6**, 2519 (1994).

[111] J. O. Connerade and A. M. Lane, Rep.Prog.Phys. **51**, 1439 (1988).

[112] U. Fano, Phys. Rev. **124**, 1866 (1961).

[113] R. K. Adair, C. K. Bokelman, and R. E. Peterson, Phys. Rev. **76**, 308 (1949).

[114] J. A. Simpson and U. Fano, Phys. Rev. Lett. **11**, 158 (1963).

[115] F. Cerdeira, T. A. Fjeldly, and M. Cordona, Phys. Rev. B **8**, 4734 (1973).

[116] V. Madhavan *et al.*, Science **280**, 567 (1998).

[117] J. Kim *et al.*, Phys. Rev. Lett. **90**, 166403 (2003).

[118] W. Yi *et al.*, Phys. Rev. Lett. **90**, 166403 (2003).

[119] D. A. D. Z. Zhang, V. Chandrasekhar and R. S. Ruoff, cond-mat/0311360v1 (2003).

[120] A. Clerk, X. Veintal, and P. W. Brouwer, Phys. Rev. Lett. **86**, 4636 (2001).

[121] K. Kobayashi, H. Aikawa, S. Katsumoto, and Y. Iye, Phys. Rev. B **68**, 235304 (2003).

[122] K. Kobayashi, H. Aikawa, S. Katsumoto, and Y. Iye, Phys. Rev. Lett. **88**, 256806 (2002).

[123] A. Yacoby, M. Heiblum, D. Mahalu, and H. Shtrilman, Phys. Rev. Lett. **74**, 4047 (1995).

[124] Y. Imry, *Introduction to mesoscopic physics* (Oxford University Press, New York, 1997).

[125] I. G. Zacharia *et al.*, Phys. Rev. B **64**, 155311 (2001).

[126] M. L. L. de Guevara, F. Claro, and P. A. Orelanna, Phys. Rev. B **67**, 195335 (2003).

[127] B. Kubala and J. König, Phys. Rev. B **65**, 245301 (2003).

[128] B. Kubala and J. König, Phys. Rev. B **67**, 205303 (2003).

[129] O. Lourie and H. D. Wagner, Journal of Materials Research **13(9)**, 2418 (1998).

[130] M. F. Yu *et al.*, Science **287**, 637 (2000).

[131] D. A. Walters *et al.*, Appl. Phys. Lett. **74**, 3803 (1999).

[132] X. Ming *et al.*, Nature **421**, 496 (2003).

[133] M. L. Roukes, Physics World **14**, 25 (2001).

[134] B. Reulet *et al.*, Phys. Rev. Lett. **85**, 2829 (2000).

[135] L. D.Landau and E. M. Lifschitz, *Theory of Elasticity* (Permagon Press, New York, 1959), Vol. NATO ASI Series B 294.

[136] S. Sapmaz, Y. M. Blanter, L. Gurevich, and H. S. J. van der Zant, Phys. Rev. B **67**, 235414 (2003).

[137] A. M. Cassell *et al.*, J. Am. Chem. Soc. **121**, 7975 (1999).

[138] N. R. Franklin, J. Han, and H. Dai, Adv. Mater. **12**, 890 (2000).

[139] G. Kim, G. Gu, U. Waizmann, and S. Roth, Appl. Phys. Lett. **80**, 1815 (2002).

[140] N. R. Franklin *et al.*, Appl. Phys. Lett. **81**, 913 (2002).

[141] see e.g. Chapter 2.

[142] J. Nygård and D. H. Cobden, Appl. Phys. Lett. **79**, 4216 (2001).

[143] Buffered hydrofluoric acid is made according to the following recepie: 28 ml HF + 107 ml H_20 + 113 g NH_4F. The etch rate for SiO_2 is 50 nm/min.

[144] T. Hoss, Ph.D. thesis, University of Basel, 2000.

[145] The etch ratio of Si to SiO_2 is ≈ 500, for 20 % weight mass of KOH at $60\,^0C$.

[146] J. P. Lu, Phys. Rev. Lett. **79**, 1297 (1997).

[147] J.-P. Salvetat *et al.*, Adv. Mater. **11**, 161 (1999).

[148] M. Kociak *et al.*, Phys. Rev. Lett. **86**, 2416 (2001).

[149] M. R. Buitelaar, T. Nussbaumer, and C. Schönenberger, Phys. Rev. Lett. **89**, 256801 (2003).

[150] E. Scheer *et al.*, Phys. Rev. Lett. **78**, 3535 (1997).

Publication list

Publications in journals and proceedings:

- *Suitability of carbon nanotubes grown by chemical vapor deposition for electrical devices*, B. Babić, J. Furer, M. Iqbal and C. Schönenberger, submitted to the Proc. of the 18th Int. Winterschool on Electronic Properties of Novel Material (2004).

- *Intrinsic thermal vibrations of suspended doubly clamped single-wall carbon nanotubes*, B. Babić, J. Furer, S. Sahoo, Sh. Farhangfar and C. Schönenberger, Nano Letters **3(11)**, 1577, (2003).

- *Multiple Andreev Reflection in a Carbon Nanotube Quantum Dot*, M. R. Buitelaar, W. Belzig, T. Nussbaumer, B. Babić, C. Bruder and C. Schönenberger, Phys. Rev. Lett. **91**, 057005, (2003).

- *Ambipolar field-effect transistor on as-grown single-wall carbon nanotubes*, B. Babić, M. Iqbal and C. Schönenberger, Nanotechnology **14**, 327, (2003).

- *Nanomechanics of Microtubules*, A. Kis, S. Kasas, B. Babić, A. J. Kulik, W. Benoit, G. A. D. Briggs, C. Schönenberger, S. Catsicas and L. Forró, Phys. Rev. Lett. **89**, 248101, (2002).

Invited talks:

- *Electronic properties of CVD-grown Single-wall Carbon Nanotubes*, Seminar talk at Josef Stefan Institute, Ljubljana (Slovenia), December 2003.

- *Mechanical properties of CVD-grown Single-wall Carbon Nanotubes*, Seminar talk at the group of J. P. Kotthaus, München (Germany), November 2003.

Curriculum Vitae

Bakir Babić

10. 6. 1976	Born in Sarajevo, Bosnia and Herzegovina.
1991-1995	I Gymnasium, Sarajevo.
1995-2000	Studied and graduated at Physics Department of University in Zagreb, under the supervision of Prof. dr. M. Požek and Prof. dr. A. Dulčić. Subject: 'Observation of depolarization transition by microwave absorption in Si semiconductor'.
2001-2004	Ph.D. research at Basel University in the group of Prof. dr. C. Schönenberger. Subject: 'Electrical Characterization of Carbon Nanotubes grown by Chemical Vapor Deposition Method'.
2004-	Postdoctoral research in the group of Prof. Imamoglu at ETH Zurich.

Acknowledgements

This thesis would be very different without the support of a several people.

First of all, I would like to thank my Ph.D. advisor Christian Schönenberger who has always been helpful, enthusiastic and supportive. I highly appreciate that you could always find a time for the stimulating discussions (although sometimes painful but always useful). I learned a lot from you. Particulary I am grateful for your guidance on tackling problems, writing publications and dealing with people.

I am especially grateful to Mark Buitelaar and Mahdi Iqbal for introducing me to the different experimental techniques and extensive discussions inside and outside the lab. I furthermore thank the following Ph.D. students: Erasmus Bieri, François Dewarrat, Jürg Furer, Lucia Grüter, Gunnar Gunnarsson, Soufiane Ifadir, Dino Keller and Sangeeta Sahoo; and postdocs: Michel Calame, Adam Hansen, Christian Hoffmann, Shadyar Farhangfar, Derek Kelly, Takis Kontos, Zuqin Liu, Thomas Nussbaumer and Stefan Oberholzer who made my time in Basel happy, sane and productive. I also thank Andras Kis and László Forró for successful collaboration on mechanics of microtubulus. Aside from the research, I would like to thank secretaries Barbara Kammerman and Astrid Kalt for the help on bureaucratic problems and friendly chats.

Last, but not least I thank my family and friends in Sarajevo and Zagreb for all these years of support, understanding and encouraging. Most of all, I am grateful to my wife Onelia for the overwhelming patience and love during our stay in Basel.

At the end, I acknowledge the financial support during my Ph.D from the BBW and the NCCR on Nanoscience.